

# Dam Break of Newtonian Fluids and Granular Suspensions: Internal Dynamics Measurements

THÈSE N° 5344 (2012)

PRÉSENTÉE LE 19 AVRIL 2012

À LA FACULTÉ DE L'ENVIRONNEMENT NATUREL, ARCHITECTURAL ET CONSTRUIT  
LABORATOIRE D'HYDRAULIQUE ENVIRONNEMENTALE  
PROGRAMME DOCTORAL EN MÉCANIQUE

ÉCOLE POLYTECHNIQUE FÉDÉRALE DE LAUSANNE

POUR L'OBTENTION DU GRADE DE DOCTEUR ÈS SCIENCES

PAR

Nicolas ANDREINI

acceptée sur proposition du jury:

Prof. L. Laloui, président du jury  
Prof. C. Ancey, directeur de thèse  
Dr G. Chambon, rapporteur  
Prof. F. Gallaire, rapporteur  
Dr G. Ovarlez, rapporteur



ÉCOLE POLYTECHNIQUE  
FÉDÉRALE DE LAUSANNE

Suisse  
2012



# Remerciements

Je tiens à remercier mon directeur de thèse, le Prof. Christophe Ancey, de m'avoir suivi et guidé pendant ce travail. Son dynamisme et sa force de travail ont été une réelle motivation au quotidien. Je le remercie aussi pour son humanité et son franc-parler si rare par les jours qui courent.

D'autre part, je tiens à exprimer ma gratitude aux membres du jury: Dr. Guillaume Ovarlez, Prof. François Gallaire ainsi qu'au Dr. Guillaume Chambon pour leurs critiques et leurs commentaires enrichissants ainsi que pour avoir fait de l'examen de thèse un moment intéressant. Je suis particulièrement reconnaissant au Prof. Gallaire qui a été très arrangeant quant à la date et l'heure de la soutenance. Un grand merci au Prof. Lyesse Laloui qui a accepté de bien vouloir présider le jury malgré son emploi du temps extrêmement chargé.

En outre, merci à (plus ou moins par ordre chronologique): Steve de m'avoir initié à la préparation de caramels mous par dizaines de kilos; Claude pour son dynamisme et sa jeunesse d'esprit; Sébastien pour m'avoir tout appris sur l'isoindice; Martin pour son originalité et pour m'avoir fait vivre un "vrai" déménagement; Damien pour les bières post-plongée; Koen pour avoir fait l'expérience improbable de mettre des seiches dans une seiche; Panpam pour son paragliding spirit; Jean-Marc qui a conçu et construit l'incroyable canal que l'on a utilisé pour les expériences; Michel pour son support technique; Bob pour son aide ainsi que pour m'avoir appris ce qu'est l'agrément dans une auto; Gaël à qui je dois au moins la moitié de ce travail; François pour les cours de météo; Joris pour les discussions philosophiques alcolisées; tous les nouveaux du LHE en particulier Belinda qui a su rendre plus ou moins compréhensible ce document en corrigeant les innombrables fêtes d'anglais; tous les autres que j'aurais pu oublier par mégarde.

*Lausanne, le 29 Mars 2012*

N. A.



# Abstract

The objective of this thesis was to increase our understanding of two-phase geophysical flows (e.g. debris flows) by providing velocity profiles in idealized laboratory avalanches.

To that end, we developed a new experimental platform made up of an inclined flume coupled to an imaging system to measure velocity in granular suspension. The inclined flume was 3.5 m long and 10 cm wide and could be inclined from 0 to 35°. A reservoir with the capacity for 10 l of fluid was located in the upper part of the flume and closed with a pneumatic controlled gate. Velocity profiles were obtained using Particle Image Velocimetry (PIV) and index-of-refraction matching of the solid and liquid phases. We used transparent PMMA beads with mean diameters of 200  $\mu\text{m}$  and the interstitial fluid was composed of a mixture of three fluids. The interstitial fluid was adapted in order to match the refraction index and the density of the solid phase. Using pulsed laser and a high speed camera we were able to measure velocity profiles at frequencies up to 1000 Hz with very good precision.

Two additional cameras tracked the front position along the flume with a frequency of 30 Hz and a spatial resolution of 1 mm.

Prior to acquiring data on the granular suspension, we tested our system on Newtonian fluids. Eight flow configurations were selected with different fluids (glycerol and triton X100), different slopes and different released masses. Velocity profiles were found to be parabolic far from the front as well as very close to the contact line. However, near the front, quantitative theoretical predictions given by lubrication theory diverged from experimental results. Velocities were significantly overestimated ( $\sim 400\%$ ) by the theory at low Reynolds numbers ( $Re < 2$ ) and slightly underestimated ( $\sim 10\%$ ) at high Reynolds numbers ( $Re > 8$ ). Very good agreement with theory far from the front indicated that the accuracy of the setup was good (reliable calibration procedure and image processing methods).

Experiments on granular suspensions revealed a variety of behaviors depending on the particle concentration, the slope and the mass released.

At solid fractions up to 45%, suspensions behaved as homogeneous viscous fluids. For the duration of the experiment, it was not possible to detect any inhomogeneity due to migration or sedimentation. In the range of shear rate tested and with the precision allowed by the setup no shear thickening or shear thinning was observed since velocity profiles remained perfectly Newtonian.

For slightly more concentrated suspensions (up to 55%), we found that the flow dynamics

## Abstract

---

at the bulk scale could still be described using a viscous theory. However, at the local scale, migration gave rise to concentration inhomogeneities producing a blunted velocity profile. The shape of the blunted profile was well described by the Mills and Snabre migration model coupled to a Krieger-Dougherty effective viscosity. However, magnitudes of the velocities were largely overestimated, most probably because we fitted the effective viscosity at higher shear rates.

Above 55%, small released masses with high solid fractions stopped after a finite time and separation between fluid and solid phases occurred. The solid frame stayed at rest while the fluid seeped through the granular media eroding the front. For larger released masses, we observed successions of different regimes: After an inertial regime and a pseudo-viscous regime, the flow slowed down, corresponding to a new regime in which the shearing was localized in a thin layer at bottom and there was no shearing of the front. At the same time, we observed that the free surface deformed and became wavy. Fractures developed on the top of the flow and, if they grew sufficiently, modified the local velocity field substantially. Finally, at longer time ( $\geq 4$  min) an intermittent motion (stick-slip) was observed with phases during which the suspension was flowing in a quasi-steady regime and phases during which the suspension was at a halt.

**Keywords:** Dam break, avalanche, suspension, fluid, granular, Laser, PIV, isoindex, PMMA, Newtonian, front, velocity, migration

# Résumé

L'objectif de ce travail est de mesurer en laboratoire la vitesse des particules au sein d'avalanches de suspensions concentrées. Cette démarche est destinée à accroître nos connaissances sur les écoulements géophysiques biphasiques de taille réelle telles que les laves torrentielles par exemple.

A cette fin, une nouvelle plateforme expérimentale a été développée, composée d'un canal inclinable et d'un système optique capable de mesurer les vitesses des particules au sein d'une suspension granulaire en mouvement. Le dispositif d'une longueur de 3.5 m et d'une largeur de 10 cm était inclinable de 0 à 35°. A son extrémité amont, un réservoir fermé par une porte pneumatique permettait de relâcher instantanément jusqu'à 10 litres de fluide dans le canal. Les mesures de vitesse à l'intérieur de la masse en mouvement ont été effectuées par PIV (vélocimétrie laser par images de particules). Les particules employées, des billes de PMMA de 200  $\mu\text{m}$  de rayon moyen, sont mélangées à un liquide interstitiel dont la densité et l'indice de réfraction sont identiques aux billes. L'utilisation d'un laser pulsé à haute cadence a permis l'acquisition de profils de vitesse jusqu'à une fréquence de 1000 Hz. Deux caméras supplémentaires placées au-dessus du canal permettaient en outre de suivre la position du front en fonction du temps avec une fréquence de 30 Hz et une précision de 1 mm.

Une première campagne de mesures a été menée sur des fluides newtoniens afin de vérifier la fiabilité et la précision de la plateforme de mesures. Huit configurations ont été testées avec différents fluides (glycérol et Triton X100), différentes pentes et différentes masses. Les profils de vitesse mesurés étaient dans tous les cas de forme parabolique, aussi bien loin du front que très proches de la ligne de contact. L'amplitude des vitesses prédites par la théorie de lubrification (épaisseur de liquide faible devant les autres dimensions de l'écoulement) était en bon accord avec les résultats expérimentaux dans le corps de l'écoulement. Au front, en revanche, comme attendu, des différences notables entre théorie et expérience ont été constatées. Pour les écoulements à bas reynolds ( $Re < 2$ ), la théorie surestimait passablement l'augmentation de vitesse proche du front (800%) tandis que pour les écoulements à haut Reynolds ( $Re > 8$ ) l'inverse a été constaté (10%). Le très bon accord loin du front entre les profils de vitesse obtenus expérimentalement et les profils théoriques ont permis de confirmer la bonne précision de la procédure expérimentale et du setup (méthode de calibration et de traitement d'images fiables).

Les expériences sur les suspensions granulaires ont révélé une grande variété de comporte-

ments selon la concentration en matière solide, la pente ou la masse relâchée.

Pour les suspensions contenant moins de 45% de fraction solide, le comportement observé était celui d'un fluide newtonien homogène. Durant la durée des expériences aucune inhomogénéité due à de la migration ou de la sédimentation n'a pu être détectée. D'autre part, dans la gamme de cisaillements testés, ni rhéofluidification ni rhéoépaississement n'ont été observés. Pour les suspensions légèrement plus concentrées (jusqu'à 55%), la position du front de l'écoulement, et donc la dynamique globale de celui-ci était correctement décrite à l'aide d'une théorie visqueuse. En revanche, à l'échelle locale, la migration des particules vers les couches les plus hautes de l'écoulement donnait lieu, loin du front, à des profils de vitesse creusés par rapport aux profils newtoniens. La forme de ces nouveaux profils de vitesse était correctement capturée par un modèle de migration de type Mills et Snabre couplé à une viscosité effective de type Krieger-Dougherty. En revanche, si la forme était bien décrite, la norme des vitesses était largement surestimée par la théorie. Cette différence était vraisemblablement due au fait que l'expression utilisée pour la viscosité effective a été calée pour des taux de cisaillements plus importants.

Au-dessus de 55%, pour les masses les plus faibles, l'écoulement s'arrêtait avant qu'une séparation liquide-solide ne naisse. Le fluide interstitiel suintait alors de la matrice solide et érodait peu à peu le front. Pour des masses plus importantes, une succession de différents régimes fut observé. Après un régime inertiel et un régime pseudo-visqueux, un ralentissement de l'écoulement prenait place. Dans ce nouveau régime, le cisaillement était localisé aux couches les plus proches du fond et le front n'était pas cisailé. Parallèlement, des fractures à la surface de l'écoulement se développaient, modifiant le champ de vitesse localement. Finalement, à des temps plus longs (typiquement 4 minutes après l'ouverture de la porte), un mouvement intermittent (stick-slip) se mettait en place, constitué de phases où la suspension était à l'arrêt et de phases où la suspension était en écoulement/glisement avec une vitesse constante.

**Mots-clés :** Rupture de barrage, avalanche, suspension, fluide, granulaire, Laser, PIV, isoindice, PMMA, Newtonien, front, vitesse, migration



# Contents

<b>Remerciements</b>	<b>iii</b>
<b>Abstract</b>	<b>v</b>
<b>List of figures</b>	<b>x</b>
<b>List of tables</b>	<b>xii</b>
<b>1 Introduction</b>	<b>1</b>
1.1 Structure and dynamics of debris flows . . . . .	2
1.2 Research scales and approach adopted in the present work . . . . .	4
1.3 Thesis layout and contributions . . . . .	6
<b>2 Theory</b>	<b>9</b>
2.1 Dam-break problem . . . . .	9
2.1.1 Newtonian flows . . . . .	12
2.2 Suspensions rheology and migration models . . . . .	13
2.2.1 Effective viscosity . . . . .	13
2.2.2 Migration . . . . .	15
2.3 Summary . . . . .	17
<b>3 Material and methods</b>	<b>19</b>
3.1 Particle Image Velocimetry (PIV) in concentrated suspensions . . . . .	20
3.2 Transparent suspensions . . . . .	21
3.2.1 Suspensions preparation and handling . . . . .	22
3.3 Experimental setup . . . . .	24
3.3.1 Flume . . . . .	24
3.3.2 Instrumentation . . . . .	25
3.3.3 Calibration and image processing . . . . .	27
3.4 Summary . . . . .	27
<b>4 Dam break of Newtonian fluids</b>	<b>29</b>
4.1 Fluids and procedures . . . . .	29
4.2 Results . . . . .	30
4.2.1 Front positions . . . . .	31

## Contents

---

4.2.2	Velocity profiles . . . . .	34
4.3	Summary . . . . .	37
<b>5</b>	<b>Dam break of granular suspensions</b>	<b>39</b>
5.1	Facility and procedures . . . . .	40
5.2	Results . . . . .	40
5.2.1	Runs with low solid fractions ( $\phi \leq 0.45$ ) . . . . .	42
5.2.2	Runs with intermediate solid fractions ( $0.45 < \phi \leq 0.55$ ) . . . . .	46
5.2.3	Runs with high solid fractions ( $\phi > 0.55$ ) . . . . .	55
5.3	Summary . . . . .	73
<b>6</b>	<b>Overall conclusions and outlook</b>	<b>75</b>
<b>A</b>	<b>Free-surface and pore pressure measurements</b>	<b>77</b>
A.1	Free-surface measurements . . . . .	77
A.2	Basal pore pressure measurements . . . . .	78
	<b>Bibliography</b>	<b>88</b>
	<b>Curriculum Vitae</b>	<b>89</b>

# List of Figures

1.1	Picture of a debris flow deposit (Fully, Valais, Switzerland) . . . . .	2
1.2	Idealized representation of a debris flow . . . . .	3
1.3	Sketch showing the path of a segregating coarse particle . . . . .	4
1.4	Different research scales. . . . .	5
2.1	Schematic defining the flow configuration . . . . .	10
3.1	Overview of the isoindex measurement technique . . . . .	20
3.2	Picture of a drop of suspension . . . . .	21
3.3	Grain size distributions of PMMA particles . . . . .	22
3.4	Sketch of the setup used during the outgassing process . . . . .	23
3.5	Sketch of the inclined flume . . . . .	24
3.6	Picture of the flow and sketch of the system used to measure the velocity . . . . .	26
3.7	Typical image recorded by the camera in a suspension flow . . . . .	26
4.1	Typical image recorded by the camera in a Newtonian flow . . . . .	30
4.2	Front position as a function of time for Newtonian flows . . . . .	32
4.3	Values of the $n$ exponent along the flume for Newtonian flows . . . . .	32
4.4	Differences between experiments and theory for $n$ and $x_f$ . . . . .	33
4.5	Flow depth variations . . . . .	34
4.6	Velocity profiles near the front of the flow for run (b) . . . . .	35
4.7	Dimensionless velocity profiles for run (e) . . . . .	35
4.8	Ratio of theoretical velocity to experimental velocity . . . . .	36
4.9	Theoretical velocity over experimental velocity in the tail/front . . . . .	36
5.1	Front positions and $n$ values for flows with a solid fraction $\leq 0.45$ . . . . .	42
5.2	Flow depth variations $h(t)$ for flows with a solid fraction $\leq 0.45$ . . . . .	43
5.3	Dimensionless velocity profiles for run (c) $\phi = 0.45$ . . . . .	44
5.4	Effective viscosity models fitted on experimental data of run (b) and (c) . . . . .	45
5.5	Front positions of flows with a solid fraction between 0.52 and 0.55 . . . . .	47
5.6	$n$ values for flows with a solid fraction between 0.52 and 0.55 . . . . .	47
5.7	Flow depth variations $h(t)$ for flows with a solid fraction $0.45 < \phi \leq 0.55$ . . . . .	48
5.8	Velocity profiles for run (f) ( $\phi = 0.52, \theta = 25$ deg, $m = 3$ kg) . . . . .	49
5.9	Velocity profiles for run (d) ( $\phi = 0.52, \theta = 5$ deg, $m = 3$ kg). . . . .	50

## List of Figures

---

5.10	Velocity profiles for run (g) ( $\phi = 0.55, \theta = 25$ deg, $m = 3$ kg).	51
5.11	Deviation from a parabolic velocity profile: time evolution	51
5.12	Comparison between migration models and steady state velocity profiles	52
5.13	Ratio between theoretical velocity and experimental velocity plotted in function of $u(h)/h$	53
5.14	Estimation of the self-diffusion coefficient $d(\phi)$	55
5.15	Front positions for flows with solid fractions between 0.56 and 0.595	57
5.16	$n$ values for flows with solid fractions between 0.56 and 0.595	57
5.17	Velocity profiles for run (h) ( $\phi = 0.56, \theta = 25$ deg, $m = 3$ kg).	58
5.18	Comparison between migration models and steady state velocity profiles ( $\phi = 0.56, 0.57$ )	59
5.19	Velocity profiles for run (i) ( $\phi = 0.57, \theta = 25$ deg, $m = 3$ kg)	60
5.20	Detail of the front positions for run (p) ( $\phi = 0.595, \theta = 25$ deg, $m = 6$ kg)	61
5.21	Comparison between sieved and non-sieved suspension flows	61
5.22	Longitudinal flow depth profiles $h(x)$ for Run (u) ( $\phi = 0.595, \theta = 25$ deg, $m = 7.9$ kg)	62
5.23	Velocity map during a free-surface fracture	64
5.24	Cross-stream flow depth profiles $h(y)$ for Run (u)	65
5.25	Picture of a free-surface fracture	66
5.26	Run (u): stick-slip initiation and death	66
5.27	Picture of the free surface after 60 min ( $\phi = 0.595, \theta = 25$ deg, $m = 6$ kg)	68
5.28	Pore pressure, velocities and flow depth during stick-slip	68
5.29	Detail of Figure 5.28 and corresponding velocity profiles	69
5.30	Time evolution of the free-surface velocity taken at different places along the flume.	70
5.31	Pore pressure evolution at four different places	70
5.32	Orbit in the velocity-pressure phase plane	71
A.1	Free-surface height measurements.	77
A.2	Pore pressure monitoring.	78



## List of Tables

4.1	Features of the runs with Newtonian fluids . . . . .	31
5.1	Features of the runs with suspensions . . . . .	41



# 1 Introduction

Debris flows are highly concentrated mixtures of sediments and water flowing down slopes under gravity. Large debris flow can exceed  $10^9 \text{ m}^3$  in volume [1] and can move at velocities as high as  $20 \text{ m s}^{-1}$  [2] with bulk densities around  $2000 \text{ kg m}^{-3}$ . The distance traveled by the surge can be very long compared to other geophysical mass movements like dry rock avalanches or landslides. The ratio between the runout distance  $L$  and the released height  $H$  can be as high as 25 for the largest debris flow which is double the observed traveling distance for dry avalanches of comparable volume [1]. This high mobility is due to solid-liquid interactions and gives debris flows a unique destructive power.

The deadliest debris flow occurred in 1985 in the Colombian Andes: On November 13, the Nevado del Ruiz volcano erupted producing pyroclastic flows. The  $10 \text{ km}^2$  of snow and ice previously accumulated on the summit were heated by the hot erupted material producing huge volumes of meltwater that flowed down. Aided by seismic shaking, the  $2 \cdot 10^7 \text{ m}^3$  of water entrained the new volcanic deposits and existing sediments. The initial dilute flows then became a debris flow made up of saturated snow, ice and rock. Velocity of the surge was as high as  $17 \text{ m s}^{-1}$  on the steepest slopes and discharge rates reached  $48000 \text{ m}^3 \text{ s}^{-1}$ . About  $9 \cdot 10^7 \text{ m}^3$  of material was transported to depositional areas situated up to 104 km from the source area [3]. Less than 12 h after the first eruption, the town of Armero located 40 km downstream was completely destroyed by the debris flow, killing more than 23000 of the 31000 citizens.

Besides this exceptional event, each year around the world in mountain areas, debris flows claim hundred of lives and cause millions of dollars of damage to property and infrastructures. For instance, in Japan, on average 90 lives are lost due to debris flows every year [4]. Europe is not spared from such phenomenomes. On May 5-6 1998, about 150 debris flows were triggered by exceptional rainfalls in Campania (Southern Italy) killing 161 people and leaving more than 1000 others homeless [5]. On 1 October 2009 in the Messina province of Sicily, debris flow due to high-intensity rainstorm caused 31 fatalities, damaged buildings and transportation infrastructures [6]. In Switzerland, there have been many reported events. Rickenmann [7] listed approximately 600 debris flows during the exceptional summer of 1987. On 13 August



Figure 1.1: Deposit after the debris flow that took place on 14 October 2000 in Fully, Valais, Switzerland.

1995, intense precipitation induced a 50'000 m<sup>3</sup> debris flow obstructing the highway near Villeneuve (Vaud, Switzerland), 23 million Euros were spent in order to clean and prevent further similar events in the same area [8]. More recently, on 14 October 2000, in Gondo (Valais, Switzerland), incessant rain for 48 hours triggered a 10'000 m<sup>3</sup> debris flow. More than 10 buildings were destroyed, killing 14 people [9]. On the same day, again in Valais a debris flow triggered by intense rain and a pipe leakage stopped at the limits of the village of Fully. Fortunately, only vineyards were destroyed (Figure 1.1).

Despite the catastrophic character of debris flows and relatively high occurrence of such natural hazards, considerable gaps remain in the basic understanding of the flow dynamics. This lack of knowledge most probably originates from the high complexity of the phenomenon. Although the flows usually take the appearance of viscous fluids, the impediments to a full fluid-mechanics approach are numerous: particle size can range from clay size (<2 μm) to boulder size, the composition and/or volume of the bulk usually changes during the flow [10, 11]. For instance, during the Nevado del Ruiz event, the initial volume of debris flow increased by a factor four [3]. In addition, most of the time the flow is strongly inhomogeneous and initial/boundary conditions are unknown.

### 1.1 Structure and dynamics of debris flows

The purpose of this section is to give a short description of a typical debris flow in order to have an idea of the complexity of the real-world full-scale phenomena before giving details on the simplifications made in our experiments.

Most of the time, debris flows can be separated in four distinct regions (Figure 1.2):



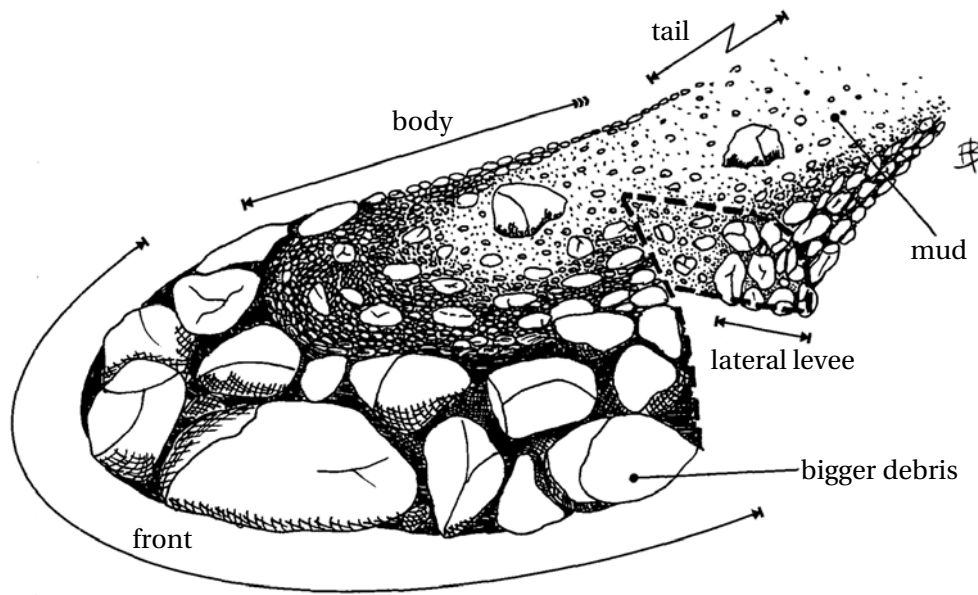


Figure 1.2: Idealized representation of a debris flow. Figure reproduced from Bardou [12].

- At the leading edge, *the frontal region* is composed mainly of big rocks. This region usually appears dry with frictional contact since the fluid seeps through the boulders. The largest rocks seem to be pushed and rolled by the rest of the debris flow.
- Behind the front, *the body* of the flow looks more like a viscous flowing liquid made up of blocks of any size. The biggest blocks seem to float at the free surface of the mixture. The apparent fluidity of the material is due to excess pore pressure that develops at the bottom of the flow [1]. The morphological characteristics of the flow depend mainly on debris properties (size distribution, concentration, mineralogy) and channel geometry (slope, shape...) [2]. However, most of the time the flow is laminar and turbulence is small. Due to the wide variety of grain sizes and shapes, the volume fraction of solid material in the flow can be as high as 0.8, a value much greater than the maximum random packing fraction of identical spheres ( $\sim 0.63$ ).
- On each side of the body, coarse material deposits are formed. These *lateral levees* are composed of almost the same material as the front.
- Behind the body, *the tail* is made up of a less concentrated material and looks like a muddy water flow.

This heterogeneous flow architecture is mainly dictated by segregation that occurs when the flow is sheared along the slope [13, 14]. As a mixture of large and small particles flow downslope, large grains rise to the surface while small grains percolate down to the lower layers of the flow [15, 16]. Thus, once coarse particles reach the surface they are transported to the front where they are submerged. Then, as coarse particles located at the base of the flow are

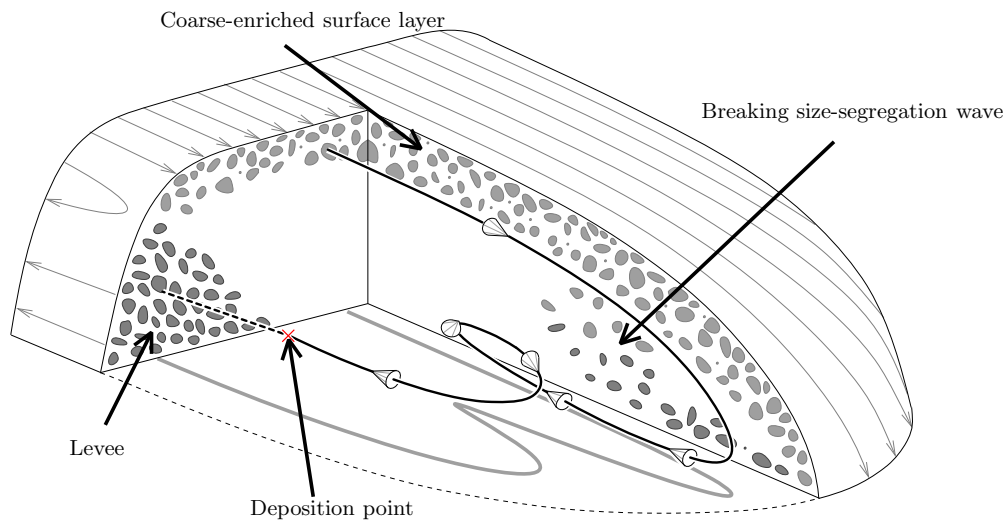


Figure 1.3: Sketch showing the three-dimensional path of a segregating coarse particle through the debris-flow head. Figure reproduced from Johnson [13].

moving more slowly, they are lifted upwards again due to segregation. This recirculation may occur several times but coarse particles are continually pushed away from the flow centerline toward the sides until they become part of the lateral levee (Figure 1.3).

In the lower layers of the body, the material is strongly sheared producing high pore pressure that diffuses through the flow depth [17, 18]. This excess pore pressure liquefies the body (contact between particles is not frictional anymore but becomes viscous) allowing the bulk to move faster and farther. Granular agitation also creates dilatation, and migration changes the local bulk density. When the flow reaches more gentle slopes, dry friction at the flow perimeter (lateral levees and front) becomes predominant and the flow stops. Excess pore-fluid pressure in the bulk interior then dissipates slowly [19, 20].

Pore pressure generation, multiple types of interaction between particles (frictional, collisional or viscous), spatial dependence of particle concentration and size distribution, and three-dimensional behavior of the surge all contribute to make debris flow dynamics a complex problem .

## 1.2 Research scales and approach adopted in the present work

To give insight into debris flow dynamics, field observations and laboratory experiments as well as theoretical research have been conducted since the beginning of the last century. Research occurs roughly at 3 different scales (Figure 1.4), each one having their own benefits and drawbacks:

- *In situ observations* have the main advantage of studying the phenomenon itself and thus prevent any additional interrogations about scale effects. However, measurements

## 1.2. Research scales and approach adopted in the present work



Figure 1.4: Different research scales. Left: In situ observation in the Illgraben: Instrumentation of the bed with a force plate and pore pressure sensors [21]. Center: Large-scale experiments into the USGS Debris-flow flume [17]. Right: Laboratory idealized experiments: dam-break of Carbopol gel on an inclined plane, measurement of the free surface topography [22].

on full scale debris-flows are not free of problems. First, most of the time it is not possible to predict where a debris flow will occur, making a preliminary instrumentation of the field impossible. This unpredictability means that, most of the time, investigation is only possible via postdepositional measurements on desiccated sediment samples reconstituted by adding water, which provide only a crudely estimation of debris flow density [1]. Even when debris flows are more or less predictable (like in the Illgraben debris flow torrent situated in the Swiss Alps [23]), few techniques exist to measure properties of the flowing materials. Invasive methods dramatically affect the flow and the noisy and dirty character of debris flows proscribes the use of non-invasive, more sophisticated techniques such as X ray, laser sheet or magnetic resonance imaging. Furthermore, initial and boundary conditions are not usually known. In short, to infer debris flow physics from in situ observations is very difficult since it is not possible to experimentally control any of the parameters, and measurements into the bulk conspicuously disturb the flow.

- *Large-scale experiments* consist of a large volume of natural sediment (sand/gravel) released in a well defined geometry. There are many advantages of such experiments over in situ measurements: the size distribution and water content of the flowing material can be controlled, the released mass, initial and boundary conditions are well known and instrumentation can be set up properly. Furthermore, experiments can be repeated as many times as needed. To that purpose, the U.S. Geological Survey (USGS) constructed an inclined flume 95 meters long, 2 meters wide, from which up to 20 cubic meters of wet sediment can be released [17]. However, there are still limitations

associated with the use of dirty sediments, when measuring flow properties inside the moving material with available techniques. Furthermore, the number of experiments and thus the number of parameters that can be varied is limited by the size of the experiment and the amount of work needed.

- *Laboratory idealized experiments* use synthetic material in a well controlled environment. The multiplicity of relevant dimensionless parameters make it impossible to scale a debris flow down to the size of a laboratory setup. However, controlling the material and boundary conditions make it possible to isolate physical phenomena that occur in the full scale debris flow. To that end, many experiments have been conducted on inclined planes or flumes using idealized material such as dry beads [24, 25, 26, 27, 28], granular suspension [29, 30, 31] or viscoplastic gels [32, 33, 34]. The main problems with such an approach may arise from scaling effects and/or oversimplifications.

In the present work we used an idealized approach. Laboratory experiments were conducted with model suspensions in a small inclined channel. The main simplifications regarding the real-world full-scale flows were:

- A simplified geometry: experiments were conducted in a flume in order to limit the three-dimensional character of the flow. In the body region the cross-stream velocity component was almost zero, however, near the tip region the fluid had to move to the sides and 3D-effects became significant.
- The slope of the bottom was held constant along the channel and the bottom was dry. Therefore, the total volume of the flow was not free to change and the mean composition of the bulk was fixed.
- The fluid was instantaneously released and was homogeneous before it began to flow.
- Particles were almost monodisperse regarding the broad debris flow size distribution and the shape was spherical.
- Interstitial fluid was Newtonian.
- Particles were neutrally buoyant. This was probably the most simplifying hypothesis since it excluded gravity-driven segregation and sedimentation processes.

### 1.3 Thesis layout and contributions

There are three major contributions in this work:

1. It shows that velocity profiles can be measured accurately in free-surface flows of dense suspension using isoindex techniques. Although some previous results were obtained in thin films [35], pipes [36] or Couette device [37], as far as we know, this technique was

not tested on big volumes of suspension released in open geometry. Since the refraction index of the fluid must be precisely controlled, it was not obvious that measurement on volumes as large as 10 liters would be possible.

2. It provides velocity profiles in a dam-break flow of Newtonian fluids. Compared to existing results, data were collected far from the wall and very close to the contact line.
3. The same measurements were performed on granular suspensions with solid fractions ranging from 15 to 59.5%. Two size distributions, various slopes and different released masses were tested. To our knowledge, no equivalent data set was available before.

Velocity profiles were also obtained for dam break flow of Carbopol gel (a viscoplastic fluid), results are shown in [38].

Including this introduction, this document has 6 chapters. Chapter 2 gives a short introduction to theoretical aspects related to the dam-break problems and mathematical asymptotic solutions for newtonian fluids. A brief overview of the suspension rheology with an emphasis to migration is also given in the second part of the chapter. In Chapter 3 the facility and measurement techniques are described. Despite the complexity of the technique we kept the description relatively short in order to emphasize experimental results rather than technical details. More information on velocity measurements in transparent suspensions can be found in [39, 40]. In Chapter 4 we report results obtained with newtonian fluids. Dam-break experiments at different slopes and with different released volumes were conducted to test the reliability of our system and provide new data near the front of the flow. In Chapter 5 we report results obtained with granular suspensions. We divided the chapter in three sections corresponding to increasing concentrations of particles. Velocity profiles and front positions are shown and compared with viscous theory and migration models. We also extensively describe an intermittent regime (stick-slip) that take place at long times for highly concentrated suspensions. Finally, Chapter 6 summarizes the results.



## 2 Theory

We address the problem of a finite volume of concentrated suspension, initially released from a reservoir, which flows down an inclined flume. The flow of suspensions has been extensively studied in a broad variety of geometries since they are involved in many industrial processes, natural phenomena, biological systems and home products. However, most of the time observations and calculations are done in a simple fixed geometry near the steady state and with rather low solid fraction (i.e. 30-50%). In a dam-break experiment, the flow is highly transient, has moving boundaries and a strong free surface curvature near the front, making the problem more complicated to solve. Even for a simple Newtonian fluid, the dam-break problem from a mathematical standpoint is far from being completely understood.

The objective of this chapter is to examine the physical phenomena and the related equations that may play a role in a dam-break flow of idealized suspension. We assume that the suspension is made up of spherical, monodisperse, neutrally buoyant particles in a Newtonian interstitial fluid. The present chapter is divided into two parts: The first part is dedicated to the dam-break flow regimes and the analytical solutions when the fluid is Newtonian. A second part summarizes the rheological properties of concentrated suspensions with an emphasis on migration in a free surface flow.

### 2.1 Dam-break problem

The dam-break experiment is the prototypical flow configuration used for investigating gravity-driven flows. A given volume of fluid is placed in a reservoir at the top of an inclined plane. Then, at time  $t = 0$ , the fluid is suddenly released by the instantaneous opening of the gate and flows down the inclined plane.

Here, we examine this problem from a theoretical standpoint. We assume that the plane is infinite in the cross-stream direction leading to a two-dimensional flow regime. As shown on Figure 2.1, we define a two-dimensional Cartesian coordinate system in which the  $x$ -axis points down the flume and the  $y$ -axis is in the direction of the upward pointing normal. The rear end of the reservoir is chosen to be the origin of the  $x$ -axis. The plane is inclined at an angle  $\theta$ , and the velocity  $\mathbf{u}$  has components  $u$  and  $v$  in the  $x$  and  $y$  directions respectively. The

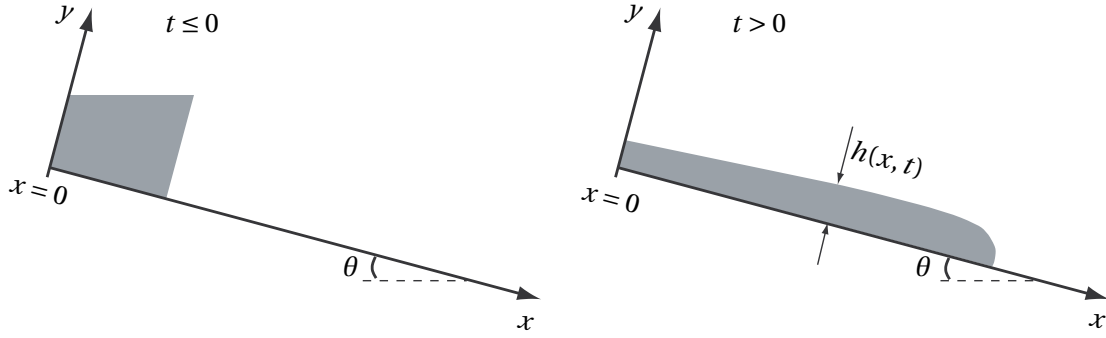


Figure 2.1: Schematic defining the flow configuration.

flow depth is denoted by  $h(x, t)$  and the pressure by  $p(x, y, t)$ . We assume that the flowing material which consists of solid particles and fluid can be treated as a continuum and that the density of the particles is the same as the density of the fluid ( $\rho$  constant everywhere).

The governing equations are given by the mass balance,

$$\nabla \cdot \mathbf{u} = 0, \quad (2.1)$$

and the momentum balance equations:

$$\rho \frac{\partial \mathbf{u}}{\partial t} + \rho (\mathbf{u} \cdot \nabla) \mathbf{u} = \rho \mathbf{g} - \nabla p + \nabla \cdot \sigma, \quad (2.2)$$

with  $\mathbf{g}$  as the gravitational acceleration and  $\sigma$  the deviatoric stress tensor. We neglect the surface tension and assume that the ambient fluid has a low density compared to the moving fluid, which implies that the stress state at the free surface is negligible. We also assume that no slip occurs at the bottom of the flow.

$$v(x, h, t) = \frac{\partial h}{\partial t} + u(x, h, t) \frac{\partial h}{\partial x}, \quad u(x, 0, t) = v(x, 0, t) = 0. \quad (2.3)$$

Without fixing any particular rheology, but assuming that the bulk viscosity does not vary significantly with shear rate over a sufficiently wide range, we define the bulk viscosity,  $\eta = \tau / \dot{\gamma}$ . Equations (2.2) and (2.3) can be transformed into dimensionless expressions as follows [41]: Let  $U_*$ ,  $V_*$ ,  $T_*$ ,  $P_*$  and  $\eta_*$  represent respectively, the characteristic streamwise and vertical velocities, the timescale, the typical pressure and the order of magnitude of the bulk viscosity. The typical vertical and horizontal length scales are denoted by  $H_*$  and  $L_*$  and the aspect ratio is denoted by  $\epsilon = H_* / L_*$ . We also introduce the Reynolds number and Froude number

$$Re = \frac{\rho U_* H_*}{\eta_*}, \quad Fr = \frac{U_*}{\sqrt{g H_* \cos \theta}}. \quad (2.4)$$



and the following dimensionless variables:

$$\hat{u} = \frac{u}{U_*}, \quad \hat{v} = \frac{v}{V_*}, \quad \hat{x} = \frac{x}{L_*}, \quad \hat{y} = \frac{y}{H_*} \quad \text{and} \quad \hat{t} = \frac{t}{T_*}. \quad (2.5)$$

The stresses are scaled as follows

$$\hat{\sigma}_{xx} = \frac{\eta_* U_*}{L_*} \sigma_{xx}, \quad \hat{\sigma}_{xy} = \frac{\eta_* U_*}{H_*} \sigma_{xy}, \quad \hat{\sigma}_{yy} = \frac{\eta_* U_*}{L_*} \sigma_{yy} \quad \text{and} \quad \hat{p} = \frac{p}{P_*}, \quad (2.6)$$

with  $T_* = L_*/U_*$  and  $P_* = \rho g H_* \cos\theta$ , since it is expected that, to leading order, the pressure is hydrostatic. Setting  $V_* = \epsilon U_*$ , the mass balance equation reads

$$\frac{\partial \hat{u}}{\partial \hat{x}} + \frac{\partial \hat{v}}{\partial \hat{y}} = 0. \quad (2.7)$$

Substituting the dimensionless variables into (2.2) gives

$$\epsilon Re \frac{d\hat{u}}{d\hat{t}} = \frac{\epsilon Re}{Fr^2} \left( \frac{1}{\epsilon} \tan\theta - \frac{\partial \hat{p}}{\partial \hat{x}} \right) + \epsilon^2 \frac{\partial \hat{\sigma}_{xx}}{\partial \hat{x}} + \frac{\partial \hat{\sigma}_{xy}}{\partial \hat{y}}, \quad (2.8)$$

$$\epsilon^3 Re \frac{d\hat{v}}{d\hat{t}} = \frac{\epsilon Re}{Fr^2} \left( -1 - \frac{\partial \hat{p}}{\partial \hat{y}} \right) + \epsilon^2 \frac{\partial \hat{\sigma}_{xy}}{\partial \hat{x}} + \epsilon^2 \frac{\partial \hat{\sigma}_{yy}}{\partial \hat{y}}. \quad (2.9)$$

On the right-hand side of (2.8), the first term ( $\sim \tan\theta$ ) represents the gravitational forces, the second term is the pressure gradient ( $\sim \partial_{\hat{x}} \hat{p}$ ) and the third and fourth contributions account for viscous dissipation and depend on the rheology of the material. The terms in the left-hand side of (2.8) arise due to inertia.

Different regimes may occur, where two contributions prevail compared to the others. The most relevant regimes for dam break flows are:

- The inertial regime, where inertial and pressure gradient terms are of the same magnitude. This regime occurs when  $\epsilon Re \gg 1$  and  $Fr = O(1)$ . In this case, rheological effects are so low that they can be neglected and the final governing equations are the Euler equations. In a dam break experiment, this regime takes place at the early times after the opening of the gate. We have  $U_* = \sqrt{gH_* \cos\theta}$ .
- The diffusive regime, where the pressure gradient is balanced by the viscous stresses within the bulk. Inertial terms must be small compared to the pressure gradient and the slope must be shallow ( $\tan\theta \ll \epsilon$ ). This imposes  $\epsilon Re \ll 1$  and  $Fr^2 = O(\epsilon Re) \ll 1$  and we have  $U_* = \rho g \cos\theta H_*^3 / (\eta_* L_*)$ . For a Newtonian fluid on a horizontal bottom the diffusive regime is the asymptotic regime observed at long times [42].

- The quasi steady uniform regime, where the viscous contribution matches the gravitational acceleration. Inertia is negligible,  $\epsilon \ll 1$ ,  $Re = O(Fr^2)$  and  $\tan\theta \gg \epsilon$ , and we have  $U_* = \rho g \sin\theta H_*^2 / \eta_*$ . For a dam break involving a Newtonian fluid on a steep slope, this regime is the asymptotic regime observed at long times [43].

When no dominant balance takes place between the different forces, full governing equations must be solved. Even numerically the task is not easy and a depth averaged variation of the governing equations is often used to simplify the problem. Several approximated solutions for viscoplastic material with  $\tau = \tau_c + K\dot{\gamma}^\lambda$  have been derived. However, this chapter will focus on the more simple case of Newtonian fluids ( $\tau_c = 0$ ,  $\lambda = 1$ ) since, as a first approximation, idealized suspensions at moderate solid fractions are known to behave like viscous fluids.

### 2.1.1 Newtonian flows

In the following treatment, we assume that the characteristic length of the flow is much greater than the typical flow depth ( $\epsilon \ll 1$ ). This assumption, called lubrication theory, makes it possible to simplify equations (2.8) and (2.9) a great deal. For the sake of simplicity we skip many of the mathematical details to focus on the physical meaning of the solution (from a mathematical standpoint, much more attention must be paid to justifying the asymptotic expansions that underpin the results presented here-after [44]). Assuming that the fluid moves slowly, we can neglect the inertial terms in the governing equations. Combined with the shallow flow approximation, this assumption leads to an hydrostatic distribution of the fluid pressure

$$p = \rho g \cos\theta (h - y), \quad (2.10)$$

while the streamwise velocity component is given by the momentum balance equation

$$\frac{\partial \sigma_{xy}}{\partial y} + \rho g \sin\theta = \rho g \cos\theta \frac{\partial h}{\partial x}. \quad (2.11)$$

Integrating (2.11) shows that the velocity profile takes a parabolic shape, whose amplitude is modulated by the free surface curvature

$$u(x, y, t) = \frac{1}{2} K y (2h - y) \left( 1 - \cot\theta \frac{\partial h}{\partial x} \right) \quad \text{with} \quad K = \frac{\rho g \sin\theta}{\mu}. \quad (2.12)$$

$\mu$  is the viscosity of the Newtonian fluid. A new integration leads to the depth-averaged velocity

$$\bar{u}(x, t) = \frac{1}{h} \int_0^h u(x, y, t) dy = \frac{1}{3} K h^2 \left( 1 - \cot\theta \frac{\partial h}{\partial x} \right). \quad (2.13)$$

## 2.2. Suspensions rheology and migration models

Conservation of mass provides the governing equation for the flow depth  $h(x, t)$ , which is a nonlinear advection-diffusion equation

$$\frac{\partial h}{\partial t} + Kh^2 \frac{\partial h}{\partial x} = Kh^2 \cot\theta \left( \frac{\partial h}{\partial x} \right)^2 + \frac{Kh^3}{3} \cot\theta \frac{\partial^2 h}{\partial x^2}. \quad (2.14)$$

The only exact solutions are for horizontal bottoms ( $\theta = 0$ ), for which the governing equation reduces to a nonlinear diffusion equation[42]. In that case, the front position is given by

$$x_f(t) = \xi_f \left( \frac{\rho g V^3}{3\mu} t \right)^{1/5}, \quad (2.15)$$

with  $\xi_f = 1.411$ . Asymptotic solutions can be obtained at short and long times [43, 44] for equation (2.14) and  $\theta > 0$ . It can be shown that at short times the front position is given by (2.15) while at long times the front position is approximated by the first-order expression

$$x_f(t) = \left( \frac{9}{4} \frac{\rho g \sin\theta V^2}{\mu} t \right)^{1/3}. \quad (2.16)$$

## 2.2 Suspensions rheology and migration models

We focus on non-brownian, monodisperse spherical particles immersed in a Newtonian fluid whose density is the same as the particles (isodense). Brownian effects, colloidal forces and sedimentation are neglected. The most relevant questions that arise about the behavior of such suspensions are: i) what is the relation between shear stress and shear rate for such material and ii) how does the local concentration of particles evolve when the suspension is sheared. The purpose of this section is to discuss these two questions.

### 2.2.1 Effective viscosity

To describe the rheology of a suspension, one may assume, crudely, that the suspension can be modeled as a generalized Newtonian fluid such that  $\tau = \mu(\phi)\dot{\gamma}$ , with  $\phi$  the solid fraction. Identification of an appropriate expression  $\mu(\phi)$ , describing the increase of viscosity observed when solid material is added to a fluid, has been extensively attempted. Early studies started with Einstein's calculations at the beginning of the 20th century and the problem is still unresolved with theoretical work as well as experimental investigations facing problems at high solid fractions.

For dilute suspensions, Batchelor and Green [45] extended Einstein's work to second order and found  $\mu(\phi) = \mu_0(1 + 2.5\phi + 7.6\phi^2)$  in pure straining flow, with  $\mu_0$  as the viscosity of the suspending fluid. Until  $\phi \sim 10\%$ , a good agreement is found between the theory and experimental data. At higher concentration, contact between particles (frictional, collisional) may occur, increasing the complexity of the analytical calculations. To avoid these difficulties, several empirical

## Chapter 2. Theory

---

equations have been proposed. Both agree that the viscosity must diverge as  $\phi$  approaches a maximum  $\phi_m$  and that the Einstein's limit must be recovered at low concentration. However, the way in which the viscosity diverges near  $\phi_m$  and the value of  $\phi_m$  which must be used is still debated. Most of the discrepancies arise from the fact that macroscopic measurements were used to infer local rheology without taking into account any suspension inhomogeneities. Since the beginning of the century, new measurement techniques allow local measurement of the velocity and solid fraction and help to explain previous inconsistent observations.

The Krieger-Dougherty [46] model is one of the most widely used equation:

$$\mu_{\text{eff}} = \mu_0 \left(1 - \frac{\phi}{\phi_m}\right)^{-\beta}. \quad (2.17)$$

with  $\beta = 2.5\phi_m$  which recover the Einstein limit at low concentration. Setting  $\beta = 2.5\phi_m$  fits macroscopic measurements well (e.g data obtained in a rheometer from the torque and angular velocity) but fits local measurements poorly. Using MRI, Ovarlez [47] measured the local dependence of the viscosity on the solid fraction and found a good agreement between the experiment and equation (2.17) with  $\beta = 2$  and  $\phi_m = 0.605$  up to  $\phi = 0.6$ . Consistent with Ovarlez's observations, Mills and Snabre [48] showed, from a theoretical standpoint, that taking into account the formation of transient solid clusters leads to a  $(\phi_m - \phi)^{-2}$  singularity of the shear viscosity near  $\phi = \phi_m$  (the shear viscosity associated with hydrodynamic interactions leads to a  $(\phi_m - \phi)^{-1}$  divergence near jamming). More recently, Zarraga [49] proposed a new model with only one parameter

$$\mu_{\text{eff}} = \mu_0 \frac{\exp(-2.34\phi)}{\left(1 - \frac{\phi}{\phi_m}\right)^3}. \quad (2.18)$$

A good agreement was found between Zarraga's model predictions and the viscosity measurements made on an inclined plane by Bonnoit [31] with  $\phi_m = 0.62$ . However, defining an effective viscosity only partially describes the rheology since, most of the time, concentrated suspensions exhibit non-Newtonian behaviors. At small shear rate and for solid fractions higher than 45% shear-thinning was reported by many authors [49, 50] for non-colloidal suspensions. This behavior seems to be more pronounced when the polydispersity is high. Reardon et al. reported a  $\tau \sim \dot{\gamma}^\alpha$  law with  $\alpha$  as small as 0.5 for suspensions made with particles having a broad size distribution. For intermediate shear rates a Newtonian plateau is reached and suspensions have a purely viscous behavior [47]. At higher shear rates, however, a new transition occurs from the Newtonian regime, where  $\tau \sim \dot{\gamma}$ , to a Bagnoldian regime, where  $\tau \sim \dot{\gamma}^2$  [51]. Moreover, for highly concentrated suspensions ( $\phi > 50\%$ ), yield stress has been observed corresponding to a jamming of the particles inside the fluid. It is, however, unclear the exact concentration above which the yield takes place. Values between 55% and 64% were found depending on the particle shape, the size distribution, the shear rate, the particle

arrangement and the protocol used [52, 53, 54]. Above this fluidity limit the suspension can support a finite shear stress and hence exhibits the properties of a solid. Fall et al. [55], carefully matched the fluid density to the particle density and, using MRI, found no yield stress below 62%. They suggested that yield stress below 60% was spurious and only due to buoyant effects.

### 2.2.2 Migration

Shear-induced migration of particles plays a key role in suspension dynamics. Once a shear gradient is present in the flow, migration occurs and strongly affects the internal dynamics. The initially uniformly-distributed particles are rearranged to a non-uniform distribution. In free surface flows this phenomenon prompts particles to move to the free surface where the shear rate is smaller. Depletion of particles into the lower layers of the flow gives rise to a blunted velocity profile.

The first reports of migration date back to 1980; Gadala-Maria and Acrivos [56] observed a decrease of the total stress as they were shearing a suspension in a Couette device at constant angular velocity. Particles were migrating out of the sheared part of the sample to the reservoir containing the stagnant part of the suspension. Since this first report, migration was extensively studied and a lot of effort was made to try to predict the resulting inhomogeneities. Two different types of models emerged: diffusive flux models ([57, 58, 59]) and temperature models ([60, 61, 62]). Diffusive flux models assume that migration is a purely diffusive process and therefore is controlled by a diffusion equation. In contrast, temperature models treat the suspension as a two-phase fluid and thus it is required to solve a system of equations for mass and momentum conservation for both phases.

Shapley et al. [63] compared the two types of model in a Couette geometry and found that, with reference to the concentration profiles, both theories gave accurate results for a mean solid fraction between 30 and 50%. Ovarlez et al. [47] used the same geometry but with a higher solid fraction (59%). They observed that none of the models were able to accurately predict the concentration profile without tuning the empirical parameters. Nott and Brady [60] compared their temperature model with the Stokesian dynamics simulations and the diffusive flux predictions of Phillips et al. [58] in a pressure-driven flow geometry. They found significant differences in the concentration profile in the close vicinity of the center of the channel. Discrepancies arise from the fact that Phillips's theory is local and thus, predicts a maximum packing concentration  $\phi_m$  at the center of the channel where the shear rate is zero. However, the velocity profiles predicted by the two models were very similar and both were insensitive to the cusp in the concentration profiles of the diffusive flux theory. Timberlake and Morris [35] modified the temperature model of Nott and Brady [60] to take into account the normal stress jump which occurs at the free surface of a film of suspension flowing down an inclined plane. They found reasonable agreement between the theory and experimental data but with parameters free to take a range of values.

## Chapter 2. Theory

---

Here, we focus on the model by Phillips et al. [58] and the Mills and Snabre [64] theory. These two models are particularly interesting since they give an analytical expression of the concentration profile. Moreover, no tunable parameters are required and, under certain conditions, both theories predict the same concentration profile for a uniform free surface flow. Phillips modified the original diffusion model of Leighton and Acrivos [57] in order to describe the time evolution of the concentration. According to this model the conservation equation for the solid fraction  $\phi$  is given by

$$\frac{\partial \phi}{\partial t} + \mathbf{v} \cdot \nabla \phi = -\nabla \cdot (\mathbf{N}_c + \mathbf{N}_\mu) \quad (2.19)$$

with  $\mathbf{v}$  the velocity and  $\mathbf{N}_c$  and  $\mathbf{N}_\mu$  contributions arising from the spatially varying interaction frequency and spatially varying viscosity respectively. Equation (2.19) is valid only for a migration normal to the shearing surface in unidirectional shear flow.  $\mathbf{N}_c$  and  $\mathbf{N}_\mu$  are given by

$$\mathbf{N}_c = -K_c a^2 (\phi^2 \nabla \dot{\gamma} + \phi \dot{\gamma} \nabla \phi), \quad \mathbf{N}_\mu = -K_\mu \dot{\gamma} \phi^2 \left( \frac{a^2}{\mu} \right) \frac{\partial \mu}{\partial \phi} \nabla \phi \quad (2.20)$$

with  $a$  the particle radius,  $\dot{\gamma}$  the shear rate,  $\mu$  the effective viscosity and  $K_c$  and  $K_\mu$  two unknown constants. Solving (2.19) for a steady uniform flow down an inclined infinite plane (plane Poiseuille flow) and using a Krieger viscosity (2.17), we obtain

$$\phi(y) = \phi_w \frac{h}{h-y} \left( \frac{1 - \phi_w / \phi_m}{1 - \phi / \phi_m} \right)^{1.82 \left( 1 - \frac{K_\mu}{K_c} \right)} \quad (2.21)$$

where the subscript  $w$  refers to the bottom ( $y = 0$ ) and  $h$  is the flow depth. Fitting equation (2.19) to experimental data obtained in a Couette geometry using NMR, Phillips found a good agreement for  $K_c / K_\mu = 0.66$ . With this value the exponent of (2.21) is approximately equal to  $-1$  and equation (2.21) reduces to

$$\phi(y) = \frac{\phi_m}{1 + \alpha \frac{h-y}{h}} \quad \text{with} \quad \alpha = \frac{\phi_m}{\phi_w} - 1 \quad (2.22)$$

for  $0 \leq y \leq h$  with  $\phi_w = \phi(0)$ .  $\phi_w$  must be determined using the mean solid fraction contained in the suspension

$$\frac{1}{h} \int_0^h \phi(y) dy = \bar{\phi}. \quad (2.23)$$

Mills and Snabre [64] found the same expression for the steady profile using a model based on lubrication forces between colliding particles. As far as we know, expression (2.22) has not been tested against experimental data obtained in a flume. However, the same solution as

(2.22) applies to flows in a rectangular channel of height  $2h$  (pressure gradient replacing the gravitational driving force). Koh et al. [65] measured particles migration in such geometry using laser-Doppler velocimetry in a transparent suspension. They found partial agreement between their data and equation (2.22) especially at the center of the channel, where the theoretical concentration profile exhibits a sharp increase (see Figure 5.12). To improve the model in the low shear rate regions where it is deficient, Mills and Snabre [64] proposed to use a non-local stress tensor which provides much better agreement with experimental data [36, 66]. Physically this non-local tensor is supported by the idea that above a sufficiently high solid fraction (percolation threshold) a transient infinite cluster must appear in the suspension. Under this assumption they showed that the concentration profile is given by

$$\phi(y) = \frac{\phi_m}{1 + \alpha \left(\frac{h-y}{h}\right)^\kappa} \quad \text{with} \quad \alpha = \frac{\phi_m}{\phi_w} - 1 \quad (2.24)$$

with  $\kappa = 2$  for  $h - \xi \leq y \leq h$  and  $\kappa = 1$  for  $0 \leq y \leq h - \xi$ .  $\xi$  stands for the correlation length over which the transmission of stress through a transient connected network of particles apply. Assuming a correlation length of the same order as the flow depth  $\xi \cong h$ , we obtain:

$$\phi(y) = \frac{\phi_m}{1 + \alpha \left(\frac{h-y}{h}\right)^2} \quad \text{with} \quad \alpha = \frac{\phi_m}{\phi_w} - 1, \quad (2.25)$$

for  $0 \leq y \leq h$  with  $\phi_w = \phi(0)$ .

Theoretical velocity profiles for a steady uniform regime can be computed from the concentration profile assuming that the suspension can be modeled as a generalized Newtonian fluid characterized by a viscosity  $\mu(\phi)$ . The momentum equation (2.11) must be integrated between the bottom and the surface. Assuming a vanishing shear stress at the free surface, we have

$$\frac{du}{dy} = \rho g \sin \theta \frac{h-y}{\mu(y)}, \quad (2.26)$$

with the viscosity  $\mu(y)$  evaluated at the flow depth  $y$  using the viscosity function  $\mu(\phi)$  and the concentration profile  $\phi(y)$ .

## 2.3 Summary

In this chapter we examined different theoretical aspects of suspension dam-break that help in the discussion of the experimental results of Chapter 4 and 5.

A dam-break consists of the sudden release of a given volume of material down a slope. Analytical solutions cannot be found for the general problem. However, after the release, different regimes can be achieved by the flow, depending on which forces are dominant. For these balanced regimes it is sometime possible to find solutions having made certain

assumptions. In particular, when the fluid is Newtonian and the characteristic length of the flow is much greater than the typical flow depth (lubrication theory), it is possible to show that the front position scale at long times is  $x_f(t) \sim t^{1/3}$  on an inclined bed and  $x_f(t) \sim t^{1/5}$  on horizontal surfaces. Furthermore, the velocity profiles are parabolic with an amplitude modulated by the free surface curvature.

At low solid fractions, suspensions behave as viscous fluids and can be approximated by a Newtonian rheology. However, at higher concentrations, suspensions exhibit complex features which are not completely understood, due to the inhomogeneities that take place in the flow and the multiple types of interactions between particles [67]. Many empirical equations were adapted in order to compute an apparent viscosity for concentrated suspension but these were only partially successful, often exhibiting geometry and/or product dependencies. These discrepancies arose from the fact that macroscopic measurements were used to infer local rheology without taking into account suspension inhomogeneities. As soon as a gradient of shear occur in a suspension, particles migrate from the high shear rate zone to the low shear rate area. In free surface flows this phenomenon prompts particles to move to the free surface where the shear rate is smaller. Depletion of particles into the lower layers of the flow gives rise to a blunted velocity profile.



## 3 Material and methods

Until the late 1980s, a major obstacle in gaining insight into the rheology of concentrated suspensions was the lack of measurement techniques able to provide velocities or solid concentrations within the flowing material. Measurements taken at the sidewalls are only poorly representative of what really happens at the center of the flow and inferring local rheology from macroscopic measurements leads to incomplete or wrong results. In the last 20 years, to bypass these problems, a large number of non-intrusive experimental techniques have been developed and tested in order to measure the local velocity and/or the solid fraction far from the sidewalls.

The most commonly used methods are Magnetic Resonance Imaging (MRI) [47, 68], Laser Doppler Velocimetry (LDV) [63, 36, 66, 65] and Particle Image Velocimetry (PIV) [40, 69] in index-matched suspension or Ultrasonic Pulsed echo Doppler (UVP) [70]. In this work, we used Particle Image Velocimetry (PIV) with index-of-refraction matching of the solid and liquid phases for three main reasons:

- PIV is able to provide an instantaneous 2D velocity map ( $u(x, y), v(x, y)$ ) at high frequency ( $f > 1000$  Hz) and consequently suits the transient nature of dam-break flows well (an MRI measurement usually takes several seconds and LDV gives velocity in only one point in the fluid);
- PIV gives a direct picture of the particles in the suspension, and thus can help identifying problems like slip or bubbles;
- this technology was already partially available in the lab.

However, there are also drawbacks to this technique. Reliable measurements of the solid concentration require a level of image quality impractical in our thick flows. PIV requires transparent suspensions made up of chemical compounds that have a limited toxicity when used in small enclosed experiments, which require special care when used in open setup. Most of the time these products are highly sensitive to temperature and humidity changes, and this imposes a rigorous experimental protocol since careful refractive index matching is

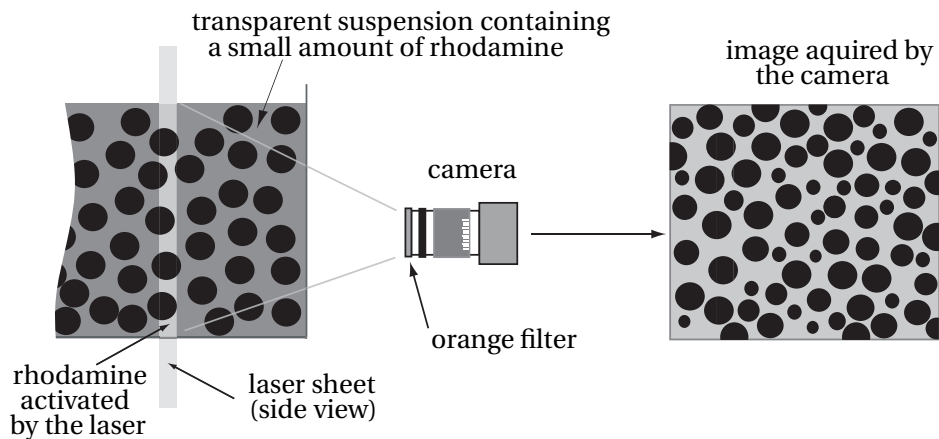


Figure 3.1: Overview of the method used to see particles located in the center of the concentrated suspension.

necessary to obtain reliable data. The price of the product can also be prohibitive when a large quantity of material is needed. To summarize, while the principle of PIV in index matched suspensions is straightforward, its implementation is far less simple.

We organized the present chapter as follows: First we briefly describe the technique, then we explain how transparent suspensions were obtained and finally we give a description of the experimental setup, instrumentation and protocol.

### 3.1 Particle Image Velocimetry (PIV) in concentrated suspensions

PIV is based on image correlation. A slice of fluid where the velocity measurement has to be performed is lit by a laser sheet. Two pictures of the illuminated particles are acquired at two different times. Each frame is subdivided in small regions (interrogating windows), each region containing a specific pattern of particles. A displacement map between the two pictures can then be computed using cross-correlation on each interrogating window. Dividing the displacement by the time between the two images leads to the velocity map [71].

In order to obtain images of the particles at the center of a concentrated suspension we proceed as follow. First, the bulk is made transparent using a mix of fluid with the same refraction index as the particles. Then, a small amount of rhodamine (a fluorescent dye) is added to the fluid in order to differentiate it from the solid phase. Therefore, when exposed to the laser sheet, particles located in the illuminated slice appear as black disc due to the absence of fluorescent compound. Conversely, the rhodamine in the liquid phase fluoresces, emitting an orange light (see Figure 3.1). To improve image quality, an orange filter is added in front of the camera removing the green light of the laser and keeping only the light emitted by the rhodamine.

Note that this method is slightly different from classical PIV. Usually, to measure velocity in clear fluids, the liquid is seeded with small particles. When lit by the laser, particles appear as

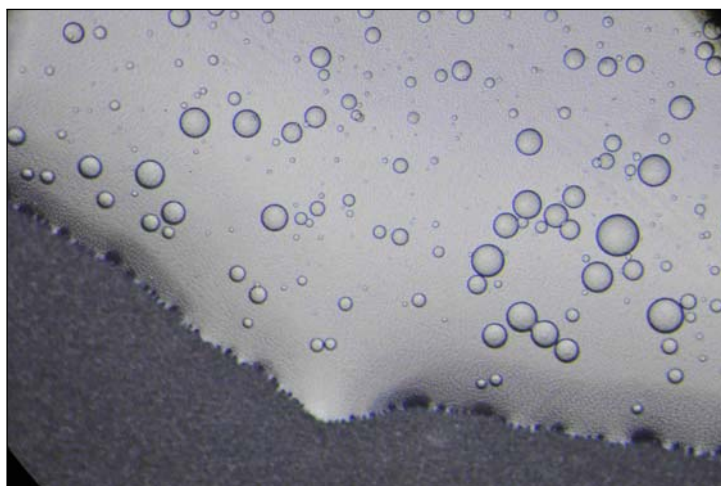


Figure 3.2: Picture of a drop of suspension. We used a fluid with a refractive index different from the refractive index of the particles in order to underline beads contour.

white dots on images, allowing tracking and displacement computation. Using classical PIV technique was not possible in our case due to strong reflections induced by the free surface (in particular close to the front of the flow). Moreover, adding small particles in concentrated suspensions can lead to dramatic changes in suspension rheology.<sup>1</sup>

### 3.2 Transparent suspensions

We used PMMA (polymethylmethacrylate) beads provided by Altuglas International SA (92257 La Garenne-Colombes, France). These particles are characterized by a good sphericity (see Figure 3.2) and excellent optical properties (constant refractive index, few impurities). In addition, as these particles are produced industrially, they are relatively inexpensive. All particles used came from a single batch in order to ensure reproducibility. The refractive index  $n = 1.48847 \pm 0.00005$  and the density  $\rho_p = 1.1840 \pm 0.0005$  of the beads were determined using the same methods as described in Wiederseiner [39]: The refractive index was obtained by measuring the laser intensity transmitted through a sample of suspension, and sedimentation tests were carried out to measure the density. Two particle size distributions were tested (see Figure 3.3), a raw distribution ( $d = 113 \mu\text{m}$ ,  $\sigma = 65 \mu\text{m}$ ) and a sieved distribution ( $d = 191 \mu\text{m}$ ,  $\sigma = 59 \mu\text{m}$ ). In the later case, PMMA particles were sieved using a sieving machine (Retsch AS200 Control) and a  $180 \mu\text{m}$  sealed sieving stack.

The random close packing  $\phi_{\text{RCP}}$  for the two distributions was measured by pouring a mass  $M_p$  of dry beads into a calibrated round-bottom flask of volume  $V_c$ , and vibrating the cylinder until steady compaction occurred. Then,  $\phi_{\text{RCP}}$  was computed using the particle density:  $\phi_{\text{RCP}} = M_p / (\rho_p V_c) = 0.655 \pm 0.02$ . Since possible errors are likely to come from partial packing

<sup>1</sup>We tried to add 1.5 g of titanium dioxide  $\text{TiO}_2$  (particles diameter  $\sim 2 - 5 \mu\text{m}$ ) to 15 kg of concentrated suspension (solid fraction 59%, mean diameter of the particles  $191 \mu\text{m}$ ), the distance traveled by the flow was divided by a factor 2.

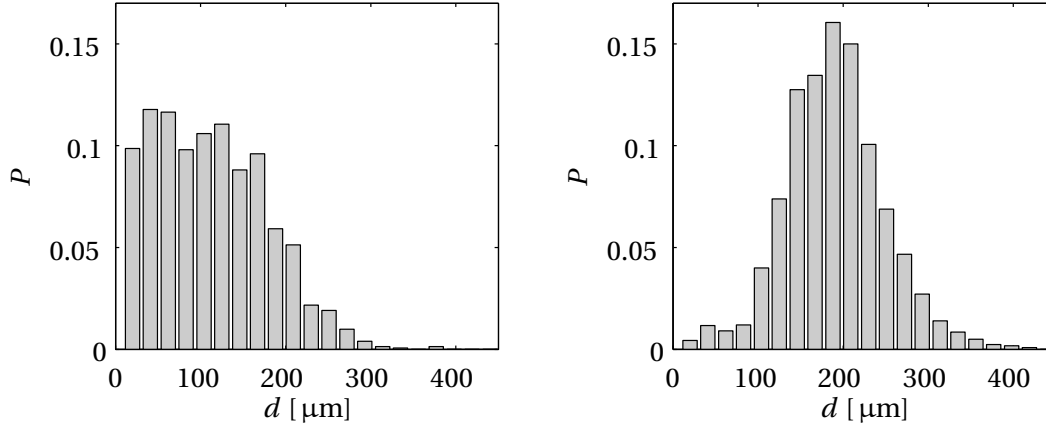


Figure 3.3: Grain size distributions of PMMA particles used in our experiments. Histograms were obtained by measuring particles diameters with a microscope (Olympus BX60). Left: raw grain size distribution (sample size: 1520 particles). Right: grain size distribution after sieving (sample size: 3427 particles).

or cluster formation due to electrostatic effects,  $\phi_{\text{RCP}} = 0.655 \pm 0.02$  represents a lower bound of the estimation of the random close packing. We were not able to detect significant influence of the particle distribution on  $\phi_{\text{RCP}}$ , due to the limited precision allowed by the method.

To match the refractive index and the density of the particles at the same time, we used the same fluid composition as Lyon and Leal [36] and Wiederseiner [39, 40]. The fluid mixture was made up with three components: Triton X100, 1,6-Dibromohexane (DBH) and UCON oil 75-H450 (Dow Chemicals) which closely match the refractive index and density of beads. The mixture viscosity was measured using a Bohlin Gemini CVOR 200 (Malvern) rheometer with a Couette geometry,  $\mu_f = 0.124 \pm 0.003$  Pa s at 20.0 °C. Surface tension of the fluid  $\gamma = 33 \pm 5$  mN m<sup>-1</sup> was determined using the pendant drop method [72, 73], the Laplace equation of capillarity was fitted to the shape and dimensions of a pendant drop.

### 3.2.1 Suspensions preparation and handling

Before each experiment, the suspension had to fulfill the following requirements:

- a refraction index of the fluid between  $n = 1.48820$  and  $n = 1.48880$  at 20.0 °C in order to have a clear suspension;
- a density of the fluid between  $\rho = 1.1835$  and  $\rho = 1.18345$  at 20.0 °C to avoid sedimentation and buoyancy effects;
- no air bubbles trapped inside the suspension;
- particles homogeneously distributed inside the bulk to ensure reproducibility of the

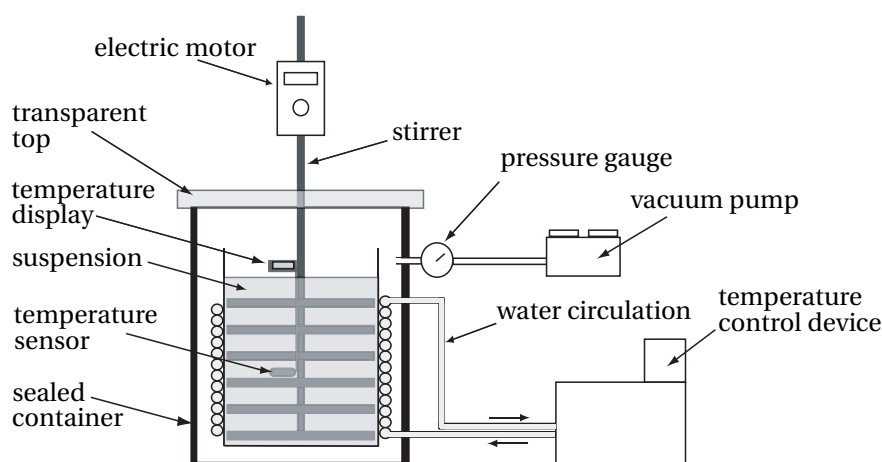


Figure 3.4: Sketch of the setup used during the outgassing process. The suspension was stirred in the sealed container under a vacuum. The temperature was controlled using a water cooling circuit. The top of the container was made transparent to check the general aspect of the suspension. This system allowed us to prepare, outgas and control the temperature of 20 kg of suspension containing up to 60% of particles.

experiments;

- a constant temperature of  $20.0 \pm 0.1$  °C everywhere in the material since viscosity, density and refraction index are very sensitive to temperature.

After many trials and errors, we ended with the following method to prepare the suspension:

1. Two binary mixtures of fluids with a density  $\rho = 1.1840$  at 20 °C were prepared. The first was obtained mixing UCON oil with DBH and the other was obtained mixing Triton X100 with DBH. The refraction index of the first mixture was below the target refraction index  $n = 1.48850$  whereas the refraction index of the second mixture was above  $n = 1.48850$ . As Triton X100 has a hydrophilic polyethylene oxide group, Triton-based solutions often absorb small quantities of water vapor, which markedly changed the refractive index of the solution. To prevent this disturbing effect we reduced exposure of the fluid to the ambient air as much as possible.
2. The two binary mixtures were mixed together to produce a resulting fluid with a refraction index  $n = 1.48850$ .
3. Particles were added to the fluid until the desired concentration was obtained. A small amount of rhodamine (typically less than 0.5 g) was added.
4. The whole mix was then vigorously stirred by hand before being placed for 12h under vacuum (pressure below 50 mbars) in a sealed cylindrical container. At the same time

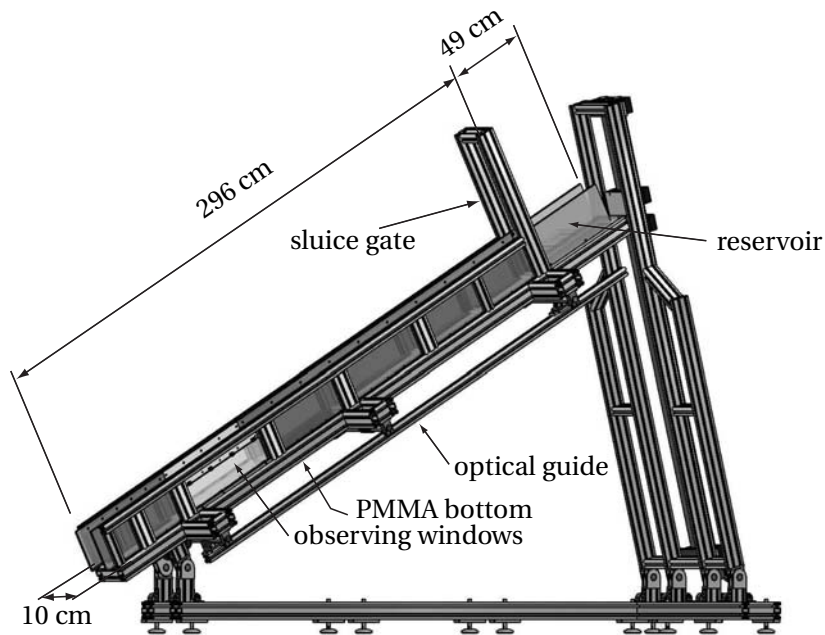


Figure 3.5: Sketch of the channel used for the dam-break flows.

the suspension was stirred at 5 rpm using a 6-blade propeller in order to remove all air bubbles and water.

5. At the end of the outgassing process, the suspension temperature was generally a few degrees too high. While still keeping the suspension stirred under vacuum to avoid air bubble, the mix was cooled to  $20.0 \pm 0.1$  °C inside the container using a water circuit connected to a thermal bath (see Figure 3.4).
6. The sealed container was opened and the suspension gently poured into the reservoir using a 600 ml syringe.
7. During the flume experiments, the suspension was exposed to the ambient air and thus absorbed water vapor. In addition, a lot of air bubbles were created when the suspension was removed from the flume at the end of the experiment. For these reasons, the outgassing process was reiterated before each experiment. This allowed also an homogeneous redistribution of the particles through the suspension.

## 3.3 Experimental setup

### 3.3.1 Flume

To conduct our dam-break experiments we built a 3.5 m long and 10 cm wide flume. Figure 3.5 shows a sketch of the apparatus. The bottom was made of 13 mm thick PMMA, whose surface in contact with the flow was made rough to avoid any unwanted slip effect. To avoid any

optical artifacts due to this wavy interface and to guarantee clear optical access from below, the PMMA used was the same as that used for the beads (i.e. same refractive index).

A glass pane, located 50 cm from the flume outlet, was inserted to observe the flows from the side. The flume could be inclined from  $0^\circ$  to  $35^\circ$ . Its position was accurately controlled using a digital inclinometer (Level Developments Ltd) with a precision of  $0.1^\circ$ . The upper part of the flume was equipped with a sluice gate mounted on a pneumatic jack (SMC Pneumatik AG) and was used as a reservoir. The jack was quickly raised by injecting air pressured at 7 MPa, which made it possible to lift the gate within 0.5 s. An electromagnetic sensor located on the jack gave the reference time for the experiment and synchronized the other instruments. In order to keep the temperature of the suspension constant during the experiment, the flume was enclosed in an isolated room, whose temperature was fixed at  $20.0 \pm 0.2^\circ\text{C}$  using a fan coil unit.

#### 3.3.2 Instrumentation

Figure 3.6 explains how we measured the velocity profiles from below using the Scheimpflug principle. Filming from the side did not allow measurement of velocities within the head far from the sidewall due to the strong curvature in both directions and the shallow flow of the front. On the other hand, filming from below gave direct optical access to the vertical plane passing through the centerline, but the disadvantage of this configuration was that a large part of the filmed plane was out of focus. To avoid this problem, we adjusted the inclinations of the camera CCD and the lens so that the Scheimpflug rule was satisfied (the image was then in focus). A prism (made from a PMMA block, with the same refractive index as that of the flume bottom) was also needed to improve the field of view captured by the camera. A typical raw image obtained with this technique in a flowing suspension is shown in Figure 3.7.

A Basler A504k camera (working in the 200-1000 Hz range, depending the velocity of the flow), mounted with a Nikkor 105 mm macro lens and an orange filter was used to acquire images of the flow. The Laser was a dual head, diode pumped, Q-switched Nd:YLF Laser (Litron LDY 303) working at  $\lambda = 527\text{ nm}$  (green). At  $f = 1\text{ kHz}$  the release energy per laser pulse was 20 mJ. The laser sheet was created beneath the channel using a spherical lens (focal length 150 mm) coupled with a cylindrical lens (focal length 100 mm). Then, the beam was deflected in a direction perpendicular to the bottom with a  $150 \times 25\text{ mm}^2$  mirror, tilted at  $30^\circ$  (lenses and mirrors were provided by CVI Melles Griot). An aluminum pinhole was positioned between the laser and the lenses to improve the beam quality and reduce the laser sheet thickness to about  $150\text{ }\mu\text{m}$ . Optical devices were mounted on linear stages and could be precisely positioned and shifted from one side of the flume to another.

Front position was tracked using two Basler A403kc cameras positioned on the top of the channel and working in the 30-100 Hz range with a resolution of  $300 \times 2300$  pixels. The cameras and laser were synchronized using a pulse generator from Berkeley Nucleonics Corporation.

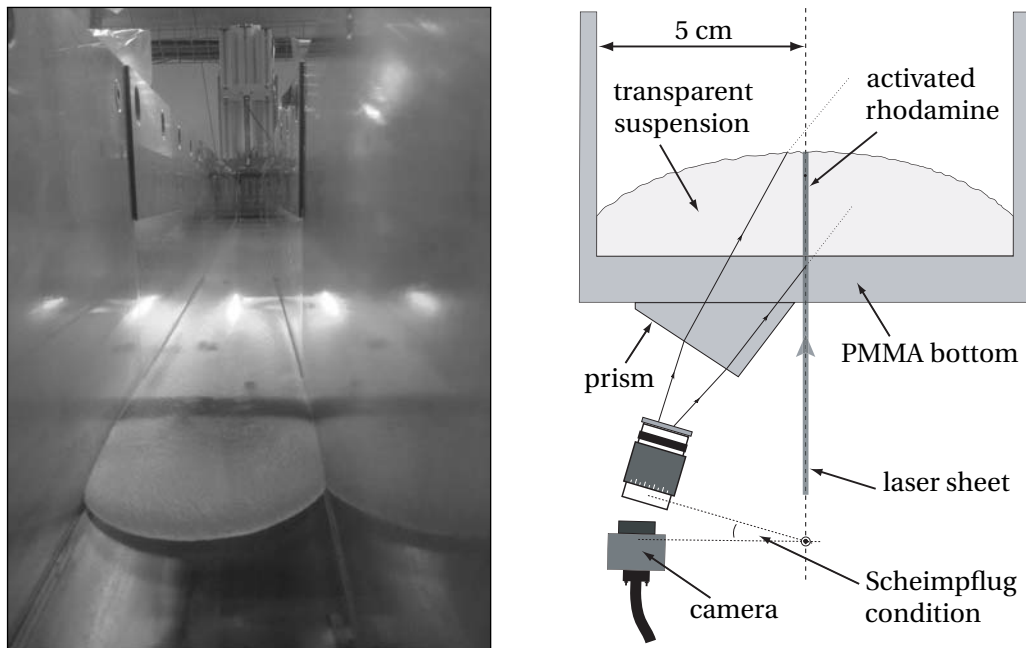


Figure 3.6: Left: picture of the flow in the measurement window. Right: Sketch of the system used to measure velocity profiles within the moving suspension. Strong curvature in both directions and flow shallowness of the front imposed measurements from below.

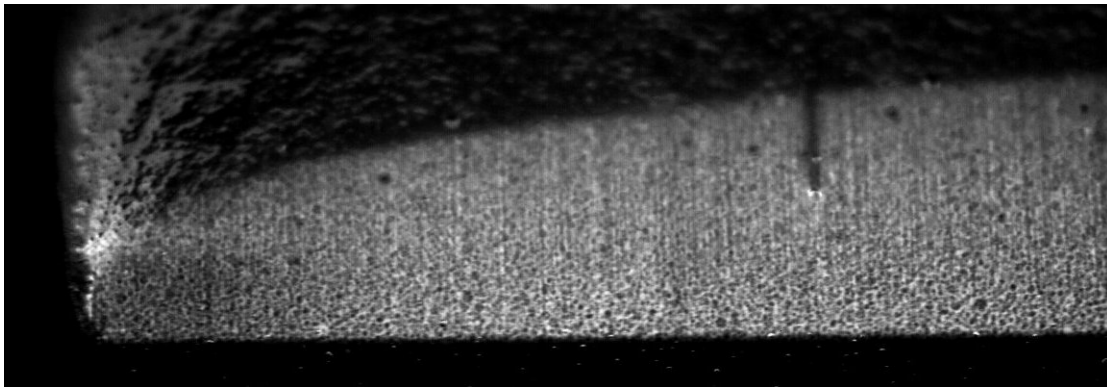


Figure 3.7: Typical raw image taken by the camera from the bottom of the flume. The black dots are the PMMA particles whereas the white area is produced by the rhodamine contained in the fluid. The corrugated free surface can be distinguished at the top of the picture and near the front, the vertical thick black line on the right of the image was due to a small bubble trapped within the flow. The picture was taken at the centerline of the flume, the solid fraction was  $\phi = 0.52$ , and the flow depth  $\sim 1.5$  cm.



### 3.3.3 Calibration and image processing

Velocity fields were computed on raw images using the open source software MatPIV<sup>2</sup> developed by J.K. Sveen. In order to return to physical coordinates, a calibration image was acquired prior to each run. The following procedure was used to acquire the calibration image: i) The flume was closed upstream and downstream of the field of view. ii) An "optical standard" was installed in the laser sheet plane. iii) A clear fluid with the same refraction index as the suspension was added until the optical standard was completely immersed.

Knowing the physical coordinates of 25 control points situated on the optical standard allowed us to define a transformation matrix linking image coordinates and physical space:  $T : (x_{\text{img}}, y_{\text{img}}) \rightarrow (x, y), \mathbb{R} \rightarrow \mathbb{R}$ . The *cp2tform* function of the Matlab Image Processing Toolbox was used to define the transformation  $T$ . Then, each velocity vector calculated with MatPIV on the raw images was converted with  $T$  to get its corresponding value in the physical space. Positioning errors using this calibration procedure were below 0.1 mm on the whole field of view.

Finally, to reject spurious velocity vectors, signal-to-noise filters and peak-height filters were applied to the data. Other PIV software (e.g. DPIVsoft<sup>3</sup>) was also tested to validate results computed with MatPIV.

## 3.4 Summary

We developed an experimental facility to accurately measure velocity profiles inside concentrated granular suspensions flowing down an inclined channel. In order to conduct our experimental campaigns we built a 3.5 m long by 10 cm width flume that could be inclined from 0 to 35°. A reservoir containing up to 10 liters of fluid was located in the upper part of the flume and closed with a pneumatic controlled gate. Velocity profiles were obtained using Particle Image Velocimetry (PIV) and index-of-refraction matching of the solid and liquid phases. We used transparent PMMA beads (mean diameter  $\sim 200 \mu\text{m}$ ) and a mixture of three fluids was used as interstitial fluid. The interstitial fluid was adapted in order to match the refraction index and the density of the solid phase. This system allowed us to prepare, outgas and control the temperature of 20 kg of suspension containing up to 60% of particles. Using a dual head pulsed laser and high speed cameras we were able to measure the velocity profiles at frequencies up to 1000 Hz. Two additional cameras tracked the front position along the flume with a frequency of 30 Hz and a spatial resolution of 1 mm.

<sup>2</sup><http://folk.uio.no/jks/matpiv/>

<sup>3</sup><https://www.irphe.fr/~meunier/>



## 4 Dam break of Newtonian fluids

In this chapter we report experimental results on dam-break flows involving Newtonian fluids. The setup introduced in Chapter 3 was used to measure front positions as well as velocity profiles inside the flowing material. Different slopes and released masses were tested. We had two main motivations for this work. i) We wanted to test the precision of our measurement procedure on simple fluids for which results far from the front of the flow are well known (i.e. near a steady uniform regime the velocity profile has a parabolic shape). ii) The flow of a fixed volume of Newtonian fluid down an inclined surface or a flume has attracted considerable attention over the last decades owing to its importance and relevance to a wide range of applications in nature or industry. Coating films [74], the design of consistometers in food industry [75] or first approximations to the rheological behavior of complex slurries in geophysical fluid mechanics [76, 77] are examples among others. Surprisingly enough, in spite of this considerable interest, we found no report on velocity measurements within the head of fluid avalanches far from the sidewalls, most of the existing studies focusing on macroscopic features such as the flow depth profiles [76, 78, 79, 44] or the front position as a function of time [42, 43]. From a theoretical standpoint, computing velocities in a dam-break flow is difficult due the transient nature of the problem. An easy way to obtain an estimation of the velocity is to assume that the characteristic longitudinal lengthscale along the bed is much greater than the typical layer thickness (lubrication theory). Under this hypothesis, the velocity profile takes a parabolic shape, whose amplitude is modulated by the free surface curvature (see 2.1.1). Basically, our idea was to test the reliability of the lubrication theory near the front of the flow where the assumption of a small aspect-ratio is not fully valid.

### 4.1 Fluids and procedures

For Newtonian fluids, we used three liquids: 98.5% glycerol solution (density  $\rho = 1260 \text{ kg m}^{-3}$ , viscosity  $\mu = 1110 \text{ mPa s}$ , surface tension  $\gamma = 51 \pm 6 \text{ mN m}^{-1}$  at  $20.0 \text{ }^\circ\text{C}$ ), pure glycerol (density  $\rho = 1260 \text{ kg m}^{-3}$ , viscosity  $\mu = 1490 \text{ mPa s}$ , at  $20.0 \text{ }^\circ\text{C}$ ), both manufactured by Reactolab (Switzerland), and Triton X100 (density  $\rho = 1067 \text{ kg m}^{-3}$ , viscosity  $\mu = 468 \text{ mPa s}$ , surface

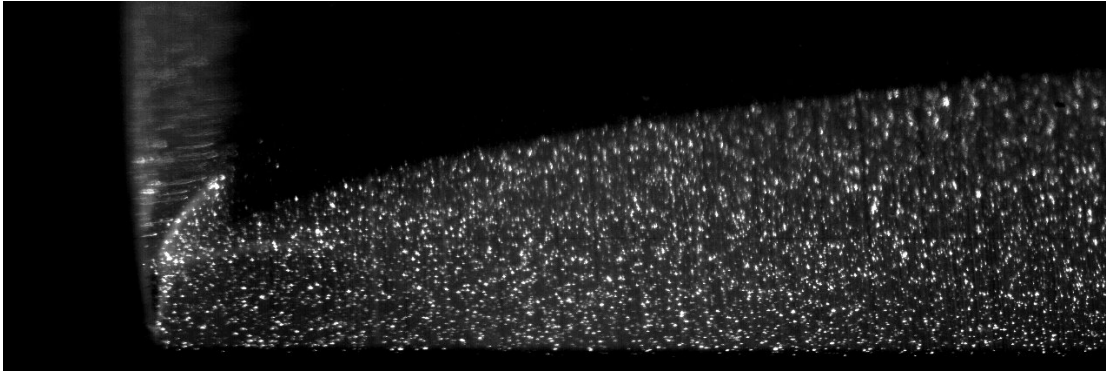


Figure 4.1: A typical image recorded by the camera ( $\theta = 9$  deg,  $m = 6$  kg), field of view:  $4 \times 2$  cm<sup>2</sup>. At the front of the flow particles out of the focus plane were lit due to the strong free surface curvature of the flow. However, there were no alterations on the area of the image used to compute velocity profiles and thus no noisy effects were observed on the data. The image was taken at the centerline of the flume, i.e. 5 cm from the sidewalls.

tension  $\gamma = 32 \pm 8$  mN m<sup>-1</sup> at 20.0 °C) produced by Interchim Bioscience (Switzerland). The viscosity was measured using a Bohlin CVOR rheometer equipped with a cone and plate geometry; the density was measured using an aerometer to within 1%. The refractive indices of glycerol ( $n = 1.4710$  for the 98.5% solution) and Triton ( $n = 1.49171$ ) were sufficiently close to the PMMA refraction index  $n = 1.48835$  to allow measurements through the rough bottom of the flume.

Since we used Particle Imaging Velocimetry to measure the velocity profiles, all of our fluids were seeded with polyamid particles to enlighten internal dynamics. The particles (manufactured by Dantec Dynamics, mean diameter 20  $\mu$ m) were marked with rhodamine by leaving them in a concentrated rhodamine solution (maintained at 60 °C) for one month. They were then rinsed with alcohol several times to avoid subsequent contamination of the samples by rhodamine. Fluorescent particles were used instead of classical PIV particles in order to filter out reflections of the laser light at the free surface, Figure 4.1 shows a typical image obtained with this technique. Instrumentation, calibration and image processing are described in Chapter 3. The great attention was paid to controlling the temperature of the fluid as precisely as possible since the viscosity of glycerol is very sensitive to temperature [80]. All measurements were taken at the centerline of the flume (i.e. 5 cm from the sidewalls).

## 4.2 Results

Table 4.1 summarizes the different runs presented in this chapter. Since the bed inclination had a direct influence on flow velocity, this was the main parameter we altered to explore the dynamical features of fluid avalanches under different flow conditions. In order to detect eventual size effects or surface tension effects, we also tested different masses and fluids.

Table 4.1: Features of the 8 runs: fluid used, density  $\rho$ , dynamic viscosity  $\mu$ , flume inclination  $\theta$ , initial mass  $m$  and flow Reynolds number  $Re = \rho \bar{u} h / \mu$  where  $\bar{u}$  and  $h$  denote the depth-averaged velocity when the flow depth is maximum and the maximum flow depth measured within the body.

Run	Fluid	$\rho$ (kg m <sup>-3</sup> )	$\mu$ (mPa s)	$\theta$ (deg)	$m$ (kg)	$Re$
(a)	98.5%-glycerol	1260	1110	0	6	0.08
(b)	98.5%-glycerol	1260	1110	1	6	0.40
(c)	98.5%-glycerol	1260	1110	3	6	1.55
(d)	98.5%-glycerol	1260	1110	6	6	6.70
(e)	98.5%-glycerol	1260	1110	9	6	9.33
(f)	98.5%-glycerol	1260	1110	6	3	1.13
(g)	pure glycerol	1260	1490	25	1	0.27
(h)	Triton X100	1067	468	6	3	9.11

Although emphasis is given to the velocity field within the head, we begin with a discussion about front positions as a function of time in order to characterize the flow regime when the surge crosses the observation window.

### 4.2.1 Front positions

Figure 4.2 illustrates the time variation of the front positions  $x_f(t)$  obtained experimentally for the eight different runs. As expected from equations (2.15) and (2.16), after a transition time, flows tended to reach an asymptotic behavior where  $x_f(t) \sim t^n$  with  $n = 1/5$  when the flume was horizontal and  $n = 1/3$  when the flume was inclined. In the log-log representation of Figure 4.2 this behavior is characterized by experimental data approaching straight lines of slope  $n$  at long time. In order to have a better idea of how well asymptotic behaviors were reached by the flows, we plotted the local value<sup>1</sup> of  $n$  along the channel on Figure 4.3.

For run (a) ( $\theta = 0$ ), convergence to  $n = 1/5$  was very fast, at  $x = 150$  cm (i.e. 100 cm from the gate), the value of  $n$  was already 0.22 and decreased slowly to 0.2. On Figure 4.2 we also report the theoretical front position given by (2.15) (solid line) and the numerical solution of (2.14) (dotted line). The gap between the two solutions when  $t$  tends to 0 comes from the initial conditions: the numerical computation of (2.14) takes into account the fact that the fluid is contained in a reservoir of a given size whereas the asymptotic equation assumes that the initial profile is a column of fluid of infinite height and no width. After  $t \sim 2$  s ( $x_f \sim 135$  cm) the two solutions became indistinguishable. Agreement between theoretical and experimental front positions was good at sufficiently long time when inertial effects have been dissipated. The time necessary for comparability of inertial and viscous forces is given by  $t_e \sim (m^4 \rho^{-1} l^{-4} g^{-2} \mu^{-3})^{1/7}$  with  $l$  the width of the flume (see [42]). Asymptotic behavior is observed when  $t \gg t_e$ . In our case, for run (a),  $t_e = 1.9$  s corresponding to a downstream coordinate  $x \sim 120$  cm. Strikingly on Figure 4.3 this distance corresponds to the beginning of

<sup>1</sup>The value of  $n$  at the downstream position  $x$  was computed by making a fit on the  $x_f(t)$  data with  $|x_f(t) - x| < 5$  cm.

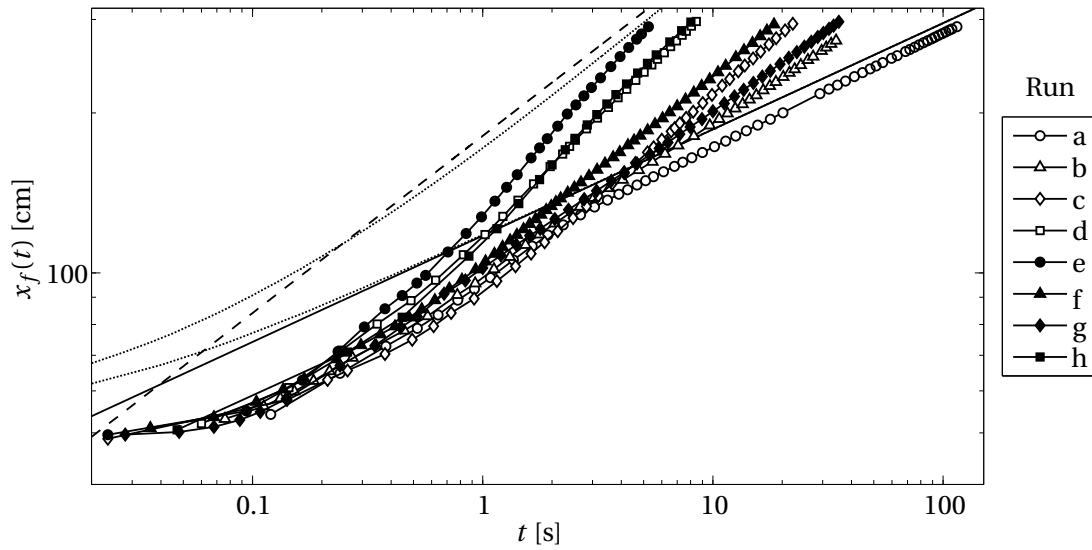


Figure 4.2: Front position as a function of time for the eight runs. The dashed line represents the asymptotic solution (2.16) for run (d) whereas the solid line stands for the horizontal solution (2.15) computed for run (a). Dotted lines correspond to the numerical solutions of (2.14) in the two cases.

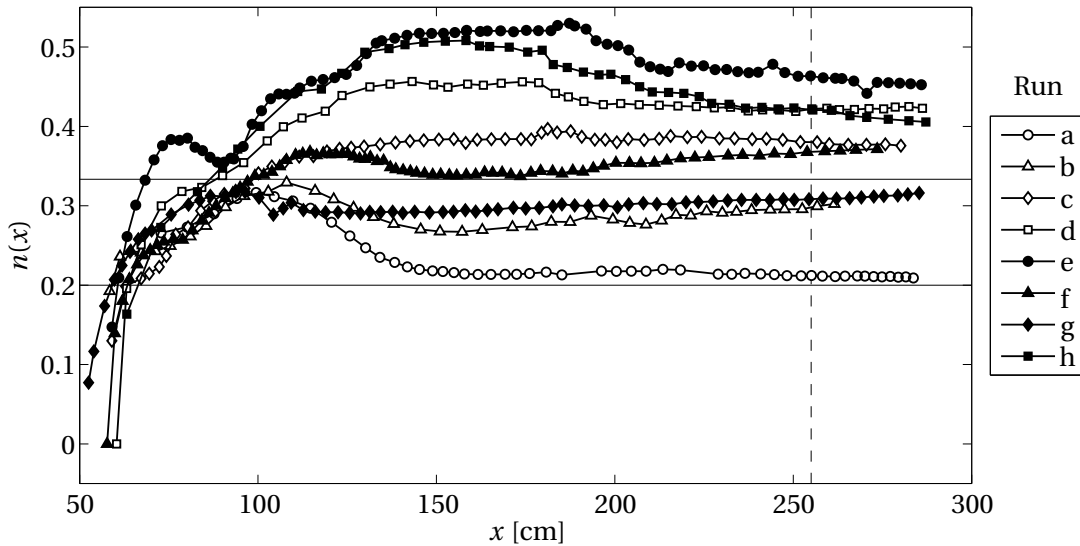


Figure 4.3: Local fit for front positions presented in Figure 4.2 using a function  $f(t) = At^n$ . Asymptotic values for  $n$  predicted by the theory,  $n = 1/5$  when  $\theta = 0$  and  $n = 1/3$  if  $\theta > 0$  are also shown (solid horizontal lines). The vertical dashed line indicates the position of the measurement window used for the velocity profiles ( $x_0 = 255$  cm).

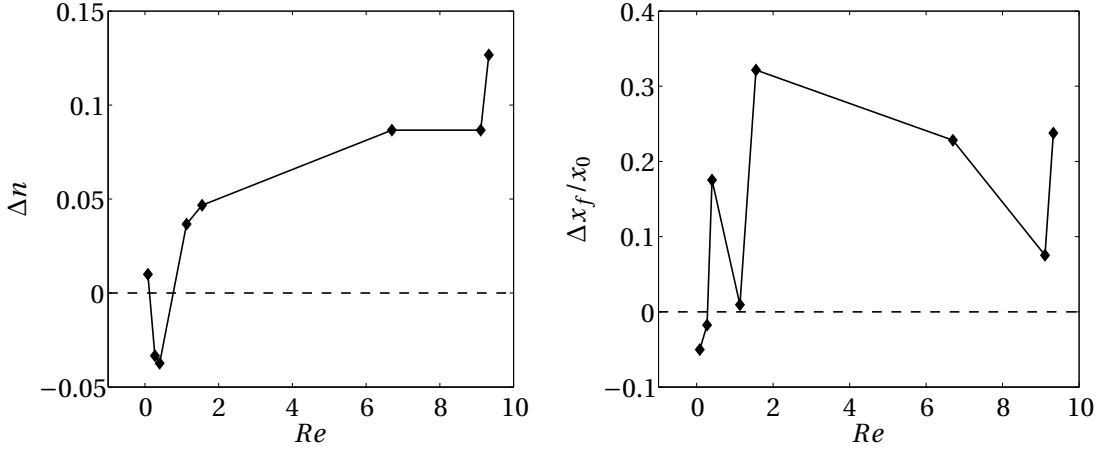


Figure 4.4: Left: the gap between theoretical  $n$  (i.e.  $n = 1/5$  for  $\theta = 0$  and  $n = 1/3$  for  $\theta > 0$ ) and experimental  $n$  as a function of the Reynolds number  $Re = \rho \bar{u} h / \mu$  (see Table 4.1). Measurements were taken at the downstream coordinate  $x_0 = 255$  [cm]. Right: the relative gap between theoretical front positions predicted by equation (2.14) and experimental front positions at the downstream coordinate  $x_0 = 255$  [cm].

the region where the values for  $n$  stabilize and converge to the asymptotic value 0.2. At the outlet of the channel, agreement was very good and discrepancies were smaller than 10 cm, i.e. less than 4%.

Convergence to the asymptotic solution  $x_f(t) \sim t^{1/3}$  was observed at various degrees for runs (b) to (h) ( $\theta > 0$ ), depending on the Reynolds number of the flow. When  $Re$  was small,  $n$  was very close to the value asymptotically expected. Conversely, for larger Reynolds,  $n$  increased to 0.46 (run (e),  $Re = 9.33$ ). These results are summarized on the left hand plot of Figure 4.4. The difference between the experimental and theoretical results for  $n$  is shown as a function of  $Re$ . When  $Re$  was smaller than 2,  $\Delta n$  did not exceeded 0.05, whereas  $\Delta n$  increased to 0.13 for  $Re \sim 10$ . Despite these differences regarding the convergence time, all runs seemed to tend to  $n = 1/3$  (Figure 4.3).

The right plot of Figure 4.4 shows the relative gap  $\Delta x_f / x_0$  between the theoretical and experimental front position observed at  $x_0 = 255$  cm. Theoretical front positions were computed using (2.14). For small Reynolds numbers, the agreement between theory and experiments seemed better ( $\Delta x_f / x_0 < 20\%$ ) than at higher Reynolds numbers ( $\Delta x_f / x_0 < 35\%$ ). However, front positions were always over-predicted by the theory except in runs (g) and (a). Discrepancies originate predominantly from sidewall friction and inertial effects (see [38] for a detailed discussion on the contribution of each effect to the discrepancies).

Since measurements for flow depth were also available from PIV images, we tested the validity of the lubrication theory for the flow depth evolution. Figure 4.5 shows the height variation measured at  $x_0 = 255$  cm (solid line) and the numerical solution of equation (2.14) (time

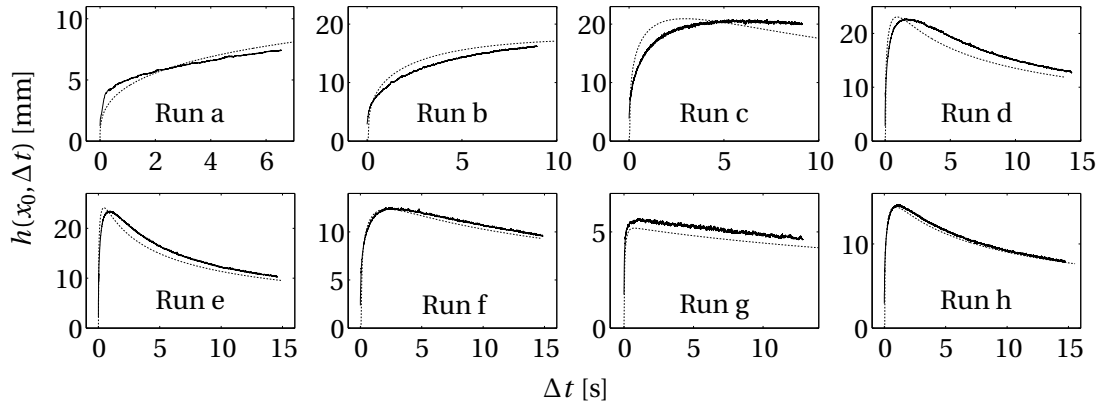


Figure 4.5: Flow depth variation measured at  $x_0 = 255$  cm (solid line) and numerical solution of equation (2.14). Because of the delay in the experimental front position relative to the computed front position, the time axis of the theoretical curve  $h(x_0, t)$  has been shifted so that the curves have the same starting point to facilitate comparison.

shifted). The height of the flow was always well captured by the theory and discrepancies remained smaller than 10%. As expected, the main discrepancies arose near the front of the flow since the small aspect-ratio hypothesis used to obtain equation (2.14) is no longer valid in this region.

#### 4.2.2 Velocity profiles

Due to the successful predictions given by lubrication theory on front positions and depth evolutions, we expected the velocity profiles to be well described by (2.12) as well, at least far from the front. We therefore aimed to answer two questions: i) does the theoretical parabolic shape fit the experimental data; ii) does the corrective term  $\left(1 - \cot\theta \frac{\partial h}{\partial x}\right)$  that take into account the free surface curvature accurately predict the magnitude of the velocity. Here we give a synthetic description of the results, detailed velocity profiles for each configurations presented in Table 4.1 can be found in [38].

Figure 4.6 shows the velocity profiles near the front for run (b) ( $Re = 0.4$ ). Dots stand for experimental measurements whereas solid lines represent the best parabolic fit for each profile. The agreement between the theoretical parabolic profile and the experimental data was excellent far from the front as well as close to the front. This good agreement was present for all runs, even at the highest Reynolds numbers. As an example of high Reynolds flow, Figure 4.7 show the dimensionless velocity profile for run (e) ( $Re = 9.3$ ). The shape remains parabolic as close as 1.6 mm away from the contact line.

We now focus on the magnitude of the velocity. Figure 4.8 shows the ratio of the free surface



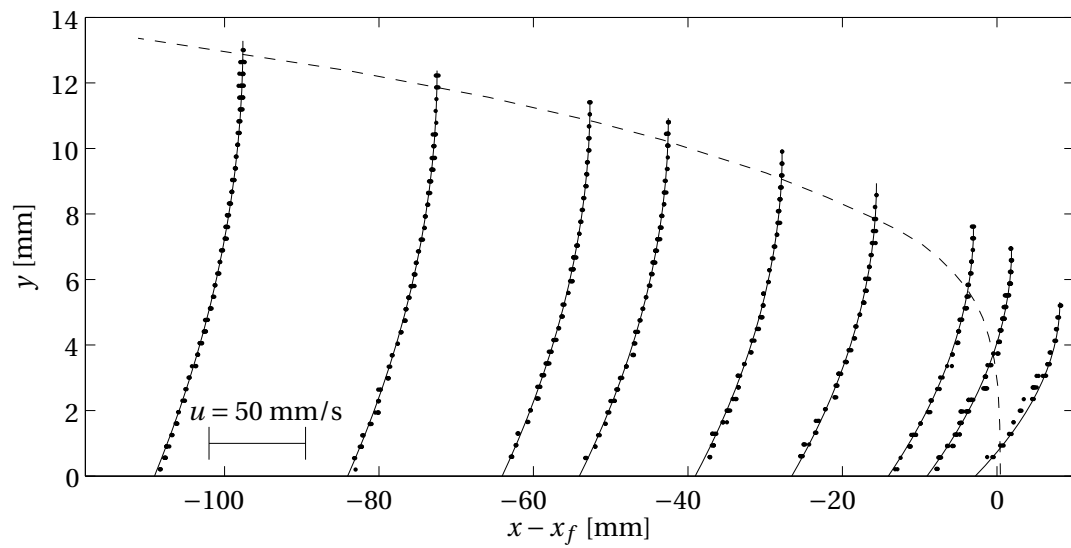


Figure 4.6: Velocity profile near the front of the flow for run (b),  $Re \sim 0.4$ . Dots represent the measured velocities while the dashed line stand for the free surface. Solid lines are fits of equation (2.12) computed for each velocity profile. Measurements were made at the centerline of the flume ( $z = 5$  cm).

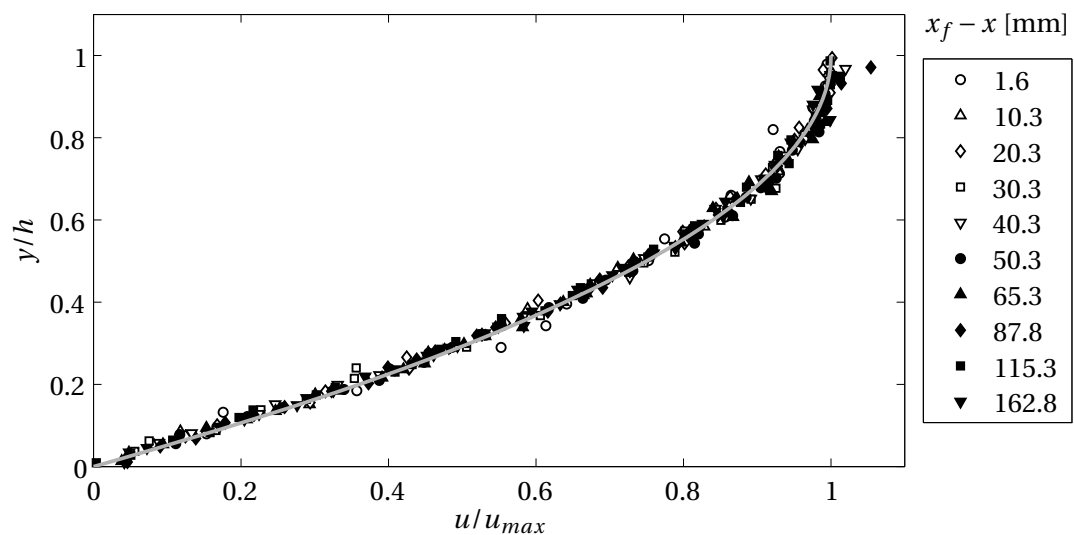


Figure 4.7: Dimensionless velocity profile for run (e),  $Re \sim 9.33$ . The solid gray line stand for the theoretical parabolic shape. Measurements were made at the centerline of the flume ( $z = 5$  cm).

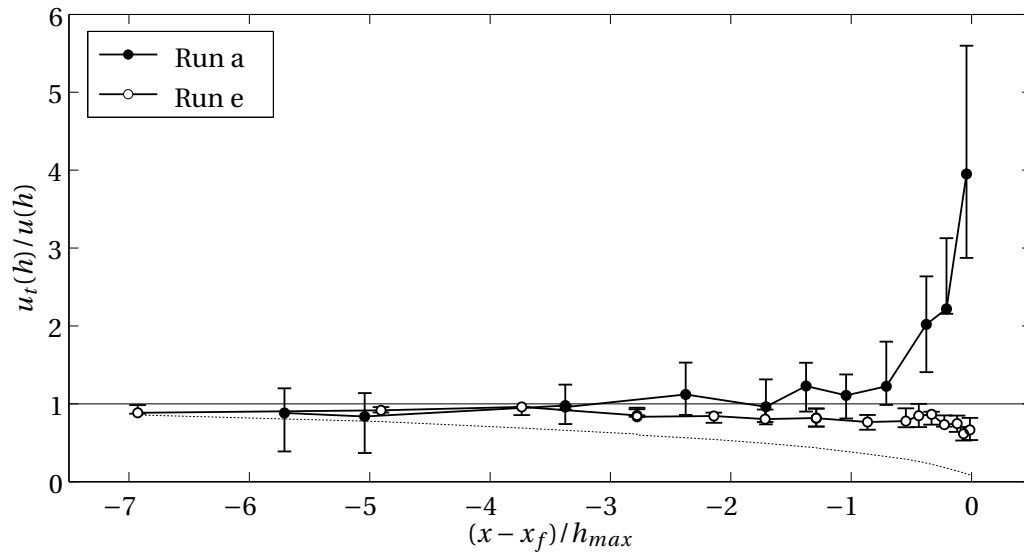


Figure 4.8: Ratio of the free surface theoretical velocity  $u_t(h)$  computed with (2.12) to the measured velocity  $u(h)$  plotted in function of the dimensionless distance to the front  $d_f = (x - x_f)/h_{max}$ ;  $h_{max}$  being the maximal flow-depth. Errorbars gives the uncertainty regarding the computation of  $\partial h/\partial x$ , whereas the horizontal line stand for the ideal case  $u_t(h) = u(h)$ . The dotted line represent the ratio  $u_t(h)/u(h)$  assuming a steady uniform regime, i.e. by setting the depth gradient term to zero in (2.12).

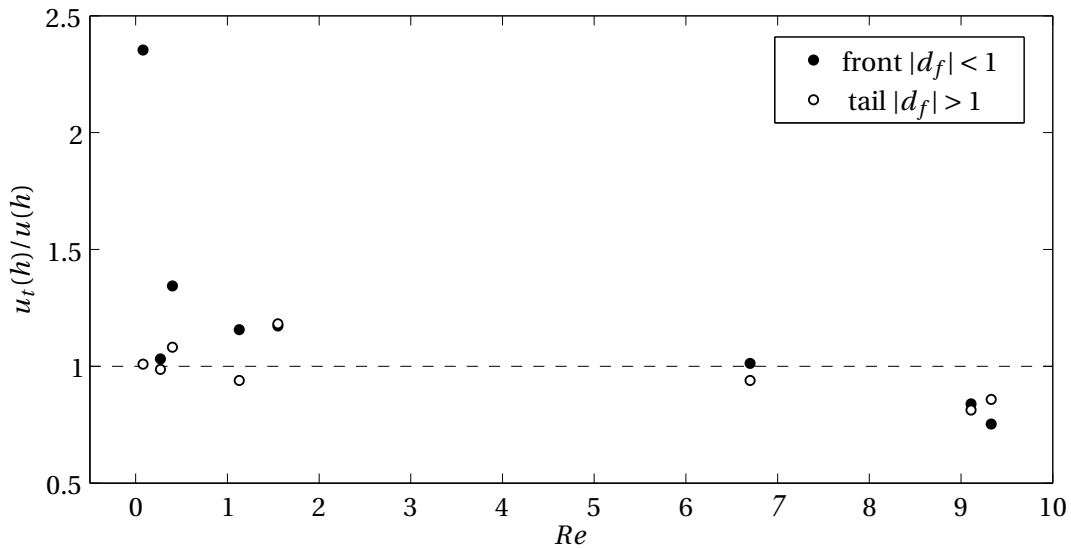


Figure 4.9: Mean of  $u_t(h)/u(h)$  depending the Reynolds number (see Table 4.1) of the run and whether measurements were taken near the tail or in the front.

velocity predicted by (2.12)  $u_t(h)$  to the experimental velocity  $u(h)$ . This ratio is plotted as a function of the dimensionless distance from the front  $d_f = (x - x_f)/h_{max}$ , with  $h_{max}$  being the maximal flow-depth. The solid horizontal line stand for the ideal case  $u_t(h) = u(h)$ . For the sake of clarity, only runs (a) and (e) are shown, as other runs lie between this two limiting curves. The error bars give the uncertainty regarding the computation of  $\partial h/\partial x$ .

As expected, far from the front (i.e when  $d_f$  was smaller than -1), a good agreement was found between lubrication theory and experimental results. However, when  $d_f$  was close to 0 (i.e. in the close vicinity of the front), the observed and theoretical profiles diverged by 400% for run (a). To illustrate the depth gradient importance in the velocity computations, we added the ratio  $u_t(h)/u(h)$  for run (e) to Figure 4.8, assuming a steady uniform regime, i.e. by setting the depth gradient term to zero in (2.12); for run (a) the solution is trivial. Figure 4.9 illustrates the mean ratio of  $u_t(h)/u(h)$  for each run and shows whether computations are made near the front ( $d_f > -1$ ) or in the tail ( $d_f < -1$ ). At small Reynolds ( $Re < 1$ ), theoretical predictions were accurate in the tail (error smaller than 8%) but they significantly overestimated the velocities near the front. For instance, differences between theory and experiment for run (a) ( $Re = 0.08$ ) were up to a mean of 130% into the front ( $d_f > -1$ ). At higher Reynolds numbers ( $Re > 6$ ), gaps between  $u_t(h)/u(h)$  calculated in the tail and in the front were small (less than 10%) meaning that the theory underestimated the global flow velocity but took the front curvature into account relatively well. The underestimation of the velocity near the front for high Reynolds number flows most probably arises from inertial and three-dimensional effects.

### 4.3 Summary

Front positions were accurately predicted by lubrication theory at small Reynolds numbers, however at higher Reynolds numbers ( $Re \sim 10$ ) differences up to 35% were found due to residual inertial and/or wall effects. Velocity profiles were found to be parabolic far from the front as well as very close to the contact line. However, as expected, near the front (distance to the contact line smaller than the typical flow height), theoretical predictions diverged from experimental results. Velocities were significantly overestimated ( $\sim 400\%$ ) by the theory at low Reynolds numbers ( $Re < 2$ ) and slightly underestimated ( $\sim 10\%$ ) at high Reynolds numbers ( $Re > 8$ ).

Very good agreement between theory and experimental velocity profiles far from the front indicate that the accuracy of the setup was very good (reliable calibration procedure and image processing methods), errors (spatial positioning and magnitude) in the calculation of velocity vectors were smaller than 5% on the whole image.



## 5 Dam break of granular suspensions

In this chapter we report results obtained by releasing concentrated granular suspensions into an inclined flume. Suspensions were composed of non-Brownian particles in a viscous fluid. Density of the interstitial fluid was modified in order for particles to be neutrally buoyant. We tested different solid concentrations ranging from 15% to 59.5% , different masses (3 to 8 kg), different flume inclinations and two size distributions of particles.

Despite the number of studies on suspensions carried out in a broad range of geometries (pipe [81, 82, 83], rectangular duct [84, 65, 36, 66], Couette device [85, 59, 86, 47], etc.), only a few authors conducted dam-break or fully-developed-flow experiments of concentrated suspensions. Nsom [30] ran dam-break experiments with neutrally buoyant particle suspensions (acrylic plastic beads immersed in glucose solutions) with solid concentrations as high as 60%. He found that for solid concentrations lower than 52%, the flow features (flow depth profile and position of the front with time) looked like those of a viscous flow, but for higher concentrations (typically 60%), he observed that the flow came to a halt, a phenomenon typical of plastic behavior. Timberlake and Morris [35] measured the velocity and concentration profiles in thin films of concentrated suspension down an inclined plane for various inclinations and concentrations. The data were compared with predictions from a particle-migration model. They observed that the free surface became more deformed with both increasing concentration and inclination. Bonnoit et al. [31] used neutrally buoyant 40  $\mu\text{m}$ -polystyrene bead suspensions in silicone oil in the 35 to 61% solid concentration range. By using the steady-state equation that relates the bulk viscosity to the surface velocity and flow depth, they were able to measure the viscosity for various flow depths and plane inclinations. They found that the bulk viscosity varied consistently with the Zarraga relation. Ward et al. [29] carried out experiments with solid concentrations ranging from 0.35 to 0.55. Various input parameters (particle density and size, fluid viscosity, initial volume, plane inclination) were varied. They showed that even though departures from the  $x_f \sim t^{1/3}$  theoretical trend were observed, this scaling was a correct approximation at long times. Zhou et al. [87] observed that for moderately concentrated suspensions and gentle slopes, the suspension remained well mixed and flowed like a viscous fluid, but for highly concentrated suspensions and steep

slopes, particles moved faster than the interstitial fluid and accumulated in a ridge just behind the contact line. Husband et al. [88] conducted experiments in a flume with neutrally buoyant suspensions to determine if the solid concentration gradient which arose between the bottom of the flume and the free surface was accompanied by size segregation. Suspensions composed of PMMA particles with a bimodal size distribution and solid fractions of 60% and 65% were used. They observed that at the end of the channel, the surface of the suspension was composed almost exclusively of large particles and inferred that coarse fraction of particles migrated much faster than the fine fraction.

In contrast with earlier investigations, we benefited from the visualization techniques that we specifically developed to measure velocity profiles within the flowing material (i.e. far from the sidewall). The time resolution of our system allowed us to have a reliable velocity map even very close to the front.

This chapter is organized as follow: first we describe the facility and procedures but briefly since they are extensively presented in Chapter 3, then we present and discuss the experimental results.

### 5.1 Facility and procedures

All experiments were run with highly concentrated suspensions of polymethylmethacrylate (PMMA) particles within a mixture of three fluids called trimix, which was prepared so that the suspension was isodense and isoindex (transparent). We used the PIV measurement technique and prepared the suspensions as described in Chapter 3.

Before each dam-break experiment, the suspension was left for 12 hours in a sealed cylindrical container and gently stirred in order to remove bubbles entrapped in the bulk. As minute changes in the suspension preparation lead to substantial changes in the bulk behavior, great care was taken to keep the experimental conditions as constant as possible. Every five dam-break experiments, a new suspension was prepared in order to keep the solid concentration drift small and also to limit potential corrosive effects of fluids on particles. Reproducibility tests were carried out to validate this procedure.

We define a two-dimensional Cartesian coordinate system in which the  $x$ -axis points down the flume, the  $y$ -axis is in the direction of the upward pointing normal, and the  $z$ -axis is in the cross-stream direction. The upper end of the flume is at  $x = 0$ , while the lower end is at  $x = 350$  cm. The bulk velocity  $\mathbf{u}$  has components  $u$ ,  $v$ , and  $w$  in each of the directions  $x$ ,  $y$  and  $z$  respectively.

### 5.2 Results

Table 5.1 summarizes the different runs conducted during this study. We divide the description of the results in three subchapters, corresponding to typical behaviors observed during our experiments: i) runs with a solid fraction smaller than 45% ii) runs with a solid fraction between

Table 5.1: Features of the different runs: interstitial fluid, solid fraction (in volume), initial mass, flume inclination, size distribution of the beads, density and viscosity of the interstitial fluid, density of the beads.

Run	fluid	$\phi$ %	$m$ (g)	$\theta$ (deg)	sieved	$\rho_f$ (kg/m <sup>3</sup> )	$\mu_f$ (Pa s)	$\rho_s$ (kg/m <sup>3</sup> )
(a)	trimix	15	3000	25	yes	1184	0.124	1184
(b)	trimix	30	3000	25	yes	1184	0.124	1184
(c)	trimix	45	3000	25	yes	1184	0.124	1184
(c2)	trimix	45	3000	25	yes	1184	0.124	1184
(d)	trimix	52	3000	5	yes	1184	0.124	1184
(e)	trimix	52	3000	15	yes	1184	0.124	1184
(f)	trimix	52	3000	25	yes	1184	0.124	1184
(g)	trimix	55	3000	25	yes	1184	0.124	1184
(h)	trimix	56	3000	25	yes	1184	0.124	1184
(i)	trimix	57	3000	25	yes	1184	0.124	1184
(j)	trimix	58	3000	25	yes	1184	0.124	1184
(k)	trimix	52	6000	25	yes	1184	0.124	1184
(l)	trimix	57	6000	25	yes	1184	0.124	1184
(m)	trimix	57.5	6000	25	yes	1184	0.124	1184
(n)	trimix	58	6000	25	yes	1184	0.124	1184
(o)	trimix	58.5	6000	25	yes	1184	0.124	1184
(p)	trimix	59.5	6000	25	yes	1184	0.124	1184
(q)	trimix	59.5	2000	25	no	1184	0.124	1184
(r)	trimix	59.5	3000	25	no	1184	0.124	1184
(s)	trimix	59.5	4000	25	no	1184	0.124	1184
(t)	trimix	59.5	6000	25	no	1184	0.124	1184
(u)	trimix	59.5	7940	25	no	1184	0.124	1184
(v)	UCON-Triton	52	3000	15	yes	1068	0.446	1184

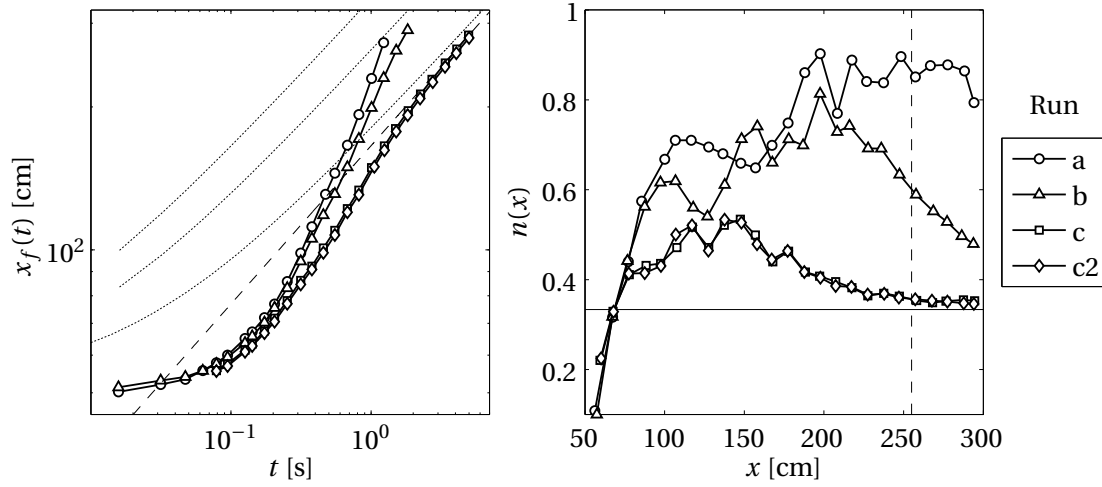


Figure 5.1: Left: front positions  $x_f(t)$  for run (a, b, c, c2) in log-log scale. The dashed line represents the asymptotic lubrication solution (2.16) for run (c) whereas dotted lines stand for the numerical solutions of (2.14) computed for each run; a Krieger-Dougherty viscosity (2.17) with  $n = 2$  and  $\phi_m = 0.625$  was used. Right: the  $n(x)$  exponent computed giving a local fit of the function  $f(t) = At^n$  on the front positions  $x_f(t)$ . Asymptotic  $n$  predicted by the theory for Newtonian fluids,  $n = 1/3$  is also shown (solid horizontal line). Location of the window used for the velocity profiles measurements is indicated by a vertical dashed line ( $x_0 = 255$  cm).

45 and 55 % and finally iii) runs with a solid fraction higher than 55%. Of course there are no rigid limits and divisions were arbitrarily decided in order to facilitate description of the observations. To be more rigorous, a description in terms of solid fraction, shear rate, viscosity of the interstitial fluid, fluid and particle density should be used whether than a description only in term of solid fraction [67]. We begin each section by discussing the bulk behavior of the flows (front position, flow height) and follow with the presentation of more local properties like velocity profiles.

### 5.2.1 Runs with low solid fractions ( $\phi \leq 0.45$ )

#### Front positions

Figure 5.1 show the front position  $x_f(t)$  for runs (a, b, c) and (c2). Run (c2) was conducted with the same parameters as run (c) (i.e. slope 25 deg, mass 3 kg, solid fraction 45%) to verify the reproducibility of the results. Differences between the front positions of run (c) and run (c2) were smaller than 4 cm / 1.5% everywhere, indicating the reliability of the experimental procedure.

Since the solid concentration was rather small, we expected a viscous behavior and thus a front position evolution given by  $x_f \sim t^{1/3}$ , once inertial and pressure gradient effects dissipated. To have a better idea of how well the behavior of the suspension approached the theoretical



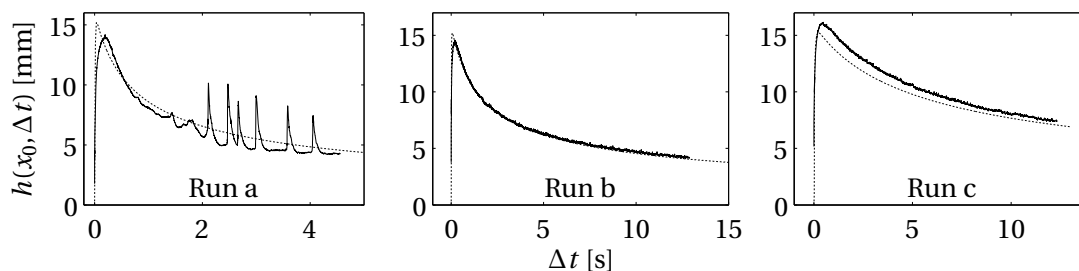


Figure 5.2: Flow depth variation measured at  $x_0 = 255$  cm (solid line) and numerical solution of equation (2.14) using a Krieger-Dougherty viscosity (2.17) computed with  $\beta = 2$  and  $\phi_m = 0.625$ . Because of the delay in the experimental front position relative to the computed front position, the time axis of the theoretical curve  $h(x_0, t)$  has been shifted so that the curves have the same start point to facilitate comparison.

asymptotic behavior, we also computed a local fit<sup>1</sup> of the function  $f(t) = At^n$  on front positions (right plot of Figure 5.1). Runs (a) and (b) did not reach an asymptotic behavior before the end of the channel due to the small solid concentrations and consequently their small effective viscosity. However, the values for  $n$  seemed to converge at long time near  $n = 0.33$ , especially in run (b). On the contrary, convergence to the theoretical asymptotic solution was very fast for run (c) (solid fraction 45%),  $n$  being 0.35 at the outlet of the flume with a downward trend.

Thus, as expected, at low solid fractions ( $\phi < 0.45$ ), suspensions behaved like a viscous fluid in terms of the front position evolution. To test further this observation we computed an effective viscosity for each run (a, b, c) using the Krieger-Dougherty equation (2.17) with  $\beta = 2$  and  $\phi_m = 0.625$ . Figure 5.1 shows (dotted line) the numerical solutions of equation (2.14) for each run and the asymptotic solution (2.16) for run (c). Agreement between theory and experimental data was very good for run (c) with discrepancies smaller than 5% at the end of the channel. For runs (a) and (b), agreement is not complete, due to the residual inertial effects not taken into account by the theory.

Predictions by the lubrication theory for a viscous fluid were also tested for the shape of the free surface. Figure 5.2 shows the time evolution of the flow depth measured at  $x_0 = 255$  cm together with the numerical solutions of equation (2.14) (time shifted). The shape of the free surface was always well predicted by the theory far from the front except for run (a), for which free-surface instabilities occurred due to the high speed of the flow. Near the front, deviations between theory and experimental data increased but remained smaller than 10%. These discrepancies were most probably due to the simplifying hypothesis (small aspect ratio) used to obtain equation (2.14).

<sup>1</sup>The value of  $n$  at the downstream position  $x$  was computed by making a fit on the  $x_f(t)$  data with  $|x_f(t) - x| < 5$  cm.

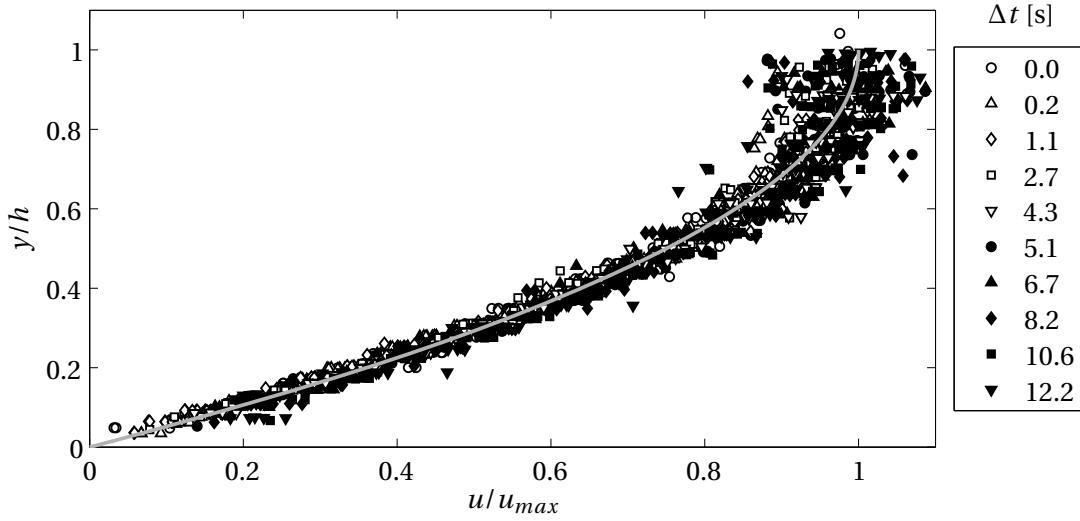


Figure 5.3: Normalized velocity profiles for run (c) (solid fraction 45%) taken at different times  $\Delta t$  behind the front;  $\Delta t = 0$  corresponds to the contact line. Measurements were taken at the center of the channel ( $z = 5$  cm) at the downstream coordinate  $x_0 = 255$  cm. The solid gray line stands for the Newtonian parabolic velocity profile.

### Velocity profiles

Figure 5.3, shows the normalized velocity profiles for run (c) taken at different times. The measurements were made at the center of the channel ( $z = 5$  cm) at the downstream coordinate  $x_0 = 255$  cm. The increase in noise between Figure 4.7 and Figure 5.3 was due to imperfect refraction index matching between fluid and particles in the suspension and/or inhomogeneities amongst the particles. Despite the relatively high concentration (45%), it was not possible to identify a significant deviation from a Newtonian profile  $u(y) \sim y(2h - y)$  for runs (b) and (c). This leads to the conclusion that no significant migration or sedimentation in the  $y$  direction took place during the experiment. We were not able to compute the velocity profile inside the flow of run (a) due to its higher velocity ( $u_f > 3$  m/s).

Since flows were homogeneous and velocity profiles were viscous ( $u(y) \sim y(2h - y)$ ), we were interested in testing the validity of the effective viscosity model (like (2.17) or (2.18)) against the experimental viscosity computed using the lubrication equation (2.12) fitted on experimental data. Figure 5.4 shows the ratio of the theoretical viscosity  $\mu_t$ , computed using the mean solid fraction and (2.17) or (2.18), to the experimental viscosity  $\mu$  computed with (2.12). The  $\partial_x h$  term in (2.12) was determined from the undistorted PIV images. The two runs exhibited the same features: a high ratio  $\mu_t/\mu$  near the front followed by a constant plateau. The constant ratio far from the front indicates that the internal dynamics were accurately described by equation (2.12). The increase in the viscosity ratio near the front was due to a decrease in experimental viscosity since the theoretical viscosity was constant for a given run and given by equation (2.17) or (2.18). The apparent decrease in viscosity near the front most likely

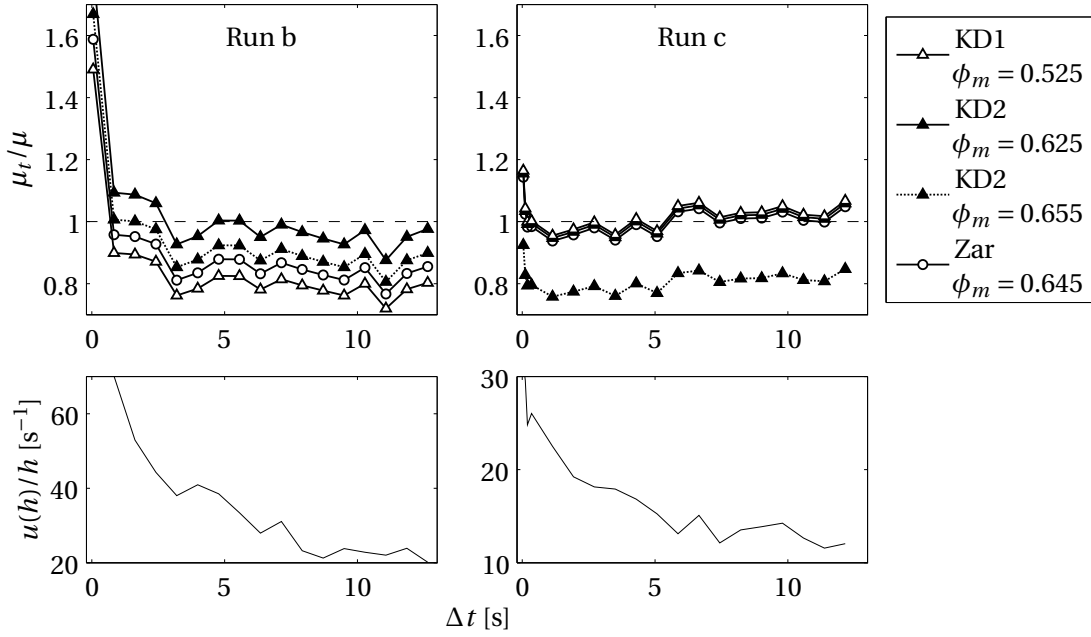


Figure 5.4: Ratio of theoretical viscosity  $\mu_t$  to experimental viscosity  $\mu$  measured at the downstream coordinate  $x_0 = 255$  cm at different times behind the front;  $\Delta t = 0$  corresponds to the contact line. Theoretical viscosities were computed using the mean solid fraction and Krieger-Dougherty/Zarraga models and were thus constant for a given run. Experimental viscosities were computed using the lubrication velocity profile (2.12) fitted on the experimental profiles. "KD1" stand for the Krieger-Dougherty model (2.17) with  $\beta = -2.5\phi_m$ . "KD2" stand for the Krieger-Dougherty model but with  $\beta = 2$ , "Zar" stand for the Zarraga model (2.18). We adapted  $\phi_m$  in order to have  $\mu_t/\mu = 1$  for the most concentrated run (run c). Dotted line, was computed using a Krieger-Dougherty relation with  $\beta = 2$  and  $\phi_m$  set to the experimental maximum packing fraction value  $\phi_{RCP} = 0.655$  obtained by vibrating the beads. Bottom: typical shear rates  $u(h)/h$ .

originates from the small aspect ratio hypothesis used in equation (2.12) and not from a true decrease in solid fraction. As observed for the Newtonian flows in Chapter 4 (see Figures 4.8 and 4.9), equation (2.12) tends to underestimate the velocity near the front at high Reynolds numbers.

Different viscosity models were tested. The value of  $\phi_m$  was adapted in order to have a ratio of one between theoretical and experimental viscosity for the run with the highest solid concentration (run c). For the dashed line we did not adapted  $\phi_m$  but we used instead the random close packing fraction  $\phi_{RCP} = 0.655$  obtained by vibrating and weighting the beads (see 3.2).

The Krieger-Dougherty model (2.17), with  $\beta = 2$  and  $\phi_m = 0.625$  showed the best general agreement. This result was consistent with the value  $\phi_m = 0.605$  obtained by Ovarlez [47] for suspensions composed of monodisperse particles. Using the same equation but setting  $\phi_m$  to the random close packing fraction, gave a theoretical viscosity 15 to 25% smaller than the

experimental viscosities. The viscosity of run (b) was underestimated by 30% when using  $\beta = 2.5\phi_m$ , meaning that this model devised to recover the Einstein limit at low solid fraction, was not suitable to compute the viscosity of suspensions with solid fractions as high as 45%. Setting  $\phi_m = 0.645$  in the Zarraga equation (2.18), calibrated for a good agreement between theory and experiment in run (c), produced discrepancies as high as 20% in run (b).

Of interest is the gap between the best fitted  $\phi_m = 0.625$  and the dry random close packing fraction  $\phi_{RCP} = 0.655$ . Shapiro and Probst [89] measured for different size distributions the  $\phi_m$  values extrapolated from viscosity measurements in a Couette cell and the corresponding  $\phi_{RCP}$  obtained by vibrating the beads into graduated cylinders. They found that a constant scaling factor was needed to link the two values and argued that this discrepancy was due to the degree of ordering present in the suspension. They suggested that rather than the random close packing, the random loose packing (the least dense packing that can support an external load) had to be identified with the fluidity limit (i.e. the  $\phi_m$  extrapolated from effective viscosity measurements).

### 5.2.2 Runs with intermediate solid fractions ( $0.45 < \phi \leq 0.55$ )

#### Front positions and velocity profiles

Figure 5.5 shows in a log-log representation the front positions  $x_f(t)$  of the runs with a solid fraction between 45% and 55%. All runs seemed to follow a  $t^n$  trend at long time. To have a clearer view of how an asymptotic behavior was approached we locally fitted a function  $f(t) = At^n$  to the front positions, as was already done for the lower concentrated suspensions. The resulting  $n$  values are shown in Figure 5.6. After a transition length, all runs converged to the asymptotic value expected for viscous fluids, except run (k) which converged more slowly. Thus, despite the high solid concentration, the front position of the bulk could still be accurately described using viscous theory. The flow depth is also well described by viscous theory (Figure 5.7) if the viscosity of the bulk is tuned to take into account the shear thinning that takes place for the slowest flows.

However, unlike less concentrated flows, runs involving solid fractions greater or equal to 52% exhibited inhomogeneities. Figure 5.8 shows the time evolution of the velocity profile taken at the centerline of the channel for run (f) (solid fraction 52%, slope 25 deg, mass 3 kg). Near the front ( $\Delta t < 1.5$  s), a Newtonian shape  $u(y) \sim y(2h - y)$  fitted experimental data well, with deviation being smaller than 2%. At longer times, the velocity profile became more and more blunted, as expected from migration theory: particles left the bottom and migrated to the free surface where the shear rate was almost zero. Therefore the effective viscosity dropped in the lower layer of the flow and increased near the free surface, leading to a blunted profile. The time evolution of the relative deviation  $\Delta u/\bar{u}(t)$  from a Newtonian velocity profile is shown on the upper subplot of Figure 5.8.  $\Delta u/\bar{u}(t)$  is the area between the experimental blunted

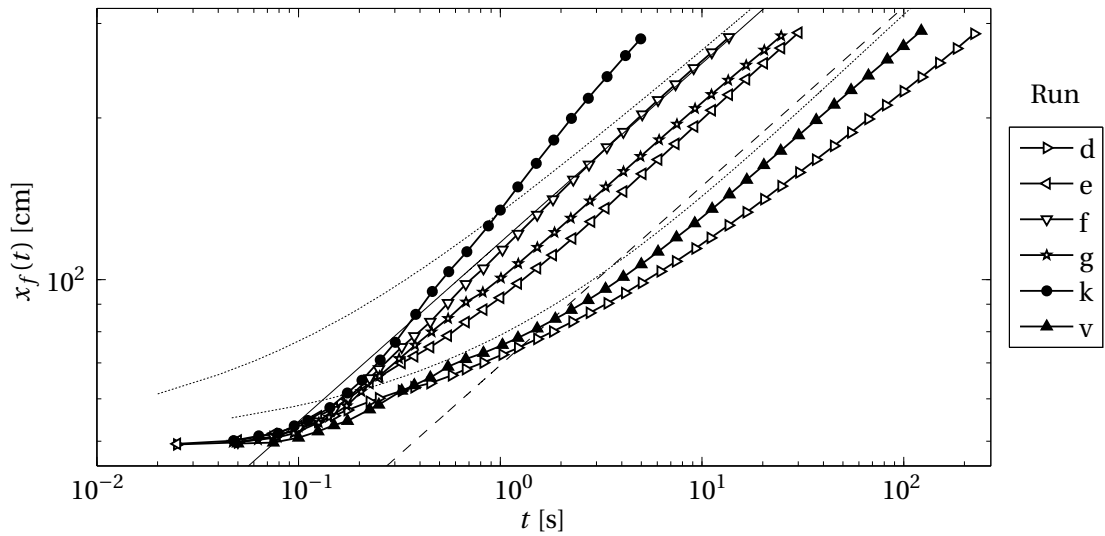


Figure 5.5: Front positions  $x_f(t)$  for runs with an intermediate solid fraction (0.52-0.55). Viscous asymptotic solutions for run (d) (dashed line) and (f) (solid line) were computed using a Krieger-Dougherty viscosity ( $\beta = 2$ ,  $\phi_m = 0.625$ ). Dotted lines stand for the solutions of equation (2.14) for each of the two cases.

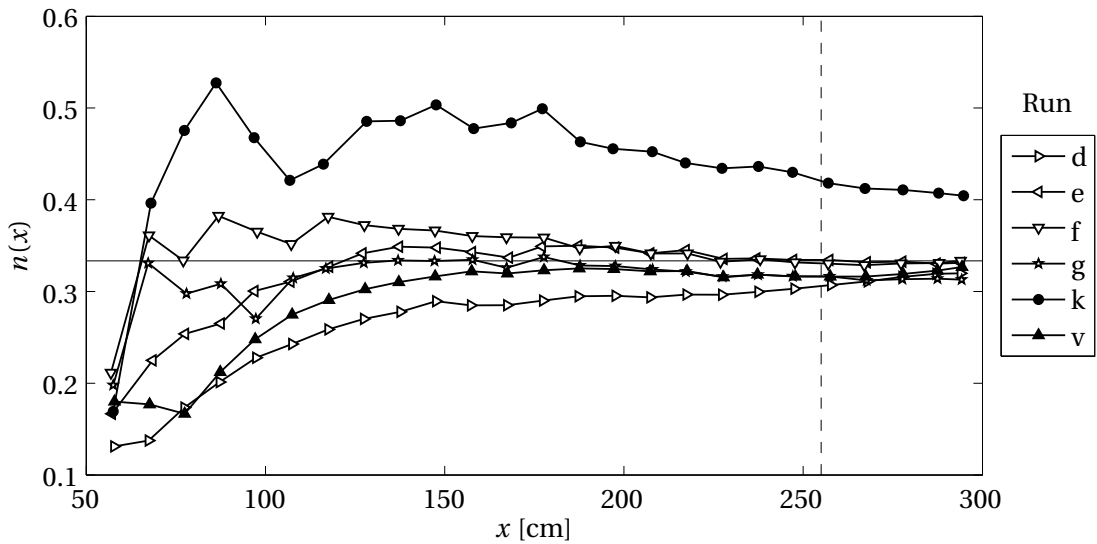


Figure 5.6: Local fit of the function  $f(t) = At^n$  to data presented in Figure 5.5. Asymptotic  $n$  predicted by the theory,  $n = 1/3$  is also shown (solid horizontal line). The vertical dashed line indicates the position of the measurement window used for the velocity profiles measurements ( $x_0 = 255$  cm).

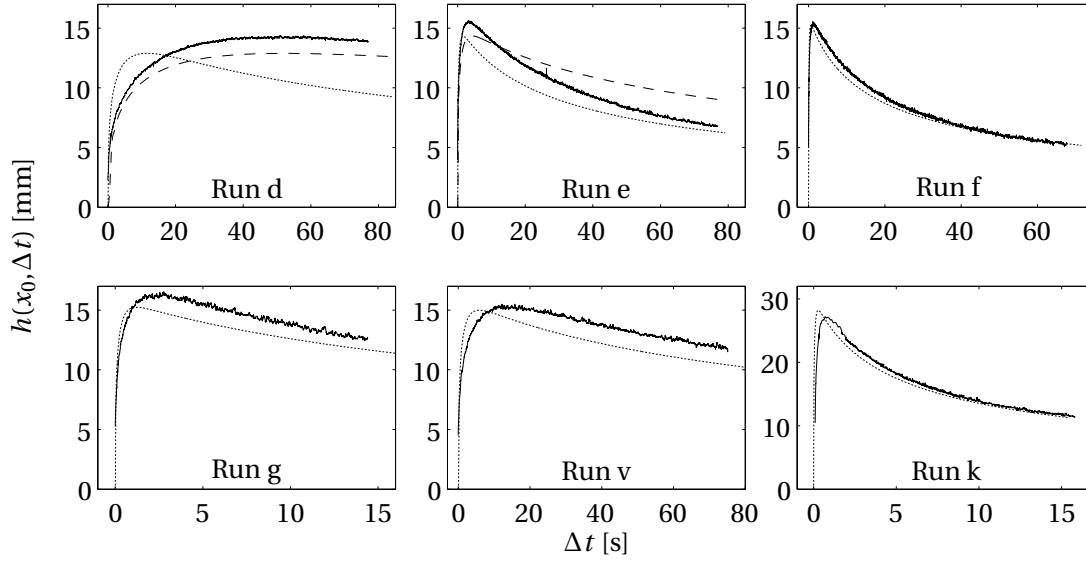


Figure 5.7: Flow depth variation measured at  $x_0 = 255$  cm (solid line) and numerical solution of equation (2.14) using a Krieger-Dougherty viscosity (2.17) computed with  $\beta = 2$  and  $\phi_m = 0.625$ . Because of the delay in the experimental front position relative to the computed front position, the time axis of the theoretical curve  $h(x_0, t)$  has been shifted so that the curves have the same starting point for ease of comparison. For runs (d) and (e) we also plotted solutions (dashed lines) of equation (2.14) with an increased viscosity in order to take into account shear thinning (see subsection "Steady-state migration models" of the present chapter). The viscosity was increased by a factor 4.6 for run (d) and 2.6 for run (e).

velocity profile and the viscous shape, normalized by the mean velocity<sup>2</sup>. The flow depth was also reported on the upper subplot of Figure 5.8 to illustrate the time scale of the surge. The same blunting of the velocity profile was observed for all runs of this section and due to these similarities, we only show detailed results for run (d) ( $\phi = 52\%$ ,  $\theta = 5$  deg,  $m = 3$  kg) and for run (g) ( $\phi = 55\%$ ,  $\theta = 25$  deg,  $m = 3$  kg) respectively in Figure 5.9 and Figure 5.10.

Figure 5.11 summarizes the time evolution of the deviation  $\Delta u / \bar{u}$  for all runs. For the sake of comparison, we also reported results of run (b) and (c) containing a low solid fraction ( $\phi < 0.45$ ). As expected, for these two runs  $\Delta u / \bar{u}$  remained smaller than 5%, confirming that no migration occurred during the experiment. For runs with  $\phi = 52\%$  (d,e,f and v),  $\Delta u / \bar{u}$  values were almost stabilized at the end of the acquisition time ( $t \sim 75$  s). Steady values of

<sup>2</sup>The following definition was used:

$$\Delta u / \bar{u} = \frac{\sum_i^n (u_i - U_i)}{\sum_i^n u_i}$$

with  $u_i$  the  $i^{\text{th}}$  point on the experimental velocity profile taken at time  $t$ .  $U_i$  was the corresponding Newtonian velocity evaluated at the same flow depth  $y$ .  $U_i$  was computed by fitting a function  $U(y) = By(2h - y)$  on the experimental data so that  $u_i = U_i$  at the free surface. This definition allows us to characterize the shape of the experimental velocity without taking into account the magnitude.

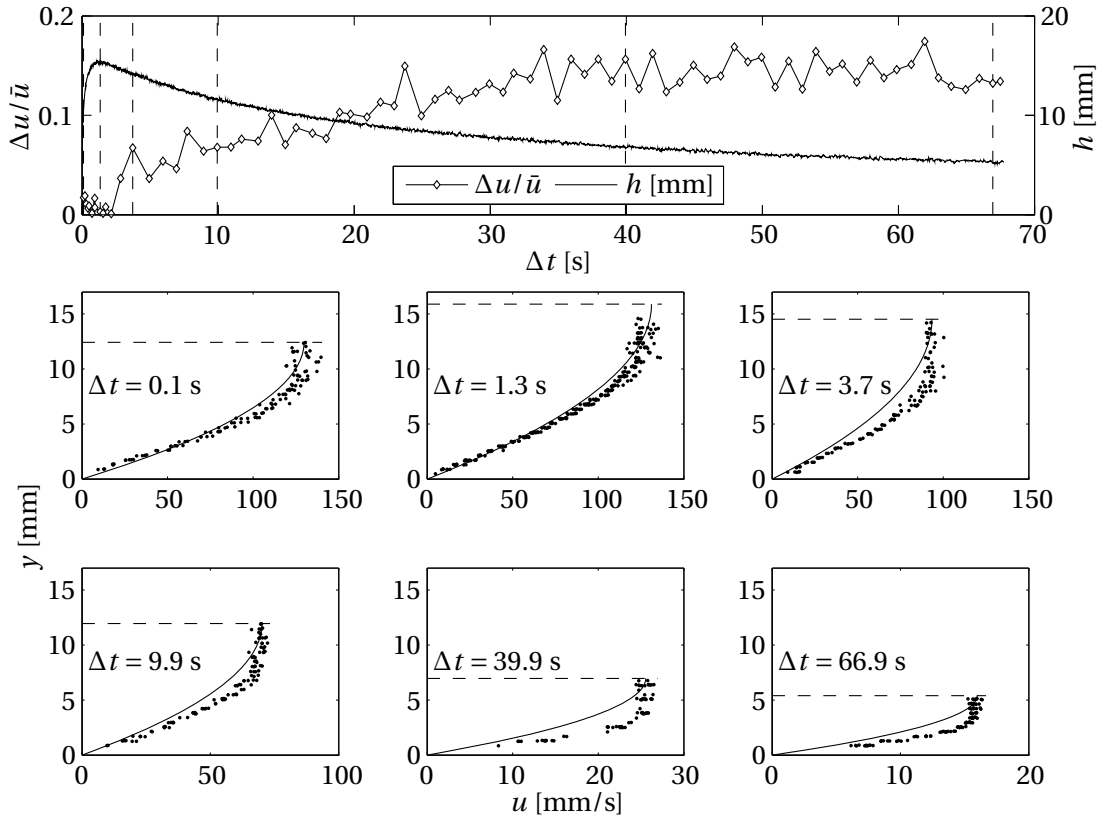


Figure 5.8: Velocity profiles and flow depth evolution for run (f): solid fraction 52%, slope 25 deg, mass 3 kg. Data were taken at the downstream coordinate  $x_0 = 255$  cm at the center of the channel ( $z = 5$  cm);  $\Delta t = 0$  corresponds to when the front crossed this position.

Upper subplot: time evolution of the normalized deviation from a Newtonian shape  $\Delta u/\bar{u}$  (white diamond symbols). The corresponding flow depth is also shown (solid line). Bottom subplots: velocity profiles taken at six different times  $\Delta t$  behind the front. The solid lines stand for the Newtonian shapes  $u(y) \sim y(2h - y)$  and the dashed lines delineate the free surface positions. On the upper subplot, the times at which the six selected velocity profiles were taken are indicated by vertical dashed lines.

$\Delta u/\bar{u}$  were nearly the same for the four runs (differences  $\sim 5\%$ ). This result was expected for runs (d) to (f) since theory predicts that the final concentration profile at steady state is not a function of the slope. More surprising is the fact that the shape of the final velocity profile for run (v) (density mismatch between fluid and particles of 10%) was the same as for runs (d) to (f) (neutrally buoyant particles). Since gravity was acting against migration we would have expected a less blunted steady velocity profile. As no significant differences were observed, we infer that settling due to a density mismatch of 10% was negligible against migration processes.

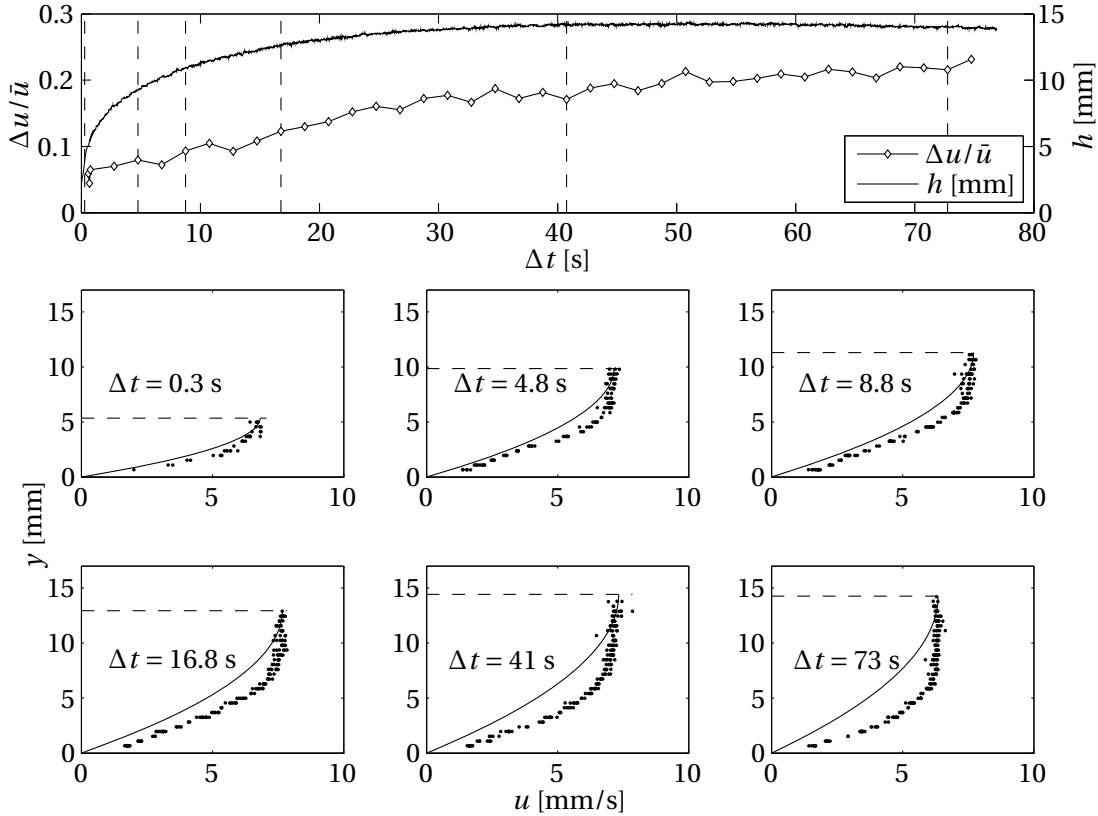


Figure 5.9: Same caption as Figure 5.8 but for run (d): solid fraction 52%, slope 5 deg, mass 3 kg.

### Steady-state migration models

We are now interested in testing migration models against steady state velocity profiles measured experimentally. The idea was not to test all available models but only to check if a migration theory coupled to an effective viscosity was able to capture the shape and the magnitude of the observed velocity. As explained in Chapter 2, we chose the Mills and Snabre [64] theory because no adjustable parameters (other than  $\phi_m$ ) were required. In addition, this theory gave the same concentration profiles as the diffusive model of Phillips et al. [58]. As effective viscosity we used a Krieger-Dougherty model (2.17) with  $\beta = 2$  and  $\phi_m = 0.625$  since it provided the best agreement on less concentrated flows (Figure 5.4). Velocity profiles were computed, numerically integrating equation (2.26) with a fourth-order Runge-Kutta algorithm.

The results are shown in Figure 5.12. Concentration profiles, normalized velocity profiles and velocity profiles in physical units are plotted. As expected, the non-local model (dashed line) allowed removal of the non physical sharp cusp near the free surface on the concentration profiles. This modification produced a vertical shift of the mean solid fraction in the upward direction, lowering the solid fraction near the bottom. This shift led to more blunted velocity profiles and therefore predicted faster flows than the local model (solid line) or the Newtonian



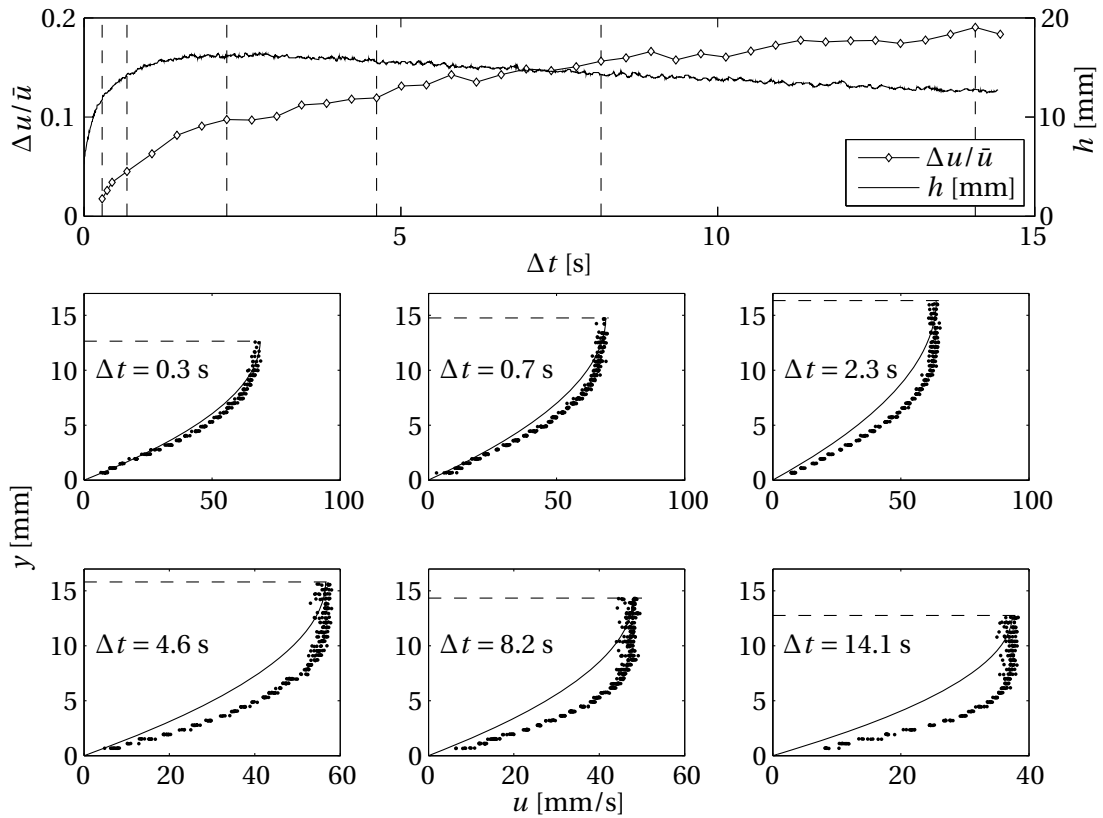


Figure 5.10: Same caption as Figure 5.8 but for run (g): solid fraction 55%, slope 25 deg, mass 3 kg.

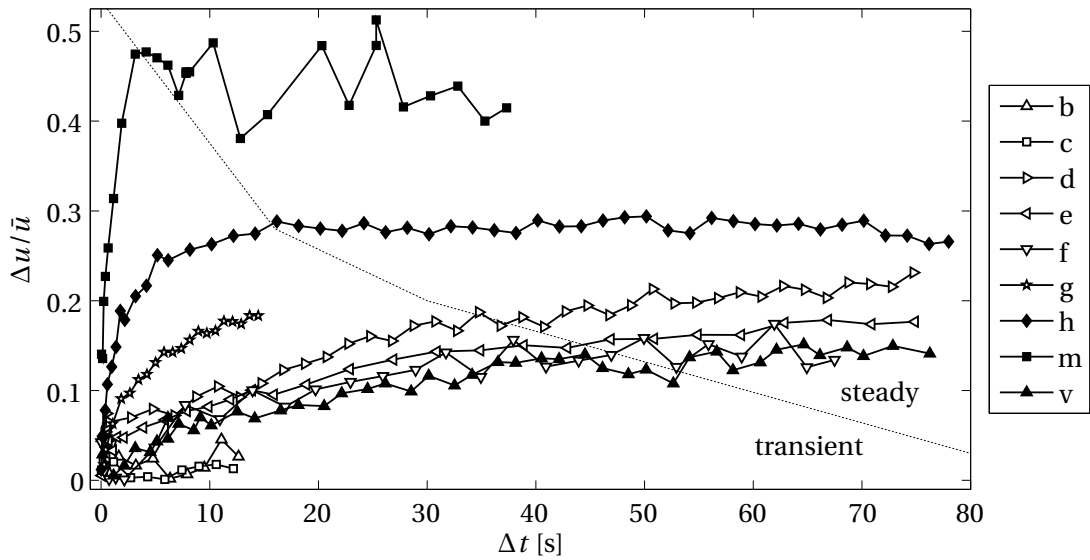


Figure 5.11: Time evolution of the deviation  $\Delta u/\bar{u}$ ,  $\Delta t = 0$  corresponding to the tip of the flow (contact line). For the sake of comparison we also plotted results obtained at lower (run(b) and run(c)) and higher (run(h) and run(m)) concentrations.

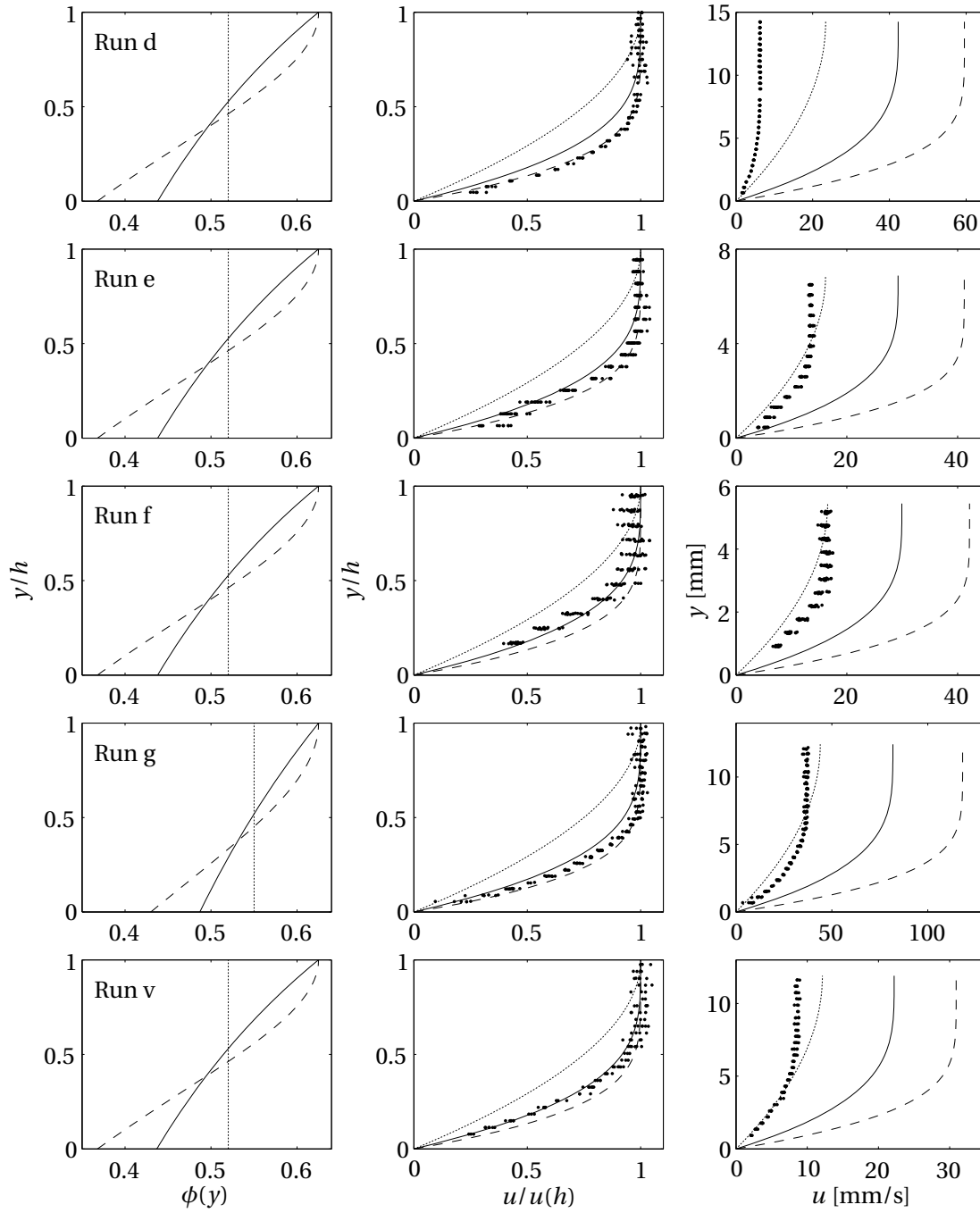


Figure 5.12: Comparison between migration models and experimental velocity profiles at steady-state. Measurements were taken at the downstream coordinate  $x_0 = 255$  cm at time  $\Delta t = 70$  s except for run (g) for which  $\Delta t = 14$  s. Left plots show the theoretical concentration profile, middle plots show the normalized results and right plots are for the results in physical coordinates. Solid lines represent the local Mills and Snabre model whereas the dashed lines represent the non-local model assuming a correlation length of the same order as the flow depth. Dotted lines assume no migration and thus stand for the Newtonian velocity profile. A Krieger-Dougherty viscosity (2.17) ( $\beta = 2$  and  $\phi_m = 0.625$ ) was used as a viscosity function.

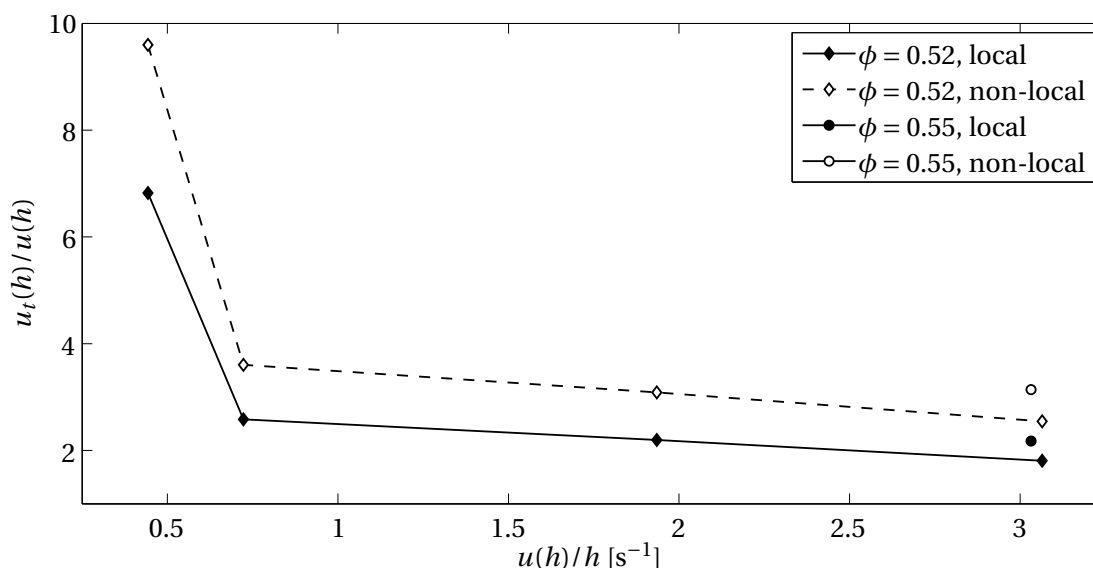


Figure 5.13: The ratio between free surface velocity  $u_t(h)$  predicted by migration models and experimental free surface velocity  $u(h)$  (see Figure 5.12). Results are plotted in function of  $u(h)/h$ .

theory (dotted line).

Agreement between theory and the experiment was very good regarding the shape of the curves. The local theory seemed to match experimental results slightly better than the non-local theory for runs (f) and (v) and, conversely, run(d), (g) and (e) showed better agreement with the non-local theory. However, regarding the magnitude of the velocity, discrepancies between theory and experiments were as high as 800%. These disagreements most probably arose due to a dependence of the effective viscosity on the shear rate ( $\mu = \mu(\dot{\gamma}, \phi)$ ). Indeed, parameters used in the Krieger-Dougherty expression were fitted at  $\bar{\gamma} \sim 15 - 20 \text{ s}^{-1}$  and, for instance, accurately predicted the front position evolution of run (f) (see Figure 5.5) during the first 10 seconds of the flows, when  $\bar{\gamma} \sim 10 \text{ s}^{-1}$ . However, the same viscosity function failed to give an estimation of the flow velocity for the same run after  $\sim 70 \text{ s}$  when  $\bar{\gamma} \sim 3 \text{ s}^{-1}$  and it failed to predict the front position evolution of run (d) (see Figure 5.5) with  $\bar{\gamma} \sim 1 \text{ s}^{-1}$ . To formalize these observations, we plotted in Figure 5.13 the discrepancies observed in Figure 5.12 as functions of the mean shear rate. As expected, overestimation of the theoretical velocity increased as the mean shear rate decreased. This behavior was consistent with previous observations that reported shear thinning at low shear rates for polydisperse concentrated suspensions. In the case of our sieved particles, the normalized standard deviation was  $\sigma/(2\bar{a}) \sim 0.3$ . For such values of polydispersity, Reardon [50] reported, using a falling-ball rheometer and suspensions with solid fraction of 0.5, a viscosity varying with the shear rate  $\mu_{\text{eff}} = m\dot{\gamma}^{q-1}$ , with  $q \sim 0.6$ . Since our expression of viscosity was fitted to shear rates around  $15 - 20 \text{ s}^{-1}$ , following Reardon, our effective viscosity should increase by a factor  $\mu(\dot{\gamma} = 0.4) = (0.4/20)^{0.6-1} \mu(\dot{\gamma} = 20) = 4.8$  when the shear rate is reduced to 0.4. This result is in good agreement with the values plotted in Figure 5.13 ( $u_t(h)/u(h) \sim 7$  for  $u_h/h = 0.4$ ) if we assume

that the free surface velocity is proportional to the mean viscosity of the bulk. We also tested the effects of increased values of viscosity computed with Reardon's viscosity  $\mu_{\text{eff}} \sim \dot{\gamma}^{0.6-1}$  on the flow depth profiles of Figure 5.7. Theoretical flow depth profiles with increased viscosity were computed for runs (d) and (e). For run (d), agreement with experimental data was much better using the new viscosity. However, agreement was only partial for the data of run (e), probably because of the strong variations in the values of the shear rates between the front and the tail.

### Time scale for migration

In this subsection we discuss the time taken until a constant  $\Delta u/\bar{u}$  is observed in Figure 5.11. The typical time scale for migration was not studied extensively and few data dealing with transient concentration profiles are available, all obtained in Couette cells [90, 86, 58]. Usually a Leighton [57] diffusion theory is applied and the typical migration time is controlled by a diffusion coefficient  $D = d(\phi)\dot{\gamma}a^2$ , with  $a$  the radius of a particle,  $\dot{\gamma}$  the shear rate and  $d(\phi) \sim \phi^2$  until  $\phi \sim 0.55$ , the dimensionless self-diffusion coefficient.

In our case computing a time scale was difficult due to the strong variations in flow depth and velocity during the migration process. However, we tried to give an estimation of  $d(\phi)$  as follows. We supposed that the concentration at the front of the flow was constant across the flow depth i.e. there was no migration. This hypothesis is consistent with the data presented in Figure 5.11 since  $\Delta u/\bar{u} = 0$  when  $\Delta t$  is small. We also suppose that the flow is locally uniform. Following Nott and Brady [60], and the shear induced diffusion hypothesis of Leighton and Acrivos [57], the average distance  $l_y$  traveled by a particle perpendicularly to the direction of the flow, during a time  $t_*$  is given by

$$l_y = 2(Dt_*)^{1/2} \quad (5.1)$$

with  $D$  being the shear-induced diffusivity. To reach a steady concentration profile we assume that  $l_y$  must be of the same order as the flow height, i.e.  $l_y \sim h_{ss}$  with  $h_{ss}$  the flow height when a steady concentration profile was reached. The self diffusion coefficient may be written as

$$D = d(\phi)\bar{\dot{\gamma}}a^2, \quad (5.2)$$

with  $\bar{\dot{\gamma}}$  the mean shear rate across the depth of the flow. From (5.1) and (5.2), it follows that

$$t_{ss} \sim \frac{h_{ss}^2}{4\bar{\dot{\gamma}}a^2 d(\phi)} \quad (5.3)$$

with  $t_{ss}$  as the time needed to observe a steady state concentration profile. Since  $\bar{\dot{\gamma}}$  was not constant during our experiment we used the time average of the mean shear rate  $\langle \bar{\dot{\gamma}} \rangle_t$  until

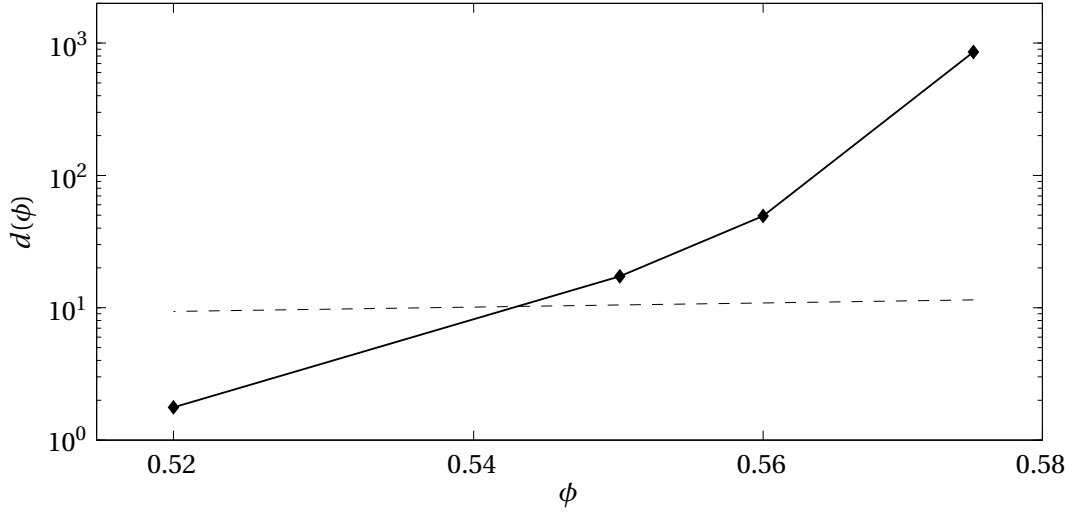


Figure 5.14: Estimation of  $d(\phi)$ . Black diamonds show the experimental data whereas the dashed line is the fit of a function  $f = A\phi^2$  on experimental results with  $\phi \leq 0.55$ .

time  $t_{ss}$  to compute an estimation of  $d(\phi)$ :

$$d(\phi) \sim \frac{h_{ss}^2}{4 \langle \bar{\gamma} \rangle_t a^2 t_{ss}} \quad (5.4)$$

The values of  $d(\phi)$  computed with equation (5.4) on runs (d, g, h, m) are shown in the log-log plot of Figure 5.14. For steady state times  $t_{ss}$ , we used the times at which, on Figure 5.11, the dashed line crosses the experimental data. The dashed line is a fit of a function  $f = A\phi^2$  on experimental  $d(\phi)$  (taking into account only  $d(\phi \leq 0.55)$ ). We found a much stronger dependence of  $d(\phi)$  on  $\phi$  than the  $\phi^2$  predicted by the theory and previously observed for concentrations ranging from 40% to 55% [90, 86, 58]. However, qualitatively, we observed the same behavior as already reported [47, 51], i.e. a very strong increase of  $d(\phi)$  for  $\phi \geq 0.55$ . In our case, we obtained  $d(\phi) \sim \phi^{g(\phi)}$ , with  $g(\phi) \approx 40$  for  $\phi \leq 0.55$  and  $g(\phi) \approx 100$  for  $\phi \geq 0.56$ . The strong dependence of  $d(\phi)$  on  $\phi$  compared to existing data and the fact that  $g(\phi)$  was not constant may be due to the simplifying hypothesis used to compute  $d(\phi)$  neglecting some of the true complexity of the flow.

### 5.2.3 Runs with high solid fractions ( $\phi > 0.55$ )

In this section we report results obtained with suspensions containing a solid fraction higher than 55%. The observed behaviors developed complexities, involving fracture, slip and intermittent motion. We found that the solid fraction and the initial released mass both played a crucial role in the dynamics. We begin this section by discussing the front position as a function of time and the velocity profiles. Then we carefully describe two regimes that were observed at longer times: a fracture regime and a stick-slip regime.

### Front positions and velocity profiles

Figure 5.15 shows the front positions  $x_f(t)$  for runs (h) to (p) (without run (k) whose solid fraction was only 52%), all runs were conducted with the flume inclined at 25 deg. In order to characterize the different regimes along the channel we computed the local fit of a function  $f(t) = At^n$  on the front positions, the results are depicted in Figure 5.16. Until the time  $t \sim 1$  s, all of the runs were in the inertial regime and thus had the same behavior since the typical velocity, in this regime, is not a function of the viscosity ( $U_* = (gH_* \cos\theta)^{1/2}$ ). At intermediate times, the front positions seemed to follow a power law  $x_f(t) \sim t^n$  with  $n \sim 0.2 - 0.3$ . This regime lasted longer for the smallest solid fractions and the biggest masses. For instance, run (l) (solid fraction 57%, mass 6 kg) displayed the same typical behavior as a viscous fluid: the value of  $n$  converged slowly to the theoretical Newtonian asymptotic value  $n = 0.33$ . We plotted on Figure 5.15 the asymptotic Newtonian solution (2.16) computed using a Krieger-Dougherty effective viscosity (2.17) with ( $n = 2, \phi_m = 0.625$ ). The close agreement between theory and experimental data for this run means that i) the global behavior of the flow was viscous, ii) a Krieger-Dougherty viscosity was well adapted for solid fractions as high as 57% despite the fact that the parameters were chosen for a suspension with a concentration of only 45%. On the other hand, when the released mass was only 3 kg, run (i) displayed a completely different behavior despite the fact that the solid concentration was the same as for run (l): after time  $t \sim 10$  s the flow slowed down abruptly and the  $n$  value dropped to  $n = 0.14$  before going up again.

To gain physical insight into this new regime occurring after the pseudo viscous regime, we plotted the velocity profiles at  $x_0 = 255$  cm for run (h) (Figure 5.17). We also plotted on Figure 5.18 the theoretical steady state velocity profiles obtained by integrating (2.26) with a Krieger-Dougherty effective viscosity ( $\beta = 2, \phi_m = 0.625$ ). The velocity profiles exhibited by run (h) looked very similar to the velocity profiles observed at smaller solid fractions. Near the front, profiles were parabolic, becoming more and more blunted closer to the tail. However, at these higher solid fractions, theory failed to catch the blunting. Careful examination of the PIV images revealed that the first layer of particles was moving on the bottom, a phenomenon not observed at lower concentration. Thus, we first thought that the excessive blunting was due to slip as reported by [91]. Figure 5.18, in the second line of plots, shows theoretical profiles corrected for a slip velocity  $u_s$ . Even taking into account a high slip velocity  $u_s = 20$  mm/s, theoretical profiles did not become as blunted as the experimental one.

Figure 5.19 shows the velocity profiles for run (i). During the first 2-3 seconds, the flow was not sheared behind the front and particles slid on the bottom of the channel. Then, slowly, as the flow depth increased, the flow became more and more sheared but this shearing remained localized in a thin layer of approximately 1-2 mm near the bottom of the channel. This behavior looked very similar to the flows of yield-stress fluids for which a critical height must be reached in order that the material start to flow. However, inspection of Figure 5.19 showed that no critical height could be defined. Near the front the plug height over the sheared layer was 12 mm whereas after  $\Delta t = 70$  s the height of the plug over the sheared region was only 9 mm. Note that the flow localization observed for run (h) and (i) was very similar to the flow localiza-

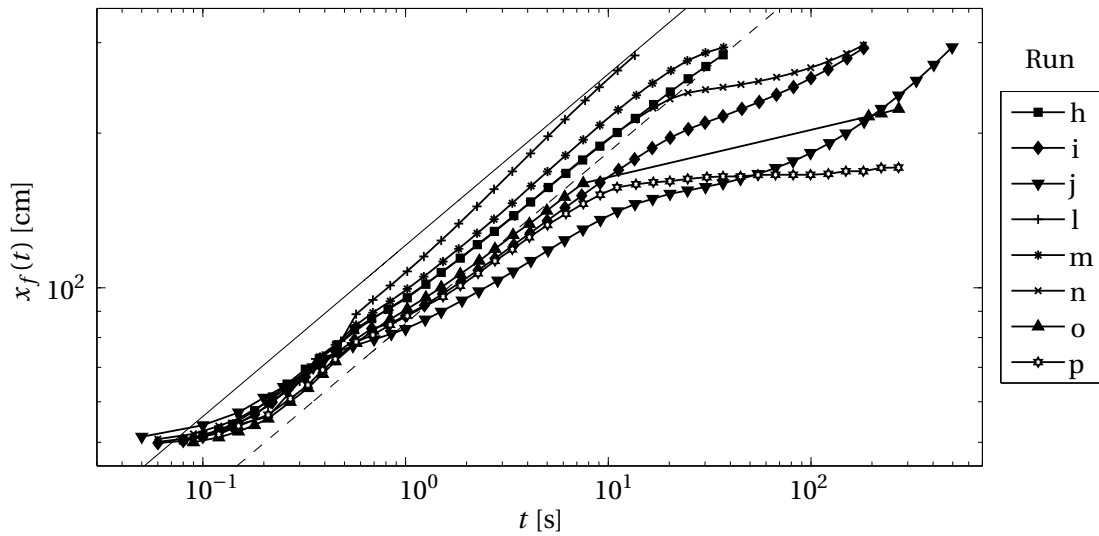


Figure 5.15: Front positions  $x_f(t)$  as a function of time for run with high solid fraction (0.56-0.595). We also plotted the Newtonian theoretical solution for run (h) (dashed line) and (l) (solid line). Computations were made using a Krieger-Dougherty effective viscosity ( $n = 2$ ,  $\phi_m = 0.625$ ).

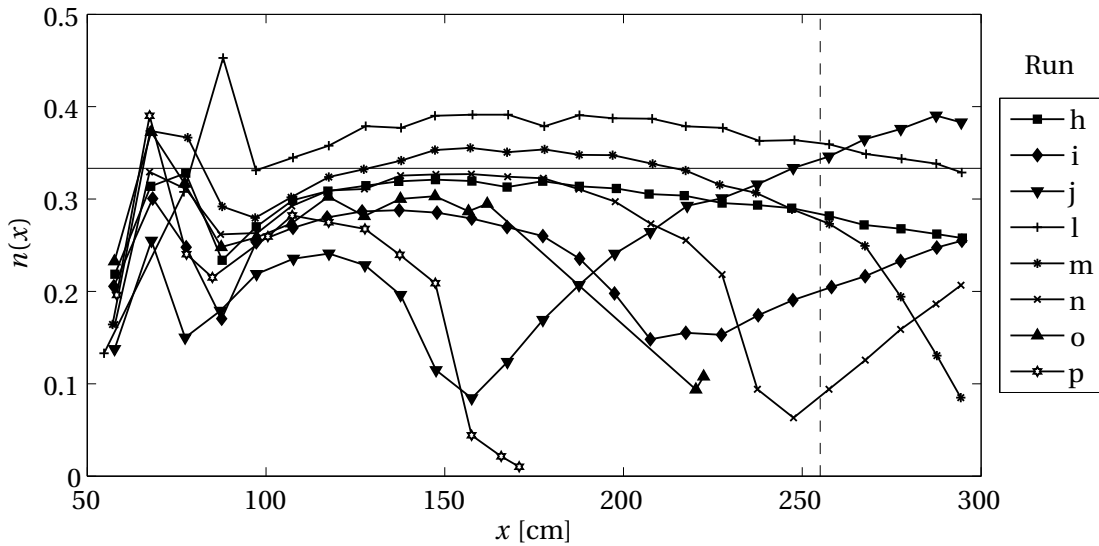


Figure 5.16: Values of  $n$  obtained using a function  $f(t) = At^n$  to locally fit data presented in Figure 5.15. The asymptotic  $n$  predicted by the theory,  $n = 1/3$  is also shown (solid horizontal line). The vertical dashed line indicates the position of the measurement window used for the velocity profiles measurements ( $x_0 = 255$  cm).

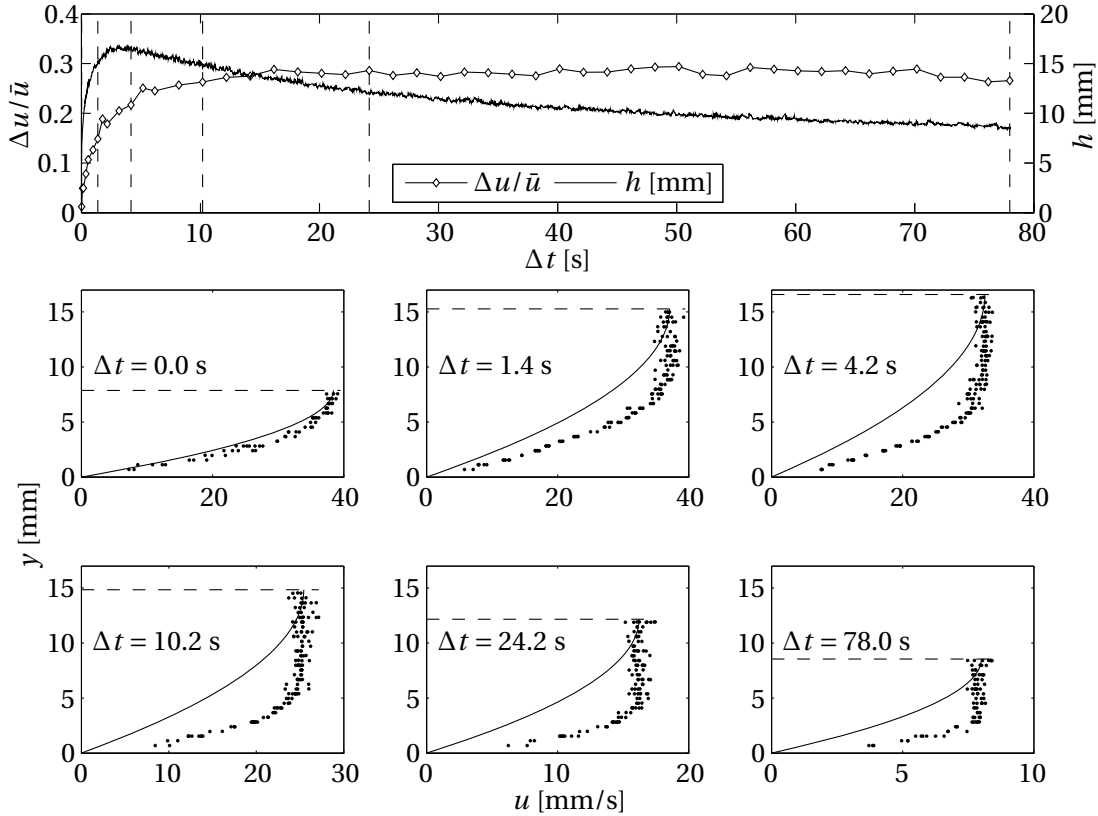


Figure 5.17: Same caption as Figure 5.8 but for run (h) ( $\phi = 0.56$ ,  $\theta = 25$  deg,  $m = 3$  kg).

tion observed in a wide gap Couette rheometer at low shear rates [92, 47]. However, Fall et al. [55] showed that this localization arose only when a density mismatch between the solid and liquid phases was present, which was not the case in our suspensions.

At the highest solid fractions ( $\phi = 0.595$ ) the front position moved like  $x_f(t) \sim t^n$  (Figure 5.15) until the flow stopped for short periods of time and the front began to move intermittently. Figure 5.20 shows in detail the front position of run (p). The times between movement increased from less than 2 s to more than 90 s. At longer times separation between fluid and solid phases occurred as previously observed by Nsom [30]. The solid frame stayed at rest while the fluid seeped through the granular media eroding the front.

### The influence of size distribution on flow dynamics

Dam-break experiments with non-sieved particles (size distribution shown on the left plot of Figure 3.3) were also conducted. A suspension with a fixed solid fraction of 59.5% was used and different masses were tested. Results are shown in Figure 5.21 (solid lines). We also plotted, on the same figure, for sake of comparison, results obtained with sieved suspensions (dashed and dotted lines). Behavior of the non-sieved suspensions looked roughly the same as the behavior



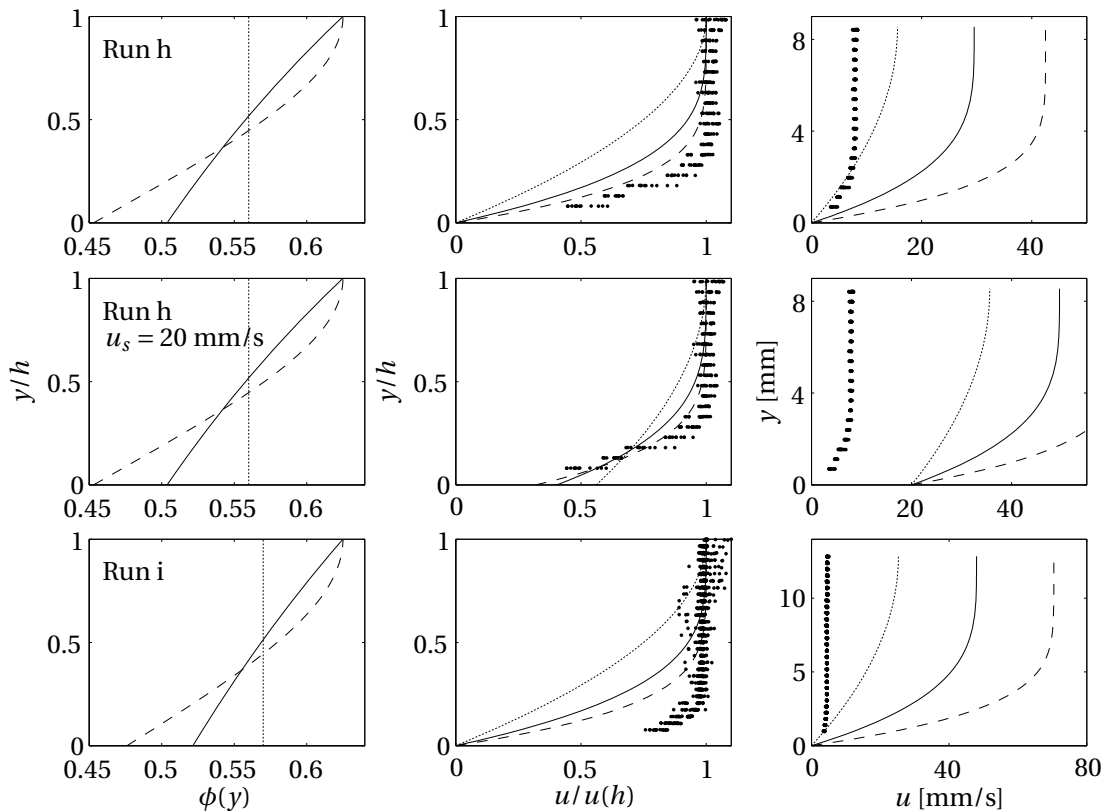


Figure 5.18: Same caption as Figure 5.12 but for runs (h) and (i); we tried to add a slip velocity of 20 mm/s on the results of run (h) (second line of plots).

of sieved suspensions: at intermediate times, the flow seemed viscous ( $x_f(t) \sim t^n$ ) whereas at longer times and for small masses the bulk slowed down and entered a new regime where shear was localized in a few layers near the bottom of the channel. Despite the similarities, there were substantial differences between the front positions of sieved and non sieved suspensions. The first difference arose from the fact that, for a given solid fraction, the effective viscosity of a suspension is lower when polydispersity is high [89, 93]. As depicted in Figure 5.21 the front position of run (t) (non-sieved,  $\phi = 0.595$ ,  $m = 6$  kg) was very close to the front position of run (m) (sieved,  $\phi = 0.575$ ,  $m = 6$  kg). The same observation was made for the 3 kg runs: the front position of the run (r) (non-sieved,  $\phi = 0.595$ ,  $m = 3$  kg) moved almost at the same speed as in run (i) (sieved,  $\phi = 0.57$ ,  $m = 3$  kg) during the viscous regime. However, shifting the solid fraction or setting  $\phi_m$  to a higher value was not sufficient to fully acknowledge the polydispersity, since, as shown on Figure 5.21, sieved and non-sieved trajectories can cross each other. In particular non-sieved flow seemed to slow down more rapidly than sieved flows. For instance, in the viscous regime, run (r) flowed faster than run (j) but trajectories finally crossed at time  $t = 345$  s.

This difference between sieved and non-sieved suspensions at long times can arise from different phenomena. Intrinsic rheological dissimilarities, for example if one of the distribution is more markedly shear thinning or shear thickening. However, migration may also play a role.

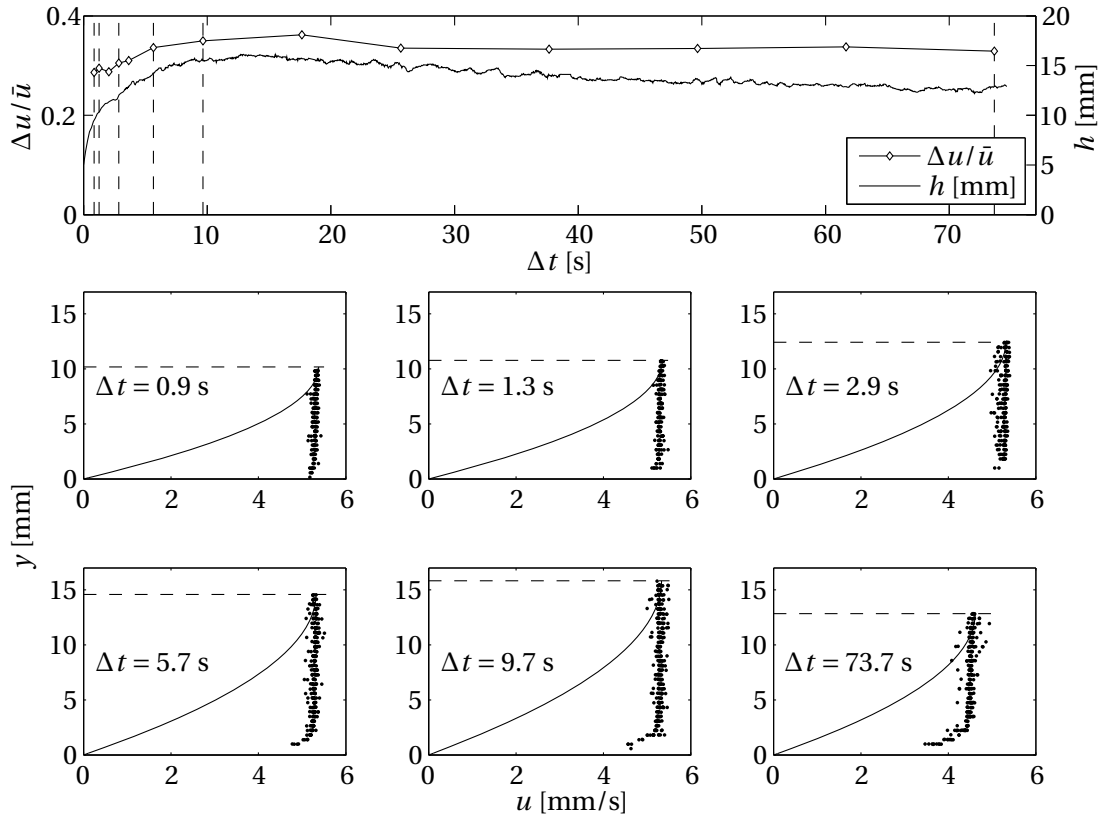


Figure 5.19: Same caption as Figure 5.8 but for run (i) ( $\phi = 0.57$ ,  $\theta = 25$  deg,  $m = 3$  kg).

Since the typical time scale for migration is smaller for big particles than for small particles, size segregation occurs in polydisperse flows [66, 94]. For free surface flows, the concentration of smaller particles is higher near the bottom and lower at the free surface [88]. According to [64] the typical migration time is inversely proportional to the square of the radius of the particle ( $t_{mig} \sim a^{-2}$ ), leading in our polydisperse suspension to a migration rate 400 times slower for smaller particles and, consequently, to a segregated flow.

### Free surface fractures

When the concentration was sufficiently high, the body of the avalanche started fracturing like a creeping (landsliding) mass of soil. We focus on run (u) but the same kind of behavior was observed for runs (m-u): A few seconds after the release (typically  $t > 3 - 5$  s for a mass of  $\sim 7$  kg), we observed that the free surface deformed and became wavy. As shown by Figure 5.22, the fractures formed a regular three-dimensional pattern (with an initial wavelength of approximately 10 cm, growing up to 100 cm) which spanned the entire length of the flow. The fractures looked like the type of fractures observed in cohesive soils, i.e. with a curved slip surface inside the material, along which the shear is localized. When these fracture regions grew sufficiently in size, they modified the local velocity field substantially. For the sake of

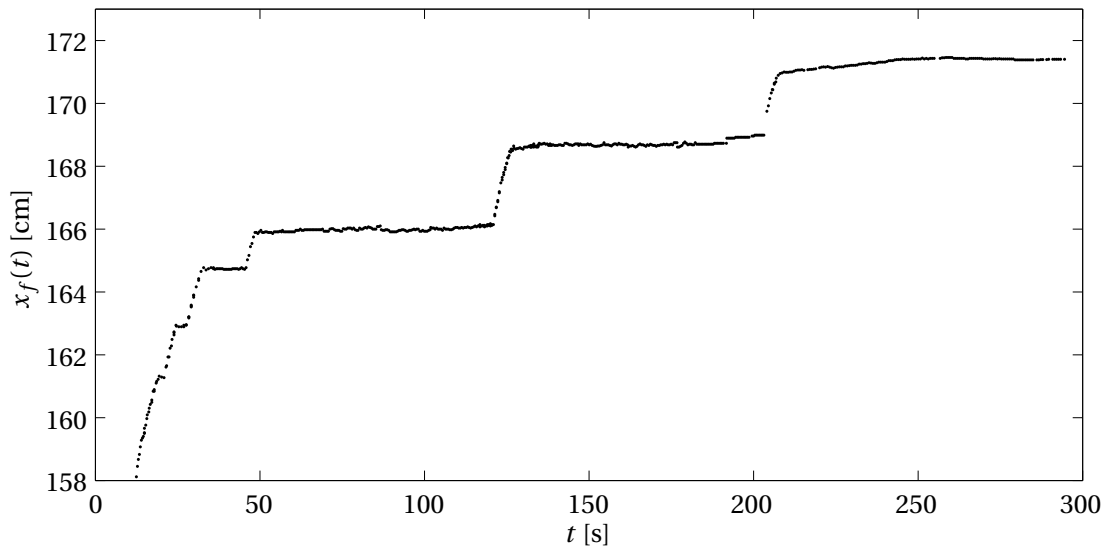


Figure 5.20: Detail of the front positions  $x_f(t)$  as a function of time for run (p). The released mass was 6 kg and the suspension solid fraction 59.5%.

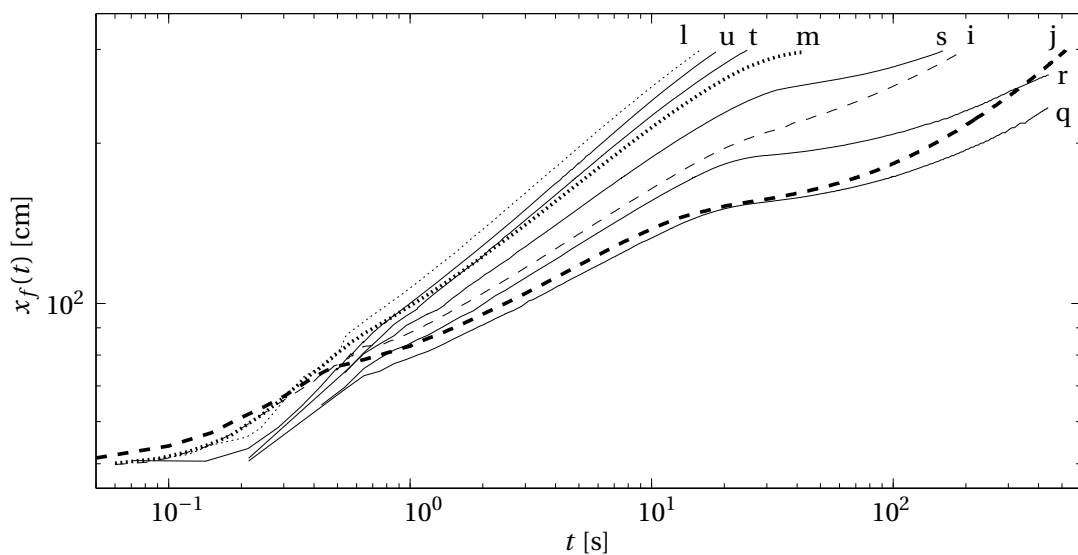


Figure 5.21: Comparison between non-sieved (solid lines) and sieved runs (dashed and dotted lines). The solid fraction for the non-sieved suspensions was held fixed to 59.5% and we tested a range of different masses: 7.940 kg, 6 kg, 4 kg, 3 kg and 2 kg (respectively run u, t, s, r, q). The thin dashed line stand for run (i) ( $\phi = 0.57$ ,  $m = 3$  kg, sieved particles) and the thick dashed line stand for run (j) ( $\phi = 0.58$ ,  $m = 3$  kg, sieved particles). The thin dotted line stand for run (l) ( $\phi = 0.57$ ,  $m = 6$  kg, sieved particles) and the thick dotted line stand for run (m) ( $\phi = 0.575$ ,  $m = 6$  kg, sieved particles). The slope was 25 deg for all runs.

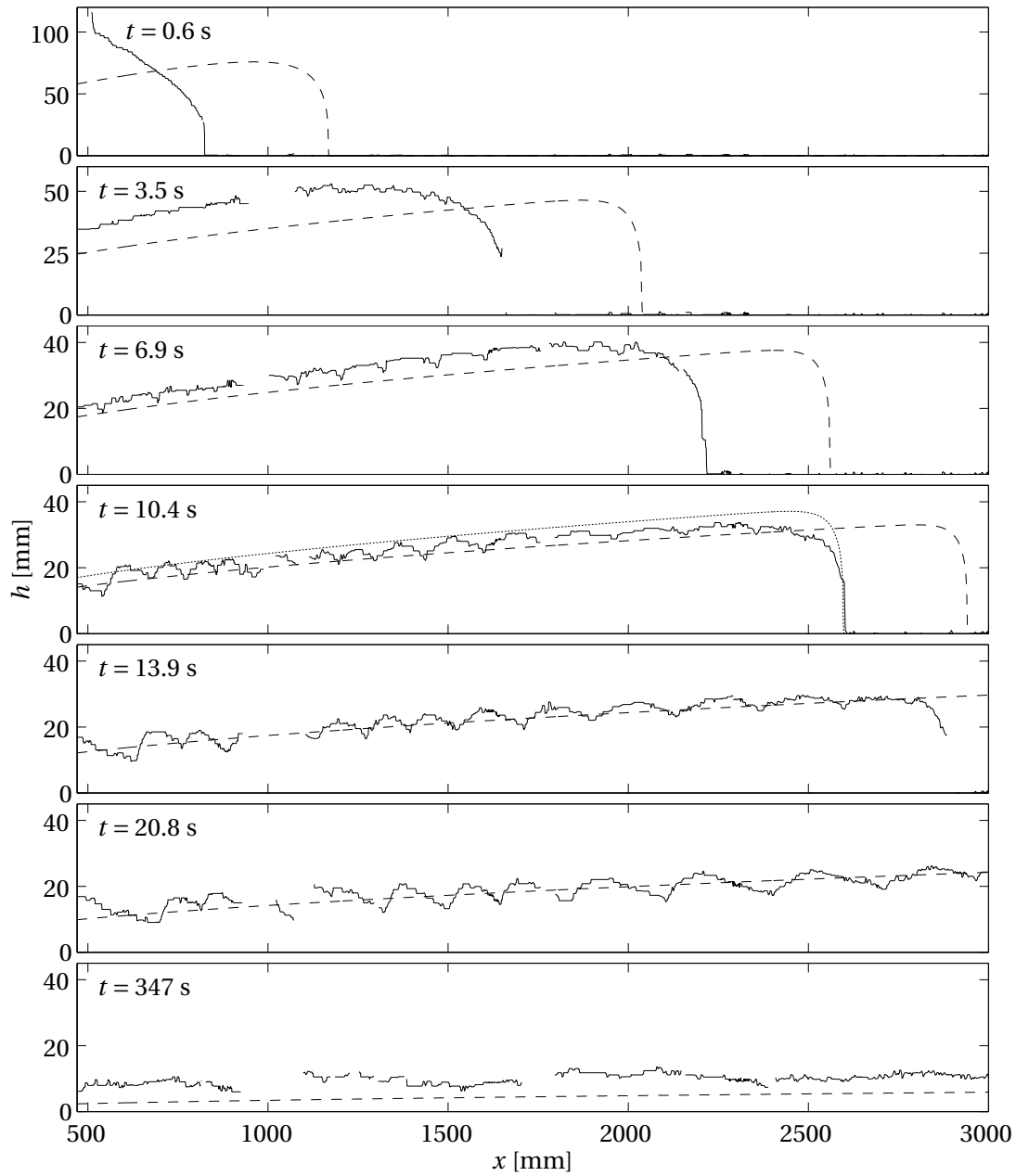


Figure 5.22: Longitudinal flow depth profiles taken at different times for run (u). Measurements were made using a laser sheet inclined at low angle and reflecting on the surface (see A.1). Dashed lines stand for the numerical solution of (2.14) computed using a Krieger-Dougherty effective viscosity model ( $n = 2$ ,  $\phi_m = 0.625$ ) and a corrected solid fraction  $\phi = 0.575$  to take into account the fact that the particles were not sieved (Figure 5.21 showed that a  $\phi = 0.595$  non-sieved suspension flowed almost like a  $\phi = 0.575$  suspension in the pseudo viscous regime). To focus on the shape of the free surface we also added (dotted line) on the  $t = 10.4$  s subplot the theoretical time-shifted flow depth ( $\Delta t = -3.2$  s).

comparison we added on Figure 5.22 the theoretical free surface shape predicted by the lubrication theory (2.14). Despite the fractures, the general shape was still well predicted using the viscous theory.

Figure 5.23 shows a sequence of snapshots taken every 0.5 s. At  $t = 49$  s (the first image in the upper left corner of the figure), the suspension moved almost as a rigid block since there was almost no shear in the vertical direction (all the shear being localized within a thin layer along the solid boundary). At  $t = 50$  s, there was a significant decrease in the flow depth, accompanied by a marked reduction in the velocity intensity. Interestingly enough, at  $t = 50.5$  s, this region quickly collapsed and gave rise to two flow regions separated by a 3-mm thick layer, inclined at 25 deg to 30 deg with respect to the bottom and characterized by a sharp velocity gradient: the upper region clearly slid on the lower region, which slid on the flume bottom. At  $t = 52$  s (image in the lower left corner of the figure), the fractured region left the observing window and a quieter region (low velocity, no shear) occupied the field filmed by our camera; note that the flow depth eventually started increasing again due to subsequent fractures passing through the measurement window.

Figure 5.24 reports the cross-stream flow-depth profiles at different times. The profiles were symmetric and exhibited two cusps, which were the lateral borders of the fracture (as shown by Figure 5.25, the slipping surface was delineated or flanked by two curvilinear levees along each sidewall). The fracture process lasted a few tens of seconds. Its effects became progressively weaker. Typically, at  $t = 100$  s, the flow was a thin creeping layer (approximately 13 mm in thickness, moving at a mean velocity 5 mm/s).

### Stick-slip regime

At longer times, a third regime occurred: we observed intermittent motion, with phases during which the suspension accelerated vigorously and reached a quasi-steady regime, and phases during which the suspension came suddenly to a halt. We refer to this regime as the stick-slip regime.

Figure 5.26 shows the time evolution of the depth averaged velocity, measured at the center of the channel during run (u). At short times ( $t < 20$  s) the velocity was high, corresponding to the front of the flow passing over the measurement windows. Later, two fractures occurred at times  $t = 30$  and  $t = 48$  s. Before each fracture the velocity briefly increased corresponding to the upper layer sliding at high speed on the bottom layer. Once the upper layer had been completely removed, the velocity strongly decreased. After the second fracture the velocity fell to less than 3 mm/s and was almost constant for 3 minutes. During this time the flow slid on the bottom of the channel without shear until it first came to rest, corresponding to the beginning of the stick-slip regime ( $t = 3.8$  min).

The duration of the slip phase decreased with time, at  $t = 4$  min, the start of the regime, the typical duration was 11 s while at  $t = 32$  min, the typical duration dropped to less than 3 s. In

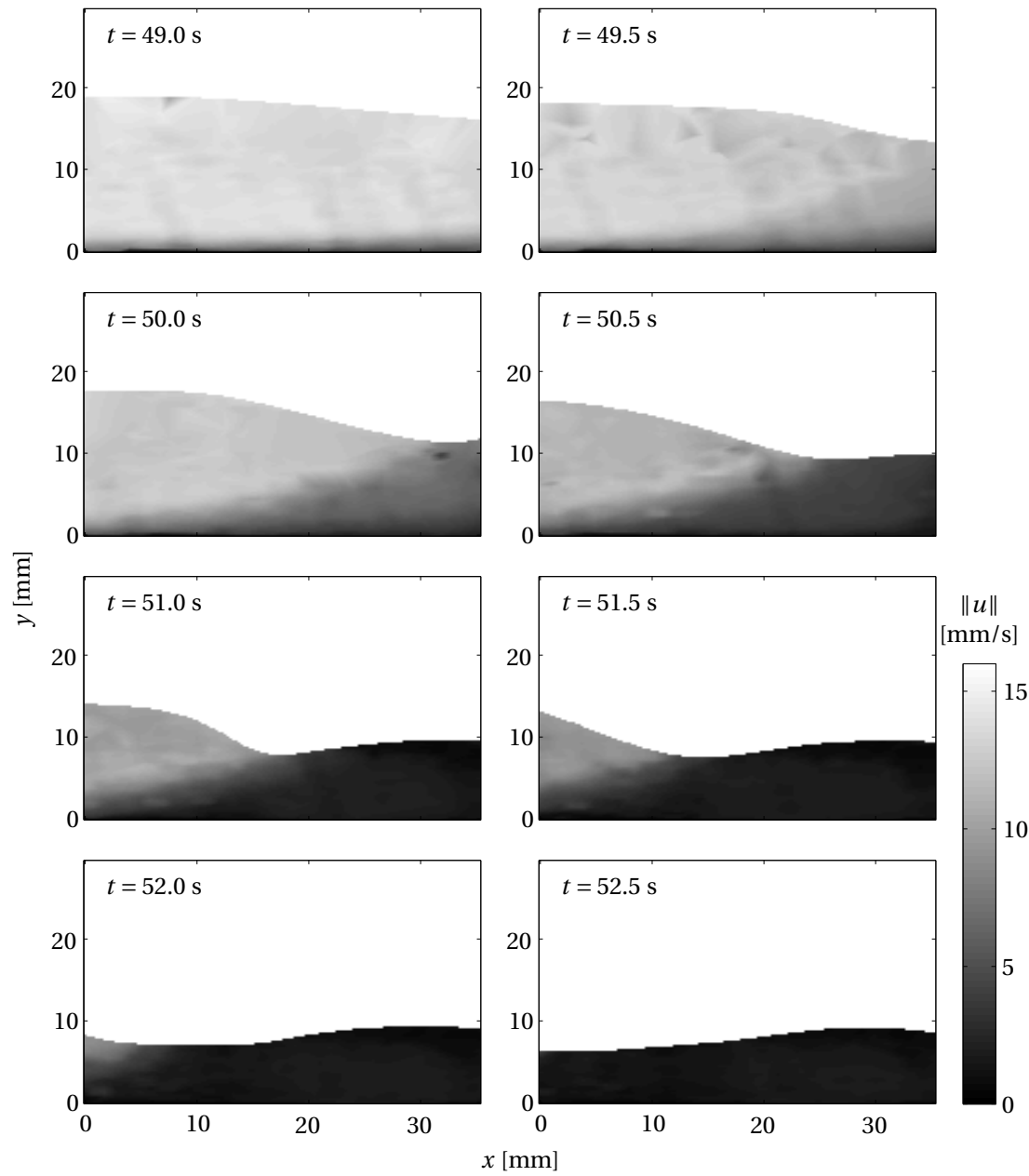


Figure 5.23: Snapshots showing the velocity distribution within the flowing suspension during the fracture process (flow from right to left); we only report the velocity norm  $\|u\| = \sqrt{u^2 + v^2}$ . The time increment between successive images was 0.5 s, the released mass was  $m = 7.9$  kg,  $\phi = 0.595$ ,  $\theta = 25$  deg, particles were not sieved (run u). Measurements were made at the downstream coordinate  $x_0 = 255$  cm on the centerline of the flume  $z = 5$  cm.

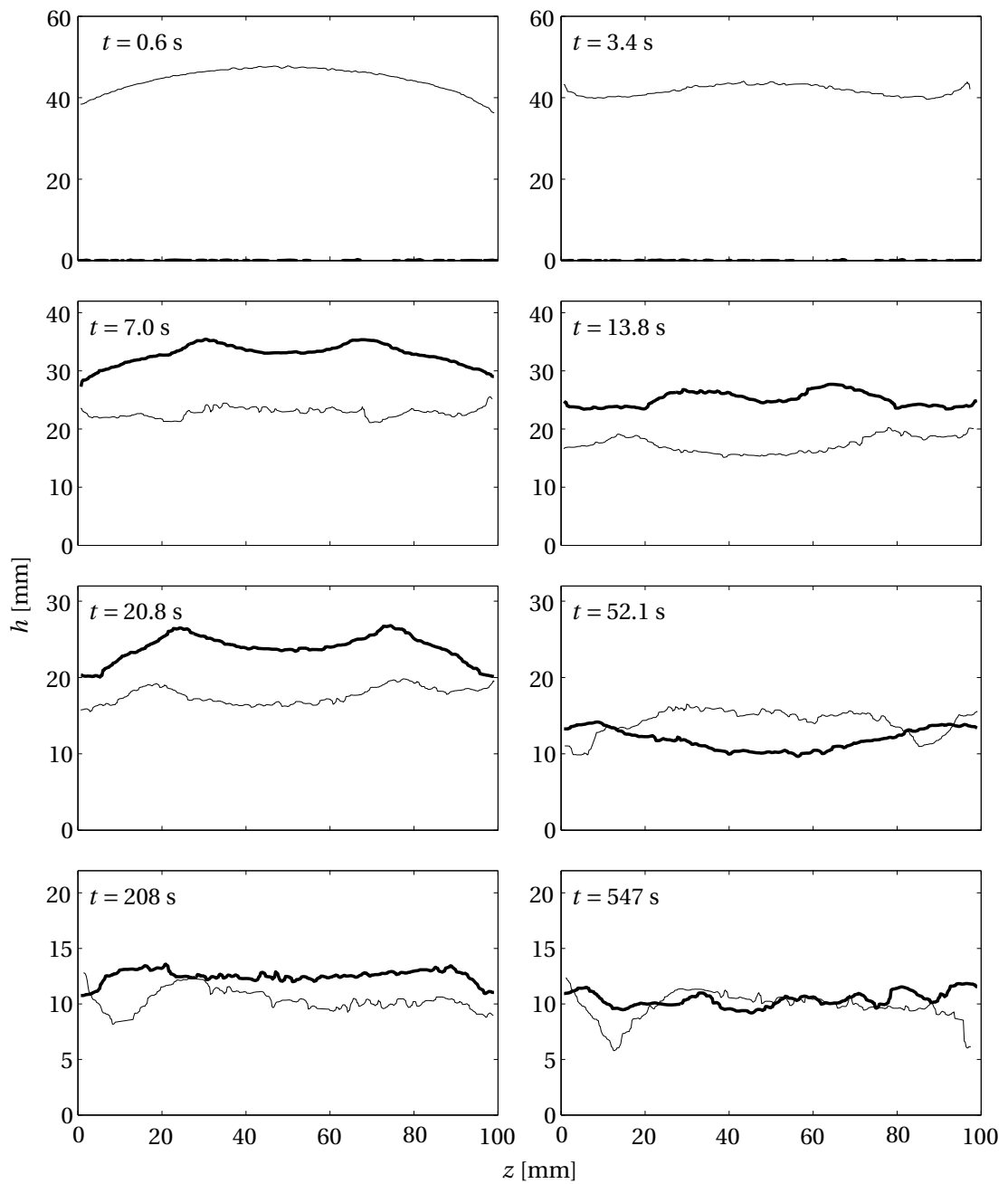


Figure 5.24: Run (u): cross-stream flow depth profiles taken at different times and two different positions along the channel  $x = 66$  cm (thin line) and  $x = 205$  cm (thick line). Flow depths were obtained projecting an inclined laser sheet on the free surface (A.1).

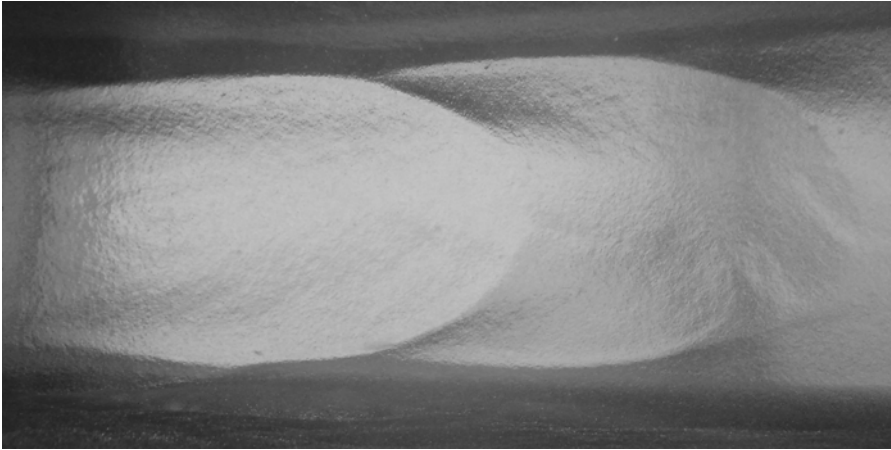


Figure 5.25: Picture of a fracture view from the top. The flume width is 10 cm, the typical length of the fracture is 10-15 cm (flow from right to left).

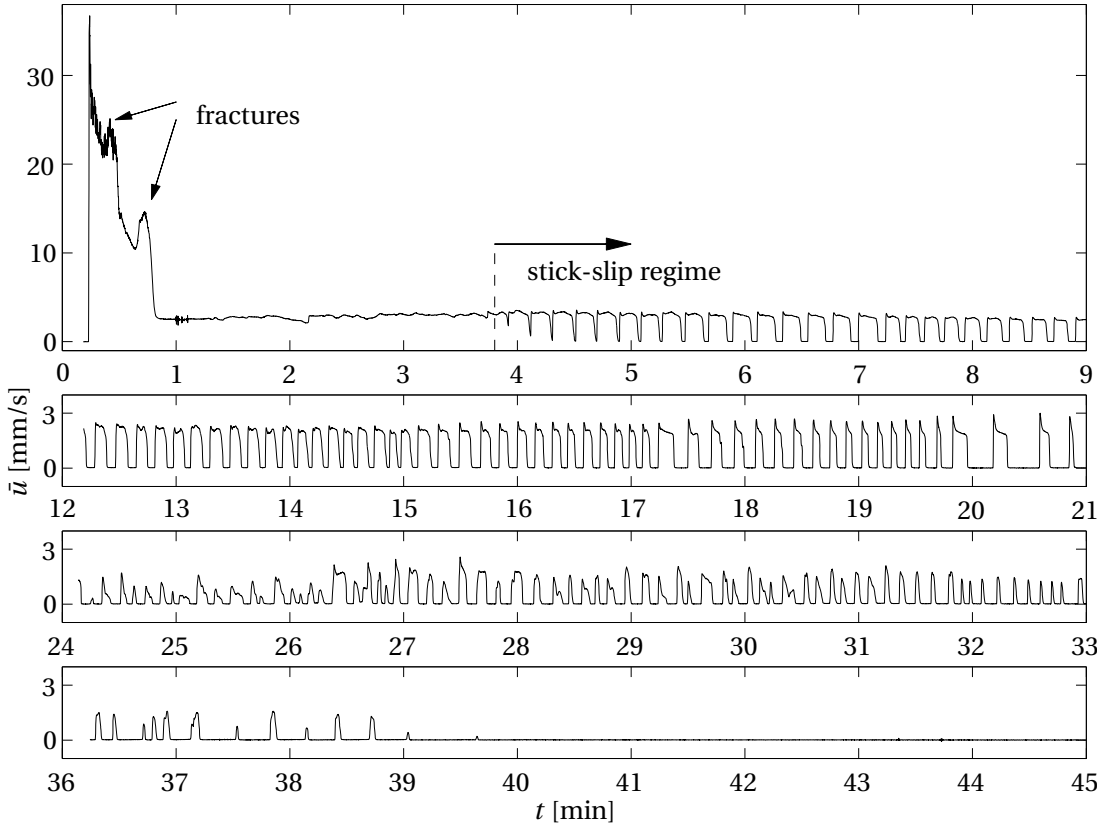


Figure 5.26: Run (u): time evolution of the depth average velocity. Measurements were taken at  $z = 5$  cm (centerline of the flume) and downstream coordinate  $x_0 = 255$  cm.



contrast, the duration of the stick phase increased more strongly, from a few milliseconds (at  $t = 4$  min) to 12 s (at  $t = 32$  min). The stick-slip regime lasted a few tens of minutes until the material came progressively to a final halt. Complete stoppage was first observed in the upper part of the flume and it took several minutes for all of the suspension to come to an arrested state. At the end of the stick-slip regime a 10-mm thick deposit of suspension covered the bottom. Fluid seepage (self-filtration) was then observed: the interstitial fluid was drained from the bulk and flowed in narrow rivulets, which progressively incised the bulk down to the base (see Figure 5.27). Interestingly, this phase separation was fairly fast since it occurred a couple of hours after the start of the experiment, whereas in the sedimentation experiments we carried out during our preliminary tests, we observed no phase separation even after one week.

To gain physical insight into the processes at play during the stick and slip phases, we monitored the evolution of the interstitial fluid pressure at the bottom (basal pore pressure)  $p$ , the flow depth  $h$ , and the velocity profile  $u(y, t)$ ,  $v(y, t)$  at the position  $x_0 = 255$  cm. Figure 5.28 shows the time variations in  $p$ ,  $h$  and the depth-averaged streamwise and cross-stream components of the velocity ( $\bar{u}$  and  $\bar{v}$ , respectively) during one cycle of slipping. Figure 5.29 is a close-up of the former figure to show the evolution at short times. As soon as the suspension started to move, the normal component  $v$  increased significantly for approximately 0.2 s, showing that the material underwent dilation. Near the bottom of the flume the vertical velocity  $v$  remained small, whereas close to the free surface, in the upper layers of the flow,  $v$  reached its maximal value. The dilation however was small: the maximal vertical velocity  $v$  was 0.2 mm/s near the free surface and lasted less than 0.4 s, producing a maximum displacement of 80 – 100  $\mu\text{m}$  (i.e. about half a particle diameter).  $v$  became negative 0.4 s after the motion started ( $t = 1.4$  s), meaning that the flow was contracting and after 2 s the initial flow height was recovered. Thus, surprisingly, contraction of the flow is not correlated with flow halt.

The maximal streamwise velocity  $u$  was reached at the maximal dilatation (i.e. just before  $v$  became negative), then,  $u$  slowly decreased to an almost constant value. Until the time  $t = 2$  s, values of  $u$  near the bottom were 7% smaller than values obtained close to the free surface, meaning that the flow was slightly sheared during the acceleration of the bulk. After  $t \sim 2$  s, the values of  $u$  near the bottom of the flume became identical to the free surface velocity: the bulk was slipping with no internal deformation. This is particularly obvious on Figure 5.29, in which velocity profiles  $u(y)$  computed at different times are shown. Profiles (A) to (D) corresponded to acceleration, while profiles (E) to (I) correspond to deceleration.

The pore pressure began to increase at the same time as the flow started to move as shown in Figure 5.29. The magnitudes of basal pore pressure fluctuations were much larger than the flow depth variations, meaning that the pore pressure was not hydrostatic. Excess pore pressures ( $p_{ex} = p - h$ ) remained negative during the entire stick-slip cycle ranging from  $-3.5$  mm of fluid just before the flow initiation to  $-1.5$  mm of fluid at  $t = 10$  s. Once the maximal pore pressure was reached, the pressure started to relax first slowly, then more rapidly. This decay induced deceleration of the suspension and eventually flow arrest. At rest the pressure continued to decrease linearly until the next slip cycle.

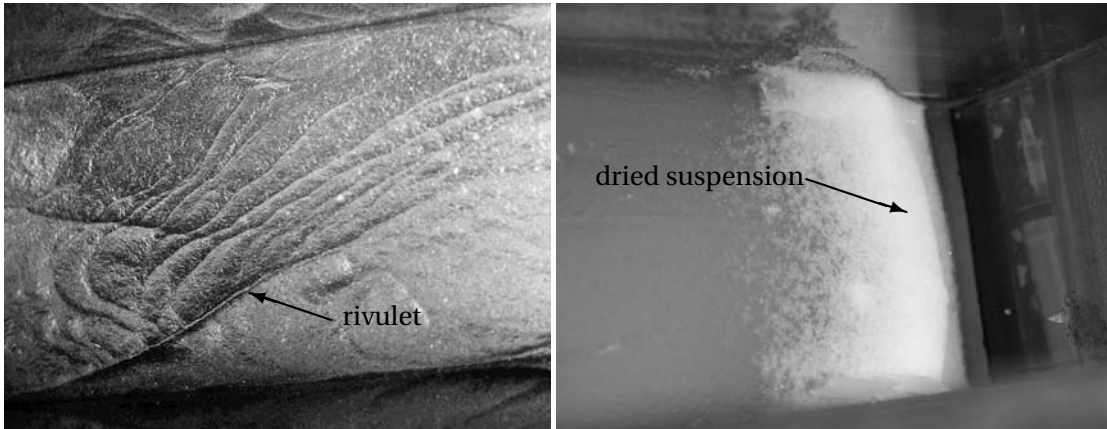


Figure 5.27: Picture of the free surface taken 60 min after dam-break for a  $\phi = 59.5\%$  sieved suspension (run p). Left: picture taken at  $x \sim 150$  cm. At the bottom of the image a rivulet draining the interstitial fluid can be identified. Other ripples are formed by the slow creeping of the bulk (flow from right to left). Right: a view of the upper end of the reservoir, fluid seepage has dried the bulk and only the solid frame remains at rest (flow from right to left).

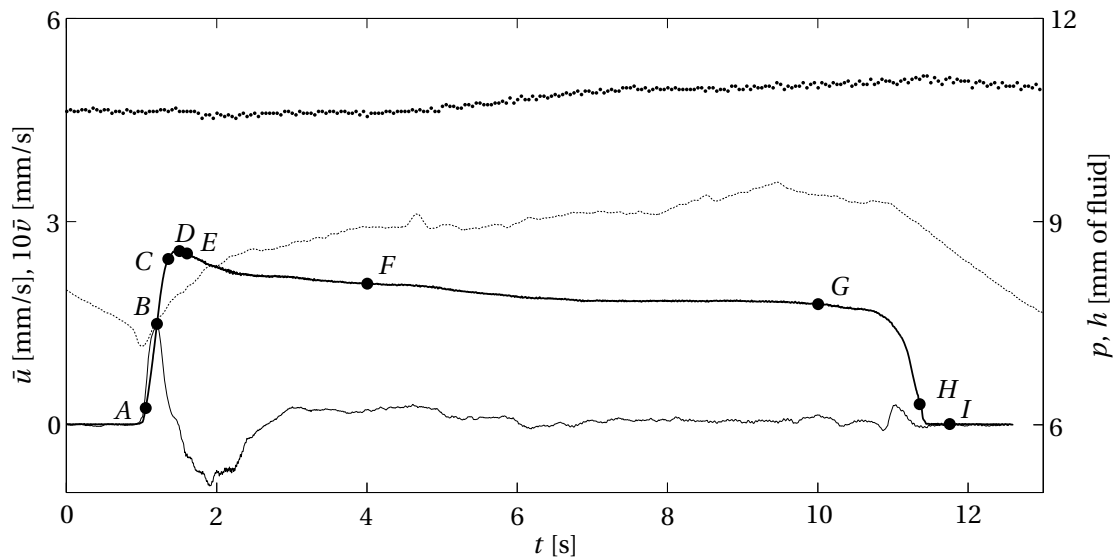


Figure 5.28: Time variations in depth-averaged velocity components  $\bar{u}$  (thick solid line) and  $\bar{v}$  (light solid line) together with basal pore pressure  $p$  (dotted line) for one cycle of slipping. Flow depth is indicated by small dots. Large dots labeled from (A) to (I) refer to the times at which the velocity profiles of Figure 5.29 have been plotted. Time  $t = 0$  corresponds to 623 s after the initial release, measurements were taken on run (t) at the centerline ( $z = 5$  cm) at the downstream coordinate  $x_0 = 255$  cm. Technical details of flow depth and pore pressure measurements can be found in A.1 and A.2.

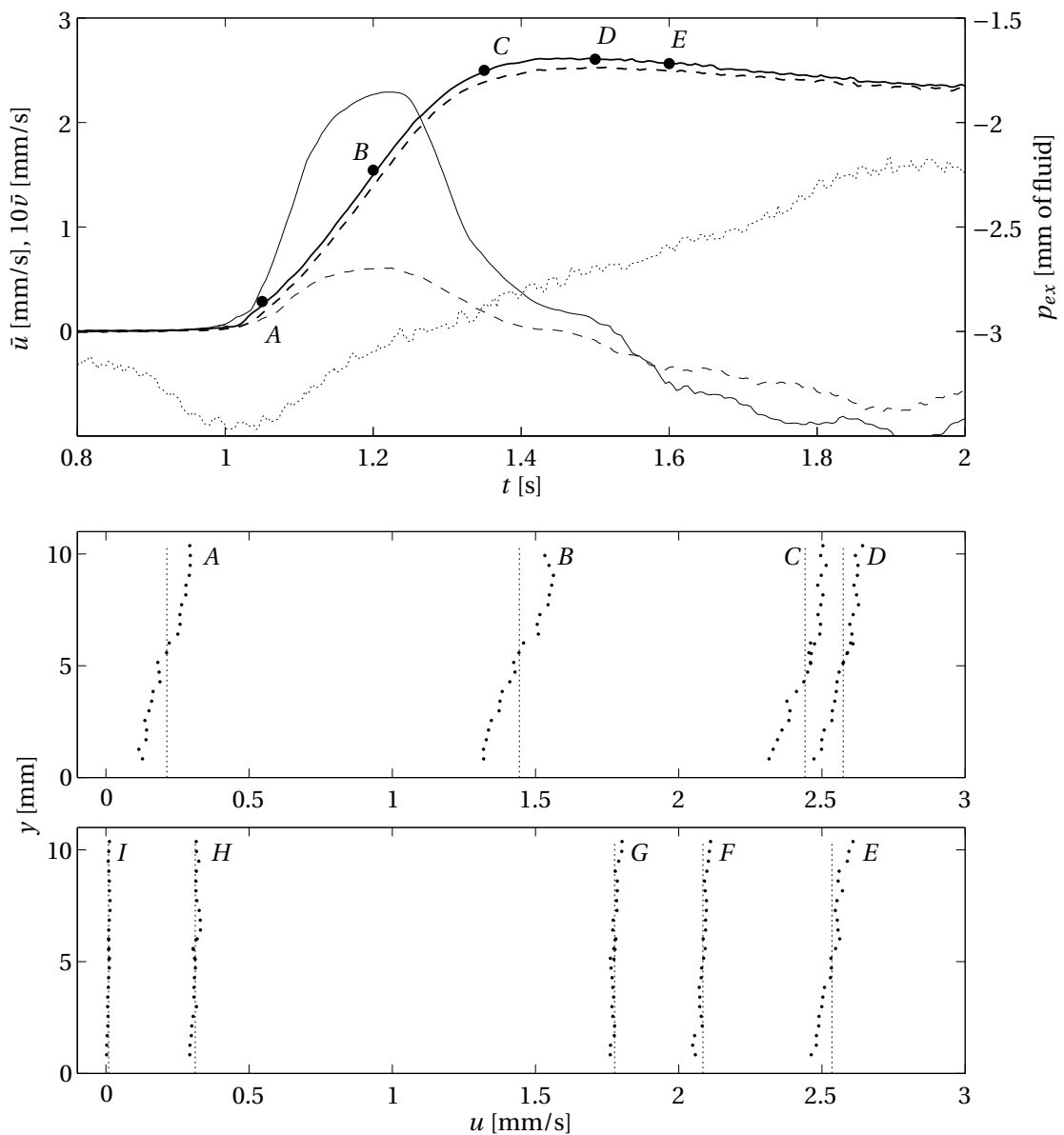


Figure 5.29: Top: detail of Figure 5.28. We split the depth-averaged velocities in two: bottom region ( $y = 0$  to  $y = h/2$ ) and top region ( $y = h/2$  to  $y = h$ ). Dashed lines stand for the bottom region whereas the solid line stands for the top region; the thick line stands for the streamwise velocity  $u$ , whereas the thin line stands for the vertical velocity  $v$ . We also plotted the excess pore pressure  $p_{ex} = p - h$ , with  $p$  the basal pore pressure and  $h$  the flow height. Bottom plots: Velocity profiles  $u(y)$  at times (A)  $t = 1.05$  s, (B)  $t = 1.20$  s, (C)  $t = 1.35$  s, (D)  $t = 1.50$  s, (E)  $t = 1.60$  s, (F)  $t = 4.00$  s, (G)  $t = 10$  s, (H)  $t = 11.35$  s, (I)  $t = 11.75$  s. Time  $t = 0$  corresponds to 623 s after the initial release. The vertical dashed lines stand for the mean (depth-averaged) velocities.

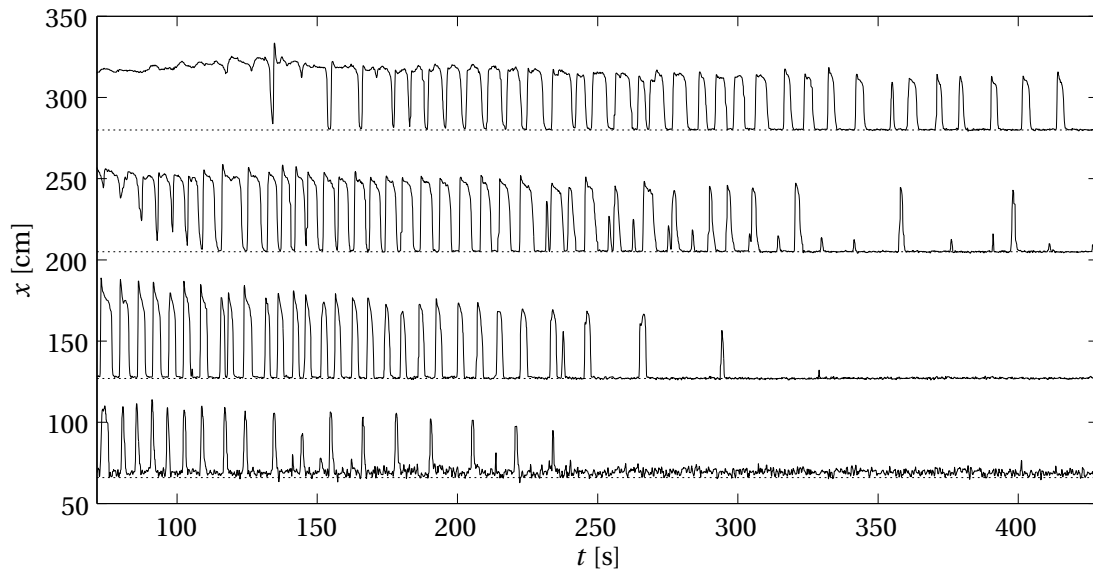


Figure 5.30: Time evolution of the free-surface velocities taken simultaneously at different places along the channel  $x = 66, 127, 205$  and  $280$  cm. The released mass was  $m = 7.94$  kg, solid fraction  $\phi = 0.595$ , slope  $\theta = 25$  deg with non-sieved particles and the typical velocity was  $\sim 2$  mm/s.

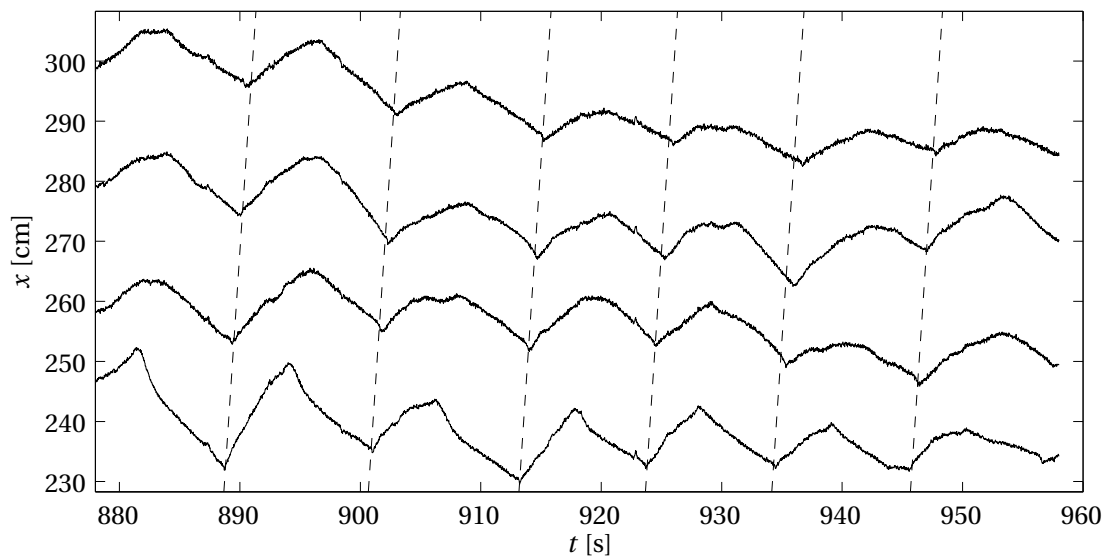


Figure 5.31: Basal pore pressure monitored along the channel at four different places:  $x = 238.3, 256.4, 274.2$  and  $292.3$  cm. The dashed lines show a propagation wave with a celerity of  $30$  cm/s. Technical details of pore pressure measurements can be found in A.2.

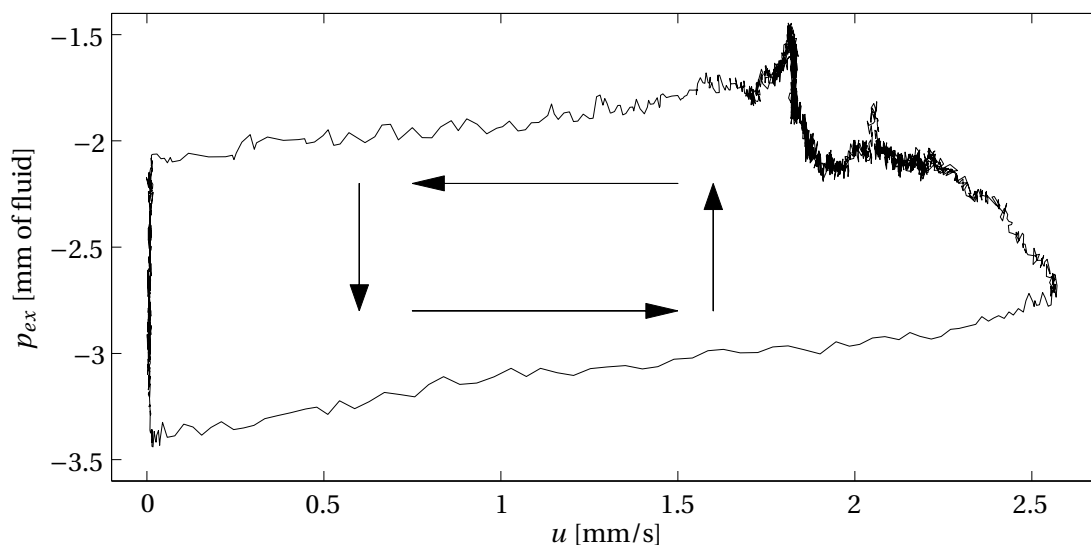


Figure 5.32: A stick-slip cycle: the streamwise velocity  $u$  versus the excess pore pressure  $p_{ex}$ , the trajectory is counterclockwise.

Initially, we thought of cyclic traveling waves as originating from the flume inlet and causing the pore pressure fluctuations. However, cross-correlating the velocity signals recorded in different places ( $x = 66, 127, 205$  and  $280$  cm) did not reveal any traveling waves at the channel length scale. As shown by Figure 5.30, the slipping phases occurred at different times and were not interrelated. However, examining smaller length scales ( $L \sim 60$  cm or less) as shown by Figure 5.31, revealed pressure waves. Limited propagation lengths may be caused by frequency mismatch: at a given place along the channel, as depicted by Figure 5.26, the shape of the stick-slip cycle changed with time, the duration of the stick phase increased whereas the slip phase duration decreased. Due to the fact that the stick-slip regime didn't start at the same time everywhere along the channel but was initiated earlier close to the door before propagating downstream, at a time  $t$  the stick-slip frequency varied at different places along the channel and thus general unified movement was impossible.

It is not clear why the stick-slip frequency evolved with time or what are the conditions required for initiation of the phenomenon in our setup are. This kind of intermittent motion is very common when two solids are rubbed together [95, 96]. The following analogy is used most of the time to illustrate the origin of stick-slip dynamics [97]. Consider a block attached to a spring and pulled at a constant velocity. At the beginning, the block sticks to the surface because the spring force  $F_s$  is smaller than the static friction force  $F_r$ . During this period the spring is stretched more and more and  $F_s$  rises continuously. When  $F_s$  exceed  $F_r$  the block starts to accelerate and  $F_s$  drops until the block stops. The cycle is repeated as long as the spring is pulled and this is due to the fact that the dynamic friction force  $F_d$  is smaller than  $F_s$ . For a given block attached to a given spring pulled over a given surface, stick slip may only occur below a threshold velocity. Above this velocity the motion becomes steady.

Stick-slip motion also occurs in experiments involving granular media such as grains in annular shear cells [98], a plate pushed on a granular layer [99], beads in a shear box [100] or in a pipe [101]. Adding liquid to grains sheared by a vane revealed that lubrication increases the slip recurrence interval [102].

Intermittent motion in a flume was observed by Iverson et al. [103] who investigated the rain-induced triggering of landslides by running large-scale experiments. Their experiments consisted of a layer of loose soil at rest on a sloping bed, in which the water content was progressively increased with the aid of sprinklers and drains. Depending on its initial porosity, the soil layer partially liquified or moved intermittently. Iverson [104] developed a constitutive equation combining Coulomb friction, contraction/dilatancy, and generation/diffusion of pore pressure. Idealizing the soil layer as a sliding block with velocity-dependent friction, Schaeffer and Iverson [105] derived a simplified set of governing equations that admitted analytical solutions. In particular, they showed that time-periodic behavior appeared in the problem in the form of intermittent motion (episodes of rapid slipping alternating with periods of no slipping) as the pore pressure fluctuated due to pore contraction/expansion and its diffusion through the pores. This theoretical description is clearly in line with our observations, however, agreement is not complete. In the paper by Schaeffer and Iverson, a lot of idealization was needed to make the equations tractable. In particular, the authors assumed the Coulomb friction coefficient to be a decreasing function of the velocity for an unstable steady state solution. In this case and for certain initial conditions, their governing equations lost stability through a subcritical Hopf bifurcation. In the phase plane showing the evolution of the velocity and excess pore pressure, the solution experienced sticking behavior during which the pressure increased and slipping behavior during which the pressure was mainly decreasing. In their model the duration of the stick phase increased and trajectories tended to a periodic orbit. In our case although we indeed observed an increasing duration of the stick phase (see Figure 5.26), the pore pressure decreased during stops and the trajectories in the  $u - p_{ex}$  phase plane were counterclockwise (Figure 5.32).

Pailha [106] investigated experimentally the flow initiation of granular material, fully immersed in a liquid. To that purpose, they instantaneously tilted a box filled with liquid and grains, then, monitored the pore pressure and the velocity of the solid phase. They found that for a sufficiently high ( $\phi \sim 0.58$ ) initial volume fraction, the flow didn't start immediately as the box was inclined. A delay was observed during which the flow was creeping and basal pore pressure fell. Once the flow developed fully the pressure increased again to a steady state value. Pailha [106] showed, using the idealized picture of landslides described by Iverson, that this delay was due to the time needed for the fluid to pass through the granular layers. Despite the fact that we were not able to identify a creeping phase, this interpretation of Iverson's model seems in good agreement with our measurements since the pressure decreased linearly before flow initiation, and rose rapidly when the flow started. Pailha [107] devised a depth-averaged two-phase flow model to accurately predict pore pressure fluctuations during the flow initiation, however, no deceleration is predicted by the model and at long times, the velocity tends to a steady state value. In conclusion, we think that the model of a sliding

permeable block developed by Iverson, or Pailha's two-phase flow model are consistent with our data, however, some extra physics is necessary, in order to completely describe our observations. In particular, we think that surface tension might play a role in the stick-slip motion, making the free surface an elastic membrane applying downward pressure to the particle skeleton and in this way helping the flow to stop. A strong surface tension effect is consistent with the corrugated surface observed at high solid fractions.

### 5.3 Summary

In this chapter we addressed the problem of a dam-break for granular suspensions with solid concentrations ranging from 15 to 59.5%. A variety of behavior was observed depending on the particle concentration, the slope or the mass released.

With solid fractions of up to 45%, our suspensions behaved as homogeneous viscous fluids. During the time scale of the experiment it was not possible to detect any inhomogeneities due to migration or sedimentation processes. In the range of shear rates tested and with the precision allowed by the setup it was not possible to detect shear thickening or shear thinning since the velocity profiles were perfectly Newtonian. Furthermore, the effective viscosity of the suspension was accurately estimated using a Krieger-Dougherty model (2.17) with  $\beta = 2$  and  $\phi_m = 0.625$  which is consistent with [47].

For slightly more concentrated suspensions (up to 55%), we found that the flow dynamics at the bulk scale could still be described using viscous theory and an effective viscosity. However, at the local scale, migration occurred producing inhomogeneities and a blunted velocity profile. We found a good agreement between the shape of the velocity profile predicted by a Mills and Snabre migration model coupled to a Krieger-Dougherty viscosity and the shape measured experimental. However, the magnitude of the velocity was greatly overestimated, most probably due to non-Newtonian effects (shear thinning at low shear rates).

Above solids concentrations of 55%, for small masses and high solids fractions the flow came to halt and separation between the fluid and solid phases occurred. The solid frame remained at rest while the fluid seeped through the granular media, thus eroding the front. When bigger masses were released, we observed a succession of different regimes. After an inertial regime and a pseudo viscous regime, the flow slowed down, corresponding to a new regime in which the shearing was localized in a thin layer at the bottom and there was no shearing of the front. At the same time, we observed that the free surface deformed and exhibited waves. Fractures developed on the top of the flow and, if they grew sufficiently large, modified the local velocity field substantially. The upper region of the bulk slid on the lower region, the sheared plane was 3-mm thick and inclined at 25 deg to 30 deg with respect to the bottom. Finally, at longer times ( $\geq 4$  min) an intermittent motion (stick-slip) was observed with phases during which the suspension was flowing in a quasi-steady regime and phases during which the suspension was at a halt. Yet it is not completely clear what was the underlying physical mechanism, since we only found partial agreement with existing stick-slip models.





## 6 Overall conclusions and outlook

The purpose of this thesis was to develop and test a new experimental platform to gain insight into internal dynamics of two-phase flow avalanches. To that end, we built a 3.5 m long and 10 cm wide inclined flume with an upstream reservoir with the capacity to hold 10 liters of fluid. At a given time, the fluid is instantaneously released and flows down the inclined flume. This dam-break facility was coupled to a Particle Image Velocimetry (PIV) system to measure the velocity profile in the flowing material. Since PIV requires a transparent media, we used an index matched suspension made up of PMMA particles (mean diameter  $\sim 200 \mu\text{m}$ ) and a mix of three Newtonian fluids to adapt the refraction index and the density of the interstitial fluid. In addition to the camera dedicated to PIV acquisition, two other cameras tracked the front position along the flume.

Three experimental campaigns were conducted with the setup, with Newtonian fluids, PMMA suspensions and Carbopol gel (results for Carbopol gel can be found in [38]). More than 30 different flow configurations were tested. Besides the high frame rate allowed by the PIV technique, the index matched measurement technique was very useful for detecting slip near the bottom of the flow for highly concentrated suspensions.

For the Newtonian flows we found a good agreement between lubrication theory (small aspect ratio assumption) and experiments. Velocity profiles were found to be parabolic far from the front as well as very close to the contact line. Near the front, the velocities were significantly overestimated ( $\sim 400\%$ ) by the theory at low Reynolds numbers ( $Re < 2$ ) and slightly underestimated ( $\sim 10\%$ ) at high Reynolds numbers ( $Re > 8$ ).

Experiments on granular suspensions revealed a wealth of behavior depending on the particle concentration, the slope or the mass released. For solid fractions up to 45%, suspensions behaved as homogeneous viscous fluids without inhomogeneity due to migration. For slightly more concentrated suspensions (up to 55%), inhomogeneities arose due to migration and a blunted velocity profile developed behind the front. The shape of the velocity profile was well described by the Mills and Snabre [64] migration model coupled to a Krieger-Dougherty viscosity model. However, the magnitude of the flows was largely overestimated, most probably because of shear-thinning at low shear rates. Above concentrations of 55%, for small masses

## Chapter 6. Overall conclusions and outlook

---

and high solid fractions, the flow stopped after a while and the fluid and solid phases separated. The solid frame stayed at rest while the fluid seeped through the granular media, eroding the front. For larger released masses, we observed a succession of different regimes: After an inertial regime and a pseudo viscous regime, the flow slowed down, corresponding to a new regime in which the shearing was localized in a thin layer at the bottom and no shearing took place near the front. At the same time, we observed that fractures developed on the top of the flow and substantially modified the local velocity field. At longer times ( $\geq 4$  min) an intermittent motion (stick-slip) was observed with phases during which the suspension was flowing in a quasi-steady regime and phases during which the suspension was at a halt. Since experimental results only partially agreed with existing stick-slip models, it is not clear what was the underlying physical mechanism that drove the motion.

With the setup now being fully operational, additional experimental campaigns may be of interest in order to answer more specific questions :

- Concentration measurements should be made. Some encouraging preliminary results were obtained by tracking the center of each particle on the acquired images. However, due to the blurring that occurred when looking deeper in the suspension, reliable results were obtained only near the bottom of the flow. Therefore, future concentration measurements must be done with smaller volumes of suspension in order to produce flow heights not bigger than 1 cm.
- Measurements away from the centerline should be done in order to quantify wall effects. In addition, measurements of the cross-stream velocity near the front should also be of interest in order to gain insight into the three-dimensional nature of the front.
- Flow of non-isodense suspensions should also be investigated. This increasing complexity will induce new behaviors due to sedimentation and segregation. Building a runout area and measuring velocity and concentration profiles near lateral levees would be, in our opinion, a very nice and exciting project.

# A Free-surface and pore pressure measurements

## A.1 Free-surface measurements

Flow depth measurements were made by filming the displacement shift of an inclined laser sheet projected on the free surface (see Figure A.1). This technique was used in two directions: along  $x$  to capture the longitudinal depth profiles and along  $y$  to obtain the cross-stream depth profiles.

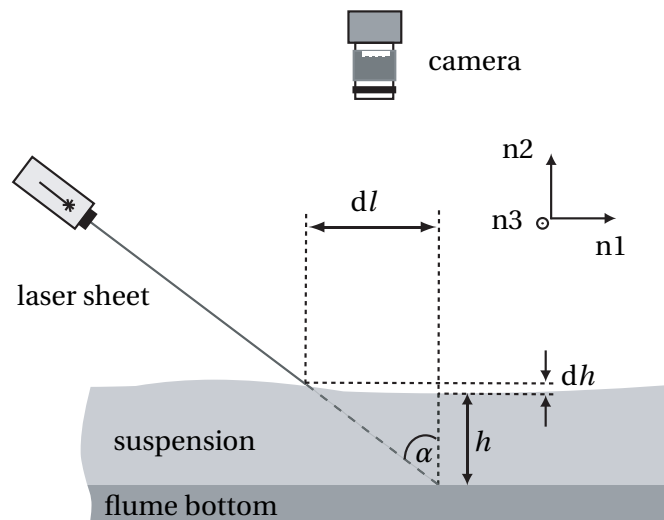


Figure A.1: Side view of the method used to measure the flow depth.

To compute the height of the flow  $h$  from the shift  $dl$  of the laser sheet we calibrated the system: plates of thickness 5, 15, 30 and 45 mm made of PVC were set in the channel. For each height a calibration image was recorded. Then, for each position along  $n3$  (see Figure A.1 for the direction of the  $n1$ ,  $n2$  and  $n3$  axis) we fitted a line  $h(dl, n3) = a(n3)dl + b(n3)$  in order that we could subsequently recover the flow depth  $h$  corresponding to a shift  $dl$  that occurred at a position  $n3$  during an experiment.

Due to the fact that the flow was not horizontal in the direction perpendicular to the laser

## Appendix A. Free-surface and pore pressure measurements

sheet ( $n1$ ), and that the laser line was shifted by  $dl$  along  $n1$ , the depth measured was  $h + dh$  instead of  $h$ . In our setup, the angle  $\alpha$  between the camera and the laser sheet was 25 deg for the longitudinal flow depth profile and 90 deg for the cross-stream flow depth measurements. We verified for all cases that  $dh/h$  was smaller than 0.1.

We used 4 cameras (Basler A311f) mounted with Fujinon 12.5-mm lenses to record the laser sheet shift along the whole flume length with the frame rate set to 28.8 Hz. Optical deformations and perspective effects were corrected during image processing. Laser sheets were produced with 4 laser diodes ( $\lambda = 670$  nm).

### A.2 Basal pore pressure measurements

Basal fluid pressures were measured using differential pressure sensors (model Honeywell DC001NDC4, with a pressure detection range from -250 to 250 Pa) linked to a data-acquisition device (model USB 6221 from National Instruments) in order to record the pore-pressure signals (sampling frequency  $f = 500$  Hz). As depicted in Figure A.2, sensors were connected by a 4-mm tube filled with dibromohexane (DBH) to the base of the flume. Since DBH has a higher density than the suspensions, particles and interstitial fluid were prevented from entering the tube.

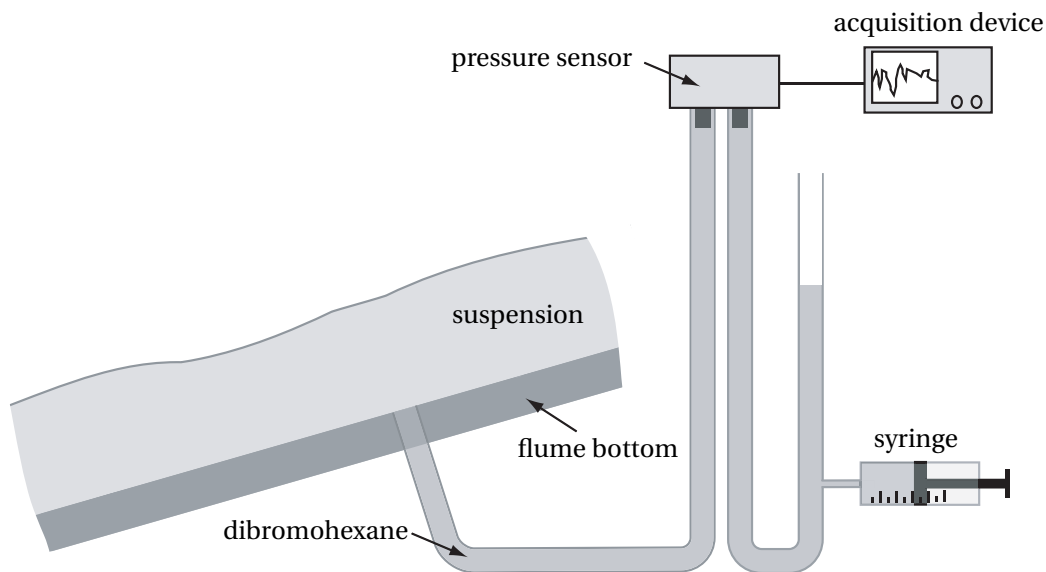


Figure A.2: Pore pressure monitoring. We used four sensors to monitor the basal pore pressure at different places along the flume but for the sake of clarity only one pressure sensor is shown.

Because the sensors performed differential measurements, we connected the other port of the sensor to an open-end tube also filled with DBH. A screw-syringe was used to set the sensor offset to an appropriate value; the sensors were calibrated before each run. The uncertainty of

## A.2. Basal pore pressure measurements

---

pressure measurements was  $\pm 3\%$  according to the manufacturer.

Tests were carried out during both static conditions and viscous flows to evaluate the performance of the system. In particular, we tested screened (by filter paper with typical mesh size  $10\ \mu\text{m}$ ) and unscreened holes since authors [106] recommended use of screens to avoid particles passing into the tubes. Despite pressure fluctuations  $\sim 30\%$  smaller, no significant differences were observed. We also tested the sensitivity of the tube inclination on the pressure: holes with different angles (from  $-45\ \text{deg}$  to  $+45\ \text{deg}$ ) were drilled but no significant differences were found.



# Bibliography

- [1] R.M. Iverson. The physics of debris flows. *Reviews of Geophysics*, 35:245–296, 1997.
- [2] C. Ancey. Debris flows and related phenomena. In N.J. Balmforth and A. Provenzale, editors, *Geomorphological Fluid Mechanics: Selected Topics in Geological and Geomorphological Fluid Mechanics*. Springer, Berlin, 2001.
- [3] T. C. Pierson, R. J. Janda, J. Thouret, and C. A. Borrero. Perturbation and melting of snow and ice by the 13 november 1985 eruption of nevado del ruiz, colombia, and consequent mobilization, flow and deposition of lahars. *Journal of Volcanology and Geothermal Research*, 41(1-4):17–66, 1990.
- [4] T. Takahashi. Debris flow. *Annual review of fluid mechanics, volume 13*, pages 57–77, 1981.
- [5] M. Del Prete, F.M. Guadagno, and A.B. Hawkins. Preliminary report on the landslides of 5 may 1998, campania, southern italy. *Bulletin of Engineering Geology and the Environment*, 57(2):113–129, 1998.
- [6] C. Berger. *Debris flow entrainment and sediment transfer processes at the Illgraben catchment, Switzerland*. PhD thesis, Universität Bern, 2010.
- [7] D. Rickenmann and M. Zimmermann. The 1987 debris flows in Switzerland: documentation and analysis. *Geomorphology*, 8:175–189, 1993.
- [8] O. Français and B. Duvernay. Laves torrentielles sur l’autoroute a9. *Strasse und Verkehr*, 84(5):208–213, 1998.
- [9] S.P. Pudasaini and K. Hutter. *Avalanche Dynamics*. Springer, Berlin, 2006.
- [10] C. Berger, B. W. McArdell, and F. Schlunegger. Sediment transfer patterns at the Illgraben catchment, Switzerland: Implications for the time scales of debris flow activities. *Geomorphology*, 125(3):421–432, 2011.
- [11] C. Berger, B. W. McArdell, and F. Schlunegger. Direct measurement of channel erosion by debris flows, Illgraben. *Journal of Geophysical Research F: Earth Surface*, 116(1), 2011.

## Bibliography

---

- [12] E. Bardou. *Méthodologie de diagnostic des laves torrentielles sur un bassin versant alpin*. PhD thesis, École Polytechnique Fédérale de Lausanne, 2002.
- [13] C. G. Johnson, B. P. Kokelaar, R. M. Iverson, R. J. LaHusen, M. Logan, and J. M. N. T. Gray. The kinematics of levee formation in geophysical mass flows. *J. Geophys. Res.* (in press).
- [14] J.M.N.T. Gray and B.P. Kokelaar. Large particle segregation, transport and accumulation in granular free-surface flows. *Journal of Fluid Mechanics*, 652:105–137, 2010.
- [15] S.B. Savage and C.K.K. Lun. Particle size segregation in inclined chute flow of dry cohesionless granular solids. *Journal of Fluid Mechanics*, 189:311–335, 1988.
- [16] J.M.N.T. Gray and V. Chugunov. Particle-size segregation and diffusive remixing in shallow granular avalanches. *Journal of Fluid Mechanics*, 569:365–398, 2006.
- [17] R. M. Iverson, M. Logan, R. G. LaHusen, and M. Berti. The perfect debris flow aggregated results from 28 large-scale experiments. *Journal Of Geophysical Research-Earth Surface*, 115, 2010.
- [18] R.M. Iverson and R.G. LaHusen. Dynamic pore-pressure fluctuations in rapidly shearing granular materials. *Science*, 246:796–799, 1989.
- [19] J. J. Major and R. M. Iverson. Debris-flow deposition: Effects of pore-fluid pressure and friction concentrated at flow margins. *Bulletin of the Geological Society of America*, 111(10):1424–1434, 1999.
- [20] J.J. Major. Gravity-driven consolidation of granular slurries – Implications for debris-flow deposition and deposit characteristics. *Journal of Sedimentary Research*, 70:64–83, 2000.
- [21] B.W. McArdell, P. Bartelt, and J. Kowalski. Field observations of basal forces and fluid pore pressure in a debris flow. *Geophysical Research Letters*, 34:L07406, 2006.
- [22] S. Cochard and C. Ancey. Tracking the free surface of time-dependent flows: Image processing for the dam-break problem. *Experiments in Fluids*, 44:59–71, 2008.
- [23] A. Badoux, C. Graf, J. Rhyner, R. Kuntner, and B. W. McArdell. A debris-flow alarm system for the alpine illgraben catchment: design and performance. *Natural Hazards*, 49(3):517–539, 2009.
- [24] G. Félix and N. Thomas. Relation between dry granular flow regimes and morphology of deposits: formation of levées in pyroclastic deposits. *Earth and Planetary Science Letters*, 221:197–213, 2004.
- [25] S. Wiederseiner, N. Andreini, G. Épely-Chauvin, G. Moser, M. Monneréau, J.M.N.T. Gray, and C. Ancey. Experimental investigation into segregating granular flows down chutes. *Physics of Fluids*, 23:013301, 2011.



- 
- [26] J. C. Phillips, A.J. Hogg, R.R. Kerswell, and N. Thomas. Enhanced mobility of granular mixtures of fine and coarse particles. *Earth and Planetary Science Letters*, 246:466–480, 2006.
- [27] C. Ancey. Dry granular flow down an inclined channel: Experimental investigations on the frictional-collisional regime. *Physical Review E*, 65:011304, 2002.
- [28] O. Pouliquen. On the shape of granular front down rough inclined planes. *Physics of Fluids*, 11:1956–1958, 1999.
- [29] T. Ward, C. Wey, R. Glidden, A. E. Hosoi, and A. L. Bertozzi. Experimental study of gravitation effects in the flow of a particle-laden thin film on an inclined plane. *Physics of Fluids*, 21(8), 2009.
- [30] B. Nsom. The dam break problem for a hyperconcentrated suspension. *Applied Rheology*, 10(5):224–230, 2000.
- [31] C. Bonnoit, T. Darnige, E. Clement, and A. Lindner. Inclined plane rheometry of a dense granular suspension. *Journal of Rheology*, 54(1):65–79, 2010.
- [32] G. Chambon, A. Ghemmour, and D. Laigle. Gravity-driven surges of a viscoplastic fluid: an experimental study. *Journal of Non-Newtonian Fluid Mechanics*, 158:54–62, 2009.
- [33] S. Cochard and C. Ancey. Experimental investigation into the spreading of viscoplastic fluids on inclined planes. *Journal of Non-Newtonian Fluid Mechanics*, 158:73–84, 2009.
- [34] C. Ancey and S. Cochard. The dam-break problem for herschel-bulkley viscoplastic fluids down steep flumes. *Journal of Non-Newtonian Fluid Mechanics*, 158(1-3):18–35, 2009.
- [35] B.D. Timberlake and J.F. Morris. Particle migration and free-surface topography in inclined plane flow of a suspension. *Journal of Fluid Mechanics*, 538:309–341, 2005.
- [36] M.K. Lyon and L.G. Leal. An experimental study of the motion of concentrated suspensions in two-dimensional channel flow. Part 1. monodisperse systems. *Journal of Fluid Mechanics*, 363:25–56, 1998.
- [37] N.C. Shapley, R.C. Armstrong, and R.A. Brown. Laser Doppler velocimetry measurements of particle velocity fluctuations in a concentrated suspension. *Journal of Rheology*, 46:241–27, 2002.
- [38] N. Andreini, C. Ancey, and G. Epely-Chauvin. Internal dynamics of newtonian and viscoplastic fluid avalanches down a sloping bed. *Submitted to Physics of Fluids*, 2012.
- [39] S. Wiederseiner. *Rheophysics of concentrated particle suspensions in a Couette cell using a refractive index matching technique*. PhD thesis, Ecole Polytechnique Fédérale de Lausanne, 2010.

## Bibliography

---

- [40] S. Wiederseiner, N. Andreini, G. Epely-Chauvin, and C. Ancey. Refractive-index and density matching in concentrated particle suspensions: A review. *Experiments in Fluids*, 50(5):1183–1206, 2011.
- [41] C. Ancey. Plasticity and geophysical flows: A review. *Journal of Non-Newtonian Fluid Mechanics*, 142(1-3):4–35, 2007. Cited By (since 1996): 57.
- [42] H. E. Huppert. The propagation of two-dimensional and axisymmetric viscous gravity currents over a rigid horizontal surface. *Journal of Fluid Mechanics*, 121:43–58, 1982.
- [43] H. E. Huppert. Flow and instability of a viscous current down a slope. *Nature*, 300(5891):427–429, 1982.
- [44] C. Ancey, S. Cochard, and N. Andreini. The dam-break problem for viscous fluids in the high-capillary-number limit. *Journal of Fluid Mechanics*, 624:1–22, 2009.
- [45] G. K. Batchelor and J. T. Green. Determination of the bulk stress in a suspension of spherical particles to order  $c^2$ . *Journal of Fluid Mechanics*, 56(Part 3):401–427, 1972.
- [46] I.M. Krieger and T.J. Dougherty. A mechanism for non-Newtonian flow in suspensions of rigid spheres. *Transactions of the Society of Rheology*, 3:137–152, 1959.
- [47] G. Ovarlez, F. Bertrand, and S. Rodts. Local determination of the constitutive law of a dense suspension of noncolloidal particles through magnetic resonance imaging. *Journal of Rheology*, 50(3):259–292, 2006.
- [48] P. Mills and P. Snabre. Apparent viscosity and particle pressure of a concentrated suspension of non-brownian hard spheres near the jamming transition. *European Physical Journal E*, 30(3):309–316, 2009.
- [49] I. E. Zarraga, D. A. Hill, and D. T. Leighton Jr. The characterization of the total stress of concentrated suspensions of noncolloidal spheres in newtonian fluids. *Journal of Rheology*, 44(2):185–220, 2000.
- [50] Feng S. Graham A. L. Chawla V. Reardon, P. T., R. S. Admuthe, and J. Abbott. Shear-thinning of polydisperse suspensions. *Journal of Physics D: Applied Physics*, 41(11), 2008.
- [51] A. Fall, A. Lemaître, F. Bertrand, D. Bonn, and G. Ovarlez. Shear thickening and migration in granular suspensions. *Physical Review Letters*, 105:268–303, 2010.
- [52] G. Y. Onoda and E. G. Liniger. Random loose packings of uniform spheres and the dilatancy onset. *Physical Review Letters*, 64(22):2727–2730, 1990.
- [53] C. R. Wildemuth and M. C. Williams. Viscosity of suspensions modeled with a shear-dependent maximum packing fraction. *Rheologica Acta*, 23(6):627–635, 1984.

- 
- [54] R. Farris. Prediction of the viscosity of multimodal suspensions from unimodal viscosity data. *Transactions of the Society of Rheology*, 12:281–301, 1968.
- [55] A. Fall, F. Bertrand, G. Ovarlez, and D. Bonn. Yield stress and shear banding in granular suspensions. *Physical Review Letters*, 103:178301, 2009.
- [56] F. Gadala-Maria and Andreas Acrivos. Shear-induced structure in a concentrated suspension of solid spheres. *Journal of Rheology*, 24(6):799–814, 1980.
- [57] D. Leighton and A. Acrivos. The shear-induced migration of particles in concentrated suspensions. *Journal of Fluid Mechanics*, 181:415–439, 1987.
- [58] R. J. Phillips, R. C. Armstrong, R. A. Brown, A. L. Graham, and J. R. Abbott. A constitutive equation for concentrated suspensions that accounts for shear-induced particle migration. *Physics of Fluids A*, 4(1):30–40, 1992.
- [59] N. Tetlow, A. L. Graham, M. S. Ingber, S. R. Subia, L. A. Mondy, and S. A. Altobelli. Particle migration in a couette apparatus: Experiment and modeling. *Journal of Rheology*, 42(2):307–327, 1998.
- [60] Prabhu R. Nott and John F Brady. Pressure-driven flow of suspensions: simulation and theory. *Journal of Fluid Mechanics*, 275:157–199, 1994.
- [61] J. F. Morris and J. F. Brady. Pressure-driven flow of a suspension: Buoyancy effects. *International Journal of Multiphase Flow*, 24(1):105–130, 1998.
- [62] J. F. Morris and F. Boulay. Curvilinear flows of noncolloidal suspensions: The role of normal stresses. *Journal of Rheology*, 43(5):1213–1237, 1999.
- [63] N.C. Shapley, R.A. Brown, and R.C. Armstrong. Evaluation of particle migration models based on laser doppler velocimetry measurements in concentrated suspensions. *Journal of Rheology*, 48(2):255–279, 2004.
- [64] P. Mills and P. Snabre. Rheology and structure of concentrated suspensions of hard spheres. shear induced particle migration. *Journal de physique.II*, 5(10):1597–1608, 1995.
- [65] C.J. Koh, P. Hookham, and L.G. Leal. Experimental investigation of concentrated suspension flows in a rectangular channel. *Journal of Fluid Mechanics*, 266:1–32, 1994.
- [66] M.K. Lyon and L.G. Leal. An experimental study of the motion of concentrated suspensions in two-dimensional channel flow. Part 2. bidisperse systems. *Journal of Fluid Mechanics*, 363:57–77, 1998.
- [67] P. Coussot and C. Ancey. Rheophysical classification of concentrated suspensions and granular pastes. *Physical Review E*, 59:4445–4457, 1999.

## Bibliography

---

- [68] T. Moraczewski, H. Tang, , and N.C. Shapley. Flow of a concentrated suspension through an abrupt axisymmetric expansion measured by nuclear magnetic resonance imaging. *Journal of Rheology*, 49(6):1409–1428, 2005.
- [69] F. Blanc, F. Peters, and E. Lemaire. Particle image velocimetry in concentrated suspensions: Application to local rheometry. *Applied Rheology*, 21(2), 2011.
- [70] B. Ouriev and EJ Windhab. Rheological study of concentrated suspensions in pressure-driven shear flow using a novel in-line ultrasound Doppler method. *Experiments in Fluids*, 32(2):204–211, 2002.
- [71] M. Raffel, C.E. Willert, S.T. Wereley, and J. Kompenhans. *Particle Image Velocimetry*. Springer, Berlin, 2007.
- [72] C.E. Stauffer. The measurement of surface tension by the pendant drop technique. *Journal of Physical Chemistry*, 69(6):1933–1938, 1965.
- [73] P. de Gennes, F. Brochard-Wyart, and D. Quéré. *Gouttes, bulles, perles et ondes*. Belin, Paris, 2005.
- [74] R.V. Craster and Matar O.K. Dynamics and stability of thin liquid films. *Review of Modern Physics*, 81:1131–1198, 2009.
- [75] K. McCarthy and J. Seymour. A fundamental approach for the relationship between the Bostwick measurement and Newtonian fluid viscosity. *Journal of Texture Studies*, 24:1–10, 1993.
- [76] B. Hunt. Newtonian fluid mechanics treatment of debris flows and avalanches. *Journal of Hydraulic Engineering - ASCE*, 120(12):1350–1363, 1994.
- [77] H.E. Huppert. Gravity currents: a personal perspective. *Journal of Fluid Mechanics*, 554:299–322, 2006.
- [78] B. Nsom, K. Debiante, and J.-M. Piau. Bed slope effect on the dam break problem. *Journal of Hydraulic Research*, 38:459–464, 2000.
- [79] J.-M. Piau and K. Debiante. Consistometers rheometry of power-law viscous fluids. *Journal of Non-Newtonian Fluid Mechanics*, 127:213–224, 2005.
- [80] M. L. Sheely. Glycerol viscosity tables. *Industrial and Engineering Chemistry*, 24:1060–1064, 1932.
- [81] R. E. Hampton, A. A. Mammoli, A. L. Graham, N. Tetlow, and S. A. Altobelli. Migration of particles undergoing pressure-driven flow in a circular conduit. *Journal of Rheology*, 41(3):621–640, 1997.
- [82] J. T. Norman, H. V. Nayak, and R. T. Bonnecaze. Migration of buoyant particles in low-reynolds-number pressure-driven flows. *Journal of Fluid Mechanics*, 523:1–35, 2005.

- [83] J. T. Norman, B. O. Oguntade, and R. T. Bonnecaze. Particle-phase distributions of pressure-driven flows of bidisperse suspensions. *Journal of Fluid Mechanics*, 594:1–28, 2008.
- [84] A. Shauly, A. Averbakh, A. Nir, and R. Semiat. Slow viscous flows of highly concentrated suspensions - part ii: Particle migration, velocity and concentration profiles in rectangular ducts. *International Journal of Multiphase Flow*, 23(4):613–629, 1997.
- [85] F. Blanc, F. Peters, and E. Lemaire. Local transient rheological behavior of concentrated suspensions. *Journal of Rheology*, 55(4):835–854, 2011.
- [86] A. M. Corbett, R. J. Phillips, R. J. Kauten, and K. L. McCarthy. Magnetic resonance imaging of concentration and velocity profiles of pure fluids and solid suspensions in rotating geometries. *Journal of Rheology*, 39(5):907–924, 1995.
- [87] J. Zhou, B. Dupuy, A. L. Bertozzi, and A. E. Hosoi. Theory for shock dynamics in particle-laden thin films. *Physical Review Letters*, 94(11), 2005.
- [88] D. M. Husband, L. A. Mondy, E. Ganani, and A. L. Graham. Direct measurements of shear-induced particle migration in suspensions of bimodal spheres. *Rheologica Acta*, 33(3):185–192, 1994.
- [89] A. P. Shapiro and R. F. Probstein. Random packings of spheres and fluidity limits of monodisperse and bidisperse suspensions. *Physical Review Letters*, 68(9):1422–1425, 1992.
- [90] J. R. Abbott, N. Tetlow, A. L. Graham, S. A. Altobelli, E. Fukushima, L. A. Mondy, and T.S. Stephens. Experimental observations of particle migration in concentrated suspensions: Couette-flow. *Journal of Rheology*, 35(5):773–795, 1991.
- [91] B. J. Medhi, A. Ashok Kumar, and A. Singh. Apparent wall slip velocity measurements in free surface flow of concentrated suspensions. *International Journal of Multiphase Flow*, 37(6), 2011.
- [92] N. Huang, G. Ovarlez, F. Bertrand, S. Rodts, P. Coussot, and Bonn D. Flow of wet granular materials. *Physical Review Letters*, 94:028301, 2005.
- [93] C. Chang and R. L. Powell. The rheology of bimodal hard-sphere dispersions. *Physics of Fluids*, 6(5):1628–1636, 1994.
- [94] A. Shauly, A. Wachs, and A. Nir. Shear-induced particle migration in a polydisperse concentrated suspension. *Journal of Rheology*, 42:1329–1348, 1998.
- [95] F. Heslot, T. Baumberger, B. Perrin, B. Caroli, and C. Caroli. Creep, stick-slip, and dry-friction dynamics: Experiments and a heuristic model. *Physical Review E*, 49(6):4973–4988, 1994.

## Bibliography

---

- [96] T. Baumberger, F. Heslot, and B. Perrin. Crossover from creep to inertial motion in friction dynamics. *Nature*, 367(6463):544–546, 1994.
- [97] G. Ananthakrishna and R. De. *Dynamics of stick-slip: Some universal and not so universal features*, volume 705 of *Lecture Notes in Physics*. 2006.
- [98] M. Lubert and A. De Ryck. Slip events and dilatancy in a sheared fine noncohesive powder. *Physical Review E - Statistical, Nonlinear, and Soft Matter Physics*, 63(2 I):0215021–0215027, 2001.
- [99] S. Nasuno, A. Kudrolli, and J. P. Gollub. Friction in granular layers: Hysteresis and precursors. *Physical Review Letters*, 79(5):949–952, 1997.
- [100] K. E. Daniels and N. W. Hayman. Boundary conditions and event scaling of granular stick-slip events. In *AIP Conference Proceedings*, volume 1145, pages 567–570, 2009.
- [101] G. Ovarlez and E. Clément. Slow dynamics and aging of a confined granular flow. *Physical Review E - Statistical, Nonlinear, and Soft Matter Physics*, 68(3 I):313021–3130217, 2003.
- [102] N. Higashi and I. Sumita. Experiments on granular rheology: Effects of particle size and fluid viscosity. *Journal of Geophysical Research B: Solid Earth*, 114(4), 2009.
- [103] R. M. Iverson, M. E. Reid, N. R. Iverson, R. G. LaHusen, M. Logan, J. E. Mann, and D. L. Brien. Acute sensitivity of landslide rates to initial soil porosity. *Science*, 290(5491):513–516, 2000.
- [104] R. M. Iverson. Regulation of landslide motion by dilatancy and pore pressure feedback. *Journal of Geophysical Research F: Earth Surface*, 110(2), 2005.
- [105] D. G. Schaeffer and R. M. Iverson. Steady and intermittent slipping in a model of landslide motion regulated by pore-pressure feedback. *SIAM Journal on Applied Mathematics*, 69(3):769–786, 2008.
- [106] M. Pailha, M. Nicolas, and O. Pouliquen. Initiation of underwater granular avalanches: Influence of the initial volume fraction. *Physics of Fluids*, 20(11), 2008.
- [107] M. Pailha and O. Pouliquen. A two-phase flow description of the initiation of underwater granular avalanches. *Journal of Fluid Mechanics*, 633:115–135, 2009.

# Curriculum Vitae

**Nicolas Andreini**

Swiss, Italian

Born on September 10, 1981

nicolas.andreini@a3.epfl.ch

## Education

---

- |           |   |
|-----------|---|
| 2007-2012 | Ph.D. student<br>Ecole Polytechnique Fédérale de Lausanne (EPFL), Switzerland     |
| 2001-2007 | Master in Physics<br>Ecole Polytechnique Fédérale de Lausanne (EPFL), Switzerland |

## Publications

---

### Peer-reviewed

- N. Andreini, G. Epely-Chauvin and C. Ancey, "Internal dynamics of Newtonian and viscoplastic fluid avalanches down a sloping bed", *submitted to Physics of Fluids*.
- S. Wiederseiner, N. Andreini, G. Epely-Chauvin and C. Ancey, "Refractive-index and density matching in concentrated particle suspensions: A review", *Experiments in Fluids* 50(5) (2011) 1183-1206.
- S. Wiederseiner, N. Andreini, G. Epely-Chauvin, G. Moser, M. Monnereau, J. M. N. T. Gray and C. Ancey, "Experimental investigation into segregating granular flows down chutes", *Physics of Fluids* 23(1) (2011).
- C. Ancey, S. Cochard and N. Andreini, "The dam-break problem for viscous fluids in the high-capillary-number limit", *Journal of Fluid Mechanics* **624** (2009) 1-22. .

### Conference Proceedings

- S. Wiederseiner, C. Ancey, M. Rentschler and N. Andreini, "Rheophysics of highly concentrated coarse-particle suspensions in a wide-gap couette rheometer", 6th International Conference on Micromechanics of Granular Media, Powders and Grains 2009, Golden CO, AIP Conference Proceedings 1145, 1063-1066 .
- N. Andreini, S. Wiederseiner, M. Rentschler and C. Ancey, "Avalanches of concentrated granular suspensions down an inclined plane", XVth International Congress on Rheology, Monterey, AIP Conference Proceedings 1027, 1045-1047.
- S. Wiederseiner, C. Ancey, M. Rentschler and N. Andreini, "Rheophysical investigation in concentrated particle suspensions", XVth International Congress on Rheology, Monterey, AIP Conference Proceedings 1027, 929-931.